POLITECNICO
MILANO 1863

SCUOLA DI INGEGNERIA INDUSTRIALE
E DELL'INFORMAZIONE

Impact of hailstorm on PV modules – Hail Resistance Tests on modules with different angle of incidence and preaging conditions.

TESI DI LAUREA MAGISTRALE IN
ENERGY ENGINEERING
INGEGNERIA ENERGETICA

Author: **Simone Ballerio**

Student ID: 969916
Supervisor: Claudio Del Pero
Co-supervisor: Dominika Chudy, Mauro Caccivio
Academic Year: 2023-24

Abstract

Climate change is leading to an increase in extreme weather event, including hailstorms. Both the severity and frequency of hailstorms have risen, leading to a notable rise in average hailstone diameter and the number of hail reports. This thesis investigates the effects of hail impact on photovoltaic (PV) modules, focusing specifically on power loss, glass failure and cell damage. More in detail, it analyses the impact of specific field conditions such as the tilting of a module or the incidence angle respect to an iceball or different aging conditions, reproduced through accelerated aging or mechanical stress applied on the modules. The experiment is made in collaboration with SUPSI PVLab, the only accredited laboratory in Switzerland for tests on PV modules such as I-V characterization, Electroluminescence and UV picturing, Hail resistance, Damp heat and mechanical load. The experiment is designed as a sequence of non-standard HAR tests on the selected modules, with different tilt angles and pre-aging conditions, interspaced by EL imaging and electrical measurements in order to evaluate and monitor the impact of iceballs on the PV cells and on the performance. The EL pictures are also used as a basis for a crack analysis. Major findings show that iceballs impacted non perpendicularly on the modules are less likely to cause the front glass breakage and also cracks on the cells. Tilted modules require higher kinetic impact energy to create cracks. The electrical performance of the module decreases depending on the type of damages created on the modules' cells; the harsher decrease it's found when new cracks cause dark areas due to partial electrical disconnection or badly damaged cells. The worst damaged cells are usually consequence of higher number of shots withstood by the module. The different types of defects pre-existent on the cells have different probability of initiating cracks and requires different impact kinetic energy. Most of those types of defects can be avoided improving the soldering phase.

Key-words: Hail, impact, resistance, PV module, cracks, PV cells, performance

Abstract in italiano

Il cambiamento climatico sta portando a un aumento degli eventi meteorologici estremi, inclusi eventi di grandine. Sia la gravità che la frequenza delle grandinate è aumentato, con un notevole incremento del diametro medio dei chicchi di grandine e del numero di segnalazioni. Questa tesi esamina gli effetti dell'impatto della grandine sui moduli fotovoltaici (FV), concentrandosi in particolare sulla perdita di performance, il danneggiamento del vetro e delle celle. Più in dettaglio, analizza l'effetto di specifiche condizioni sul campo, come l'angolo di inclinazione del modulo o di incidenza rispetto ad un chicco, oppure le diverse condizioni di invecchiamento, riprodotte tramite invecchiamento accelerato o stress meccanico applicato sui moduli. L'esperimento è stato realizzato in collaborazione con il SUPSI PVLab, l'unico laboratorio accreditato in Svizzera per i test sui moduli fotovoltaici, quali la caratterizzazione I-V, l'elettroluminescenza e la fotoluminescenza, la resistenza alla grandine, e test di resistenza al carico meccanico statico o invecchiamento accelerato tramite "Damp Heat". L'esperimento è progettato come una sequenza di test HAR non standard sui moduli selezionati, con angoli di inclinazione diversi e condizioni di invecchiamento, intervallati da EL e misurazioni elettriche per valutare e monitorare l'impatto della grandine simulata sulle celle FV e sulla performance. Le immagini EL vengono anche utilizzate come base per un'analisi delle cricche. I principali risultati mostrano che le palle di ghiaccio impattate non perpendicolarmente sui moduli hanno meno possibilità di causare la rottura del vetro frontale e cricche sulle celle. I moduli inclinati richiedono un'energia cinetica di impatto maggiore per creare cricche. La performance elettriche del modulo diminuisce a seconda del tipo di danno creato sulle celle del modulo; la diminuzione più significativa si riscontra quando nuove crepe causano aree scure nel EL dovute a disconnessione elettrica parziale o celle gravemente danneggiate. Le celle più danneggiate sono solitamente dovute ad un numero maggiore di colpi sopportati dal modulo. I diversi tipi di difetti preesistenti sulle celle hanno probabilità diverse di innescare cricche e richiedono diverse energie cinetiche di impatto. La maggior parte di questi difetti può essere evitata migliorando la fase di saldatura.

Parole chiave: Grandine, impatto, resistenza, modulo fotovoltaico, cricche, celle fotovoltaiche, performance

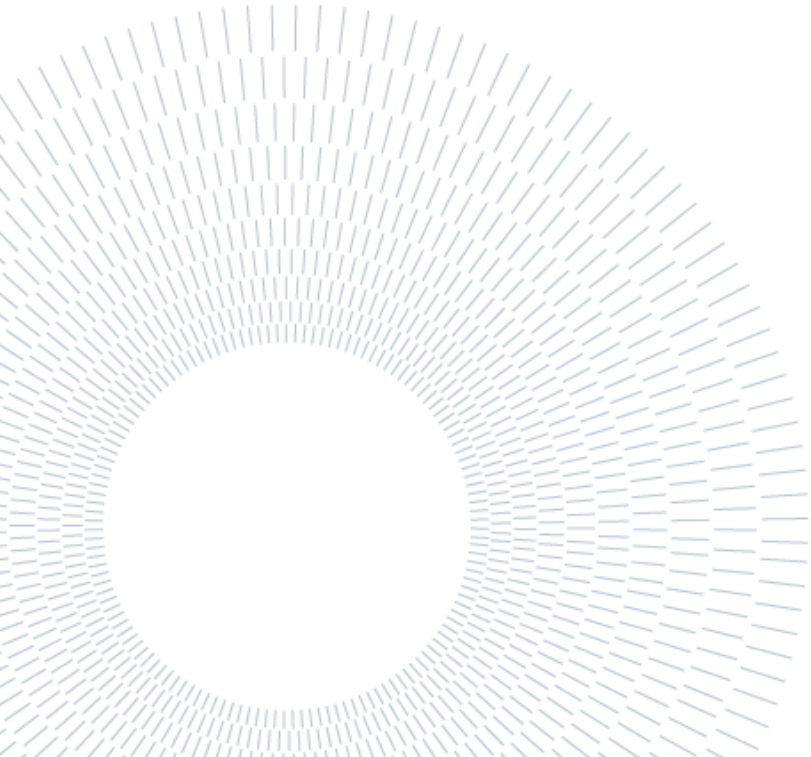

Contents

Abstract ..... **i**

Abstract in italiano ..... **iii**

Contents ..... **v**

Introduction **1**

1 State of the art in photovoltaic technology **3**

1.1. Working principles: Photoelectric effect 4

1.1.1. Efficiency and I-V characterization 5

1.2. Photovoltaic modules 7

1.3. Main photovoltaic technologies 8

2 Photovoltaic module potential failures **15**

2.1. Cell cracks and frame breakage 17

3 PV modules imaging techniques and extreme weather tests **19**

3.1. PV modules characterization techniques 19

3.1.1. Infra-Red thermography 19

3.1.2. UV Fluorescence 20

3.1.3. Electroluminescence (EL) 21

3.2. Extreme weather testing 22

3.2.1. Wind load test 22

3.2.2. Snow load test 23

3.2.3. Hail impact test 23

4 Hail formation and characterization **27**

4.1. Hail Formation 29

4.2. Hail Texture 35

4.3. Hail characteristics 38

4.4. Characterization of impact 42

5 Experimental setup and test methodology **49**

5.1. Darkroom and characterization tests 49

5.2. Static mechanical load test and equipment 52

5.3. Damp heat test and equipment 53

5.4. Hail resistance test and equipment 53
6 Experiment 57
6.1. Design of experiment 57
6.2. Specification about the "*Hail Resistance Test*" cycle 59
6.3. Pre-characterization and choice of reference module 61
7 Results 63
7.1. Mechanical impact on front glass 63
7.2. Electrical parameters and performance 64
7.3. Crack formation and kinetic energy 73
7.4. Crack Analysis 76
8 Conclusions and future developments 83
Bibliography 85
A Appendix 89
List of Figures 95
List of Tables 99

Introduction

The increasing frequency and intensity of hailstorms, exacerbated by climate change, poses a significant threat to the reliability and performance of photovoltaic (PV) systems. As global temperatures rise, shifts in weather patterns are leading to more severe and unpredictable hail events, which can have devastating consequences for solar energy infrastructure [1] [2]. PV modules, while designed to withstand various environmental stressors, remain vulnerable to impact damage caused by hailstones, especially in regions prone to frequent hailstorms, such as northern Italy and southern Switzerland. These regions have experienced a rise in extreme weather events, with hailstorms becoming relevant cause of damage to solar installations. For instance, in 2019, a severe hailstorm in Lombardy caused extensive damage to PV systems, with repair costs exceeding e 20 million in some municipalities [3]. The economic implications of hail damage to PV modules are substantial. Direct costs include the replacement of shattered glass panels and damaged cells, while indirect costs arise from the temporary loss of energy production. In southern Switzerland, hail damage in 2020 led to an estimated 10-15% decrease in regional energy output over several months due to damaged PV installations [4]. These losses can be particularly severe for regions where solar energy is increasing in the local energy mix. In northern Italy and southern Switzerland, where PV installations are expanding, these recurring costs pose a major economic challenge. Moreover, as hailstorms become more frequent and intense due to changing climate patterns, the need for enhanced resilience in PV system design is critical. Research has shown that larger hailstones, over 30 mm in diameter, can severely damage the glass surface of PV modules, causing mechanical stress and microcracks that reduce energy efficiency by up to 20% [4]. The objective of this work is to evaluate the performance of photovoltaic modules after hail impact test based on module structure parameters, with a particular emphasis on the front glass and its performance under varying hailstone impact energy, tilting and aging conditions. The purpose of the thesis is designing and execute an experiment based on Hail Resistance Tests on a certain model of PV modules, while monitoring the initiation and evolution of cracks on their cells and monitoring the variation of the electrical parameters, such as P_{max}, I_{sc} and V_{oc}.

All the tests have been performed at the PVLab of SUPSI (University of Applied Sciences and Arts of Southern Switzerland) located in Mendrisio, Switzerland. The PVLab (Photovoltaic Laboratory) is an accredited laboratory specialized in the characterization of PV modules, with a strong focus on performance and reliability. The lab offers a comprehensive range of tests, including current-voltage measurement,

electroluminescence, insulation resistance, and advanced environmental stress tests such as *"Damp Heat"*, *"Thermal Cycling"*, *"Hail Resistance"*, and *"UV exposure"*. All the prementioned tests are performed following the methodology according to IEC 61215, exception made for the hail resistance test, which is performed as a non-standard test for research purpose.

1 State of the art in photovoltaic technology

Electricity generation from Solar PV increased by a record 270 TWh (+26%) in 2022, almost reaching 1.300 TWh globally, with the largest absolute generation growth between all the renewable technologies in 2022, surpassing wind for the first time in history. This generation growth rate matches the level envisaged from 2023 to 2030 in the Net Zero Emissions by 2050 Scenario. In 2022, solar PV kept its leading position as the power generation technology with the most investment. Global solar PV investments in capacity additions increased by over 20% in 2022 and surpassed USD 320 billion. Solar PV comprised almost 45% of total global electricity generation investment in 2022, three times the spending on all fossil fuel technologies collectively. In 2023, an estimated 96% of newly installed, utility-scale solar PV and onshore wind capacity had lower generation costs than new coal and natural gas plants. [5] Solar PV is the main renewable technology of choice in the private sector and its deployment is shared between:

- Companies investing in own buildings installations, responsible for 26% of total installed PV capacity as of 2022.
- Companies entering into corporate power purchase agreements (PPAs) – signing direct contracts with solar PV plant operators for the purchase of generated electricity. Solar PV plants dominate renewables PPAs, with a share of almost 70% in 2022. [5]

Also, in EU and Brazil, growth in rooftop solar PV is expected to outpace large-scale plants: due to energy crisis and the increasing prices, by doing so residential and commercial consumers can reduce their electricity bills. [5] In 2023 the Swiss Federal Office of Energy recorded an increase of PV systems installation with more than 1.6 GW (+51%). This growth surpassed the previous year value across almost all size categories and employment sectors. The increase was substantial especially for the industrial and manufacturing sector (+65%) and multi-family households (+59%). Approximately, 58'000 new systems were installed with a mean power installed of 28.2 kW [6]. Investment in PV is expected to grow further in the coming years thanks to ambitious government targets, policy support and increasing competitiveness. The total emissions of the electricity and heat sector reached 14.600 Mt of CO2eq in 2022, the maximum ever recorded. PV played an important role in the reduction of CO2 emissions, avoiding approximately 1.399 Mt of annual CO2 emissions, a value 30%

higher from the 2021 one. (Calculated as the emissions that would have been generated from the same amount of electricity produced by each different country's grid mix and also considering PV systems life cycle emissions). This amount of avoided CO_2 emissions represents around 10% of the total electricity and heat sector emissions and 4% of all energy emissions [7].

1.1. Working principles: Photoelectric effect

The solar cell is the fundamental element in a photovoltaic module since, being made of semiconductor material, it can transform solar energy into electric energy [8]. The current is produced by the photoelectric effect, which consists in an electron promoted from the valence band to the conduction band exploiting the energy absorbed by solar radiation. To move from one side to the other, a charge must overcome the energy gap, which is the energy difference between the valence band and the conduction band of the semiconductor [8]. To this end, the energy carried by a photon is greater than the energy gap of a semiconductor. When the photon hits the semiconductor, it is absorbed and the electron acquires enough energy to move from the valence band to the conduction band. This process of absorbing energy from radiation develops an electron-hole pair. Without any action, the electron and the hole would quickly return to their original state, and the energy surplus would be lost as thermal energy [8]. Photovoltaic cells behave like a diode, an electronic component that ideally allows current to flow in only one direction blocking the other. A P-N junction determines an electric field in the semiconductor: one part has a positive charge (P) because it contains a hole of a III element (Boron), whereas the other part is negative (N) because it contains an extra electron of a V element (Phosphorus) [8].

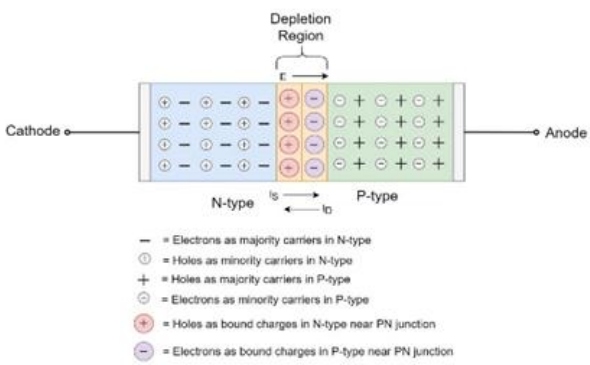

Figure 1.1: P-N junction [9]

Electrons are present in abundance in the N layer, and they diffuse from this region to the P layer, forming a positive distribution of charges at the immediate interface with the P region. This creates a region at the interface between the two parts called

"depletion region", which contains both positive and negative charges between the two sides but no moving charges [8]. The fixed charges create a potential barrier which counteracts an additional flow of charges via diffusion. The first electrode consists of front contacts (negative pole) in the form of conductors, while the second electrode presents rear contacts (positive pole), with a surface area equal to the surface of the cell itself [8]. Front contacts are generally realized by silver and aluminium (Al-Ag) thin cables, these metals are able to conduct efficiently the electrons released by photovoltaic effect. The contacts are divided in:

- **Busbars**: vertical filaments, collecting current from the fingers.
- **Fingers or Gridlines**: horizontal array of filaments with a thickness lower than 0,4 mm.

This configuration allows to conduct current reducing the impact of the active area reduction, as the contacts cover and shade the silicon cell, today there are different technologies and strategies trying to reduce as much as possible costs and energy production by adopting different configurations [7]. On the front side, cells are electrically connected by cell interconnect ribbons to form strings and then string interconnect ribbons, located near the edge of the module, connect multiple strings of cells. However back contact cells exist, to relocate frontal contacts at the rear side of the cell they require interspersed or interdigitated layers of n+ and p+ emitters called the diffusion layer then every metal contact is placed in the back of the cell, leaving the front of the cell entirely free from shading materials [10]. Back contact cells will be discussed thoroughly in section 1.3.

1.1.1. Efficiency and I-V characterization

To properly characterize the power production from a PV module, it is essential to determine its Efficiency η and I-V curve. Efficiency indicates the module's ability to convert solar energy into electrical power: it is defined as :

$$\eta = \frac{P}{G * A}$$

where P is the electrical power output [W], G the incident solar Irradiance [W/m^2] and A the area hit by the radiation [m^2]. Nominal power of PV modules is obtained in Standard Test Conditions (STC), stated by IEC 61215 [11] with the following environmental parameters:

- **Irradiance** G = 1000 W/m^2
- **Temperature** T = 25°C
- **Air Mass** AM = 1.5 G

Air Mass is given as AM = 1/cos(θ) where θ is the vertical angle (zenith angle). Air Mass coefficient is used to describe the standardized condition of solar cells in order

to compare the spectrum of the test Irradiance. G stands for Global which comprehends direct and diffuse radiation.

I-V characteristic curve allows to determine short-circuit current I_{sc}, open-circuit voltage V_{oc}, and other relevant parameters which are used in PV system design phase [7]. Moreover, it allows to understand the cell behaviour under varying conditions (therefore its production at part load), as non-dispatchable renewable technologies deeply suffer from meteorological conditions. There are two main factors that influence power production and efficiency in PV modules: Irradiance G [W/m^2] and Temperature T [°C], and their effect can be clearly seen examining the I-V curve [12]. To account for these effects and evaluate efficiency, temperature coefficient is used to correctly estimate power production and total energy yield in the design phase under different weather conditions. By keeping T constant and varying G, it is possible to observe how short-circuit current I_{sc} decreases as G decreases proportionally while the open-circuit voltage V_{oc} decreases slightly with a logarithmic trend [12].

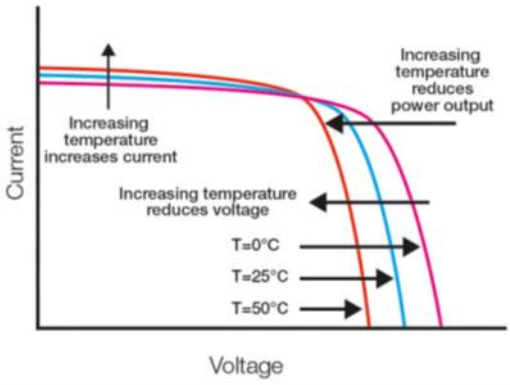

Figure 1.2: Effect of T on I-V curves [12]

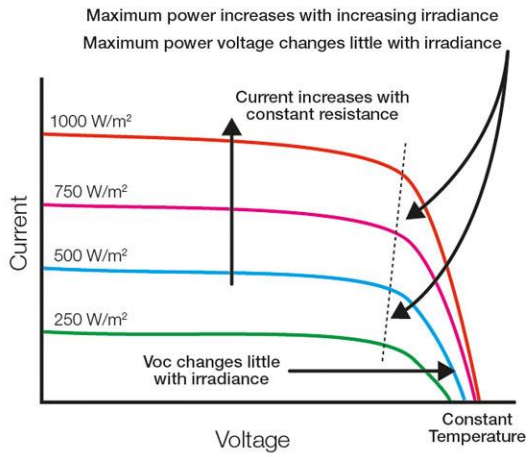

Figure 1.3: Effect of G on I-V curves [12]

When temperature increases, V_{oc} will decrease, while I_{sc} will slightly increase. A temperature increase causes an overall decrease in maximum power output Pmax since the negative influence on voltage is predominant compared to the beneficial impact on current. To account for these effects, temperature coefficient is used to correctly estimate power production and total energy yield in the design phase under different weather conditions [12]. In the case of a defective cell, the voltage decreases while the I_{sc} remains at the same normal value, while in shaded cell, Voc and Isc both decrease decisively. In both cases the maximum power produced by the string will decrease with respect to the one produced at nominal conditions [12]. For cells connected in series, the final open circuit voltage $V_{oc,string}$ will be equal to the sum of individual V_{oc}, while the final short circuit current $I_{sc,string}$ corresponds with Isc of the faulty cell. Therefore, in series connection when a cell is defective or shaded, it produces less current and behaves as a sort of resistive load against the remaining cells

dissipating the power generated by the unshaded series-connected PV cells; the sum of the voltages of the cells is applied to the faulty one and it might result in dangerous conditions when close to the short circuit, as the shaded cell heats up turning into a hot spot [12]. The cell then must dissipate power in the form of heat, and this could lead to serious damages in the long run. To solve this problem, bypass diodes are connected in parallel to the cells. In conditions of mismatch, the diode intervenes and bypasses the defective cell, allowing the current to flow through it and not through the faulty cell. Putting a bypass diode in parallel with each individual cell would be too expensive, so depending on the technology and the cells number of the single module, many configurations are possible and subject to optimization, in order to decrease cost and shading negative effects [12]. Series connection allows to sum the voltages and powers of the individual cells, while maintaining low current values, but in case of a single cell failure, the entire string would stop and no longer contribute to power production, because the bypass diode is applied to the whole string and not to the individual cell [12]. Crystalline silicon solar PV modules typically present 60-72 PV cells, even though the market is shifting towards a higher number of cells, the reason of this shift will be shown later in section 1.3

1.2. Photovoltaic modules

A photovoltaic (PV) module consists of numerous interconnected solar cells, encapsulated into a single, durable, and stable unit to produce electricity. The primary purpose of encapsulating these electrically connected cells is to shield them and their interconnecting wires from the often harsh environmental conditions in which they operate. PV modules are generally structured into five main layers.

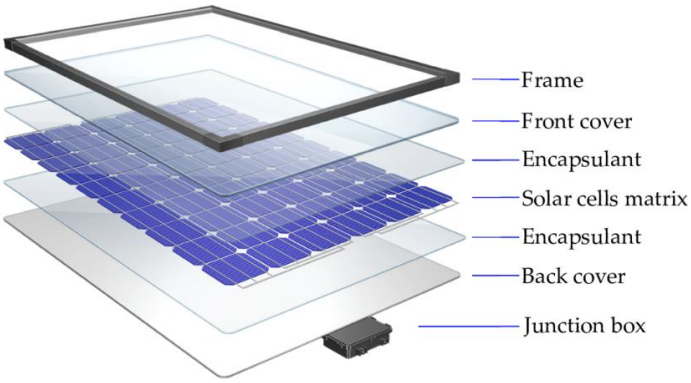

Figure 1.4: PV module assembly

The first layer, at the top, is made of tempered, low-iron-content glass. This glass enhances transparency and reduces reflectivity. Its main purpose is to protect the internal components, particularly the photovoltaic cells, from atmospheric agents like hail, which could severely damage the module [13]. Beneath the tempered glass and above the back cover lie two insulation layers made of a polymeric encapsulant

material. This encapsulant provides adhesive bonding at various module interfaces, mechanical coupling between layers, insulation of the electrical circuit, and structural strength while allowing efficient optical transmission [13]. Over the past decade, Ethylene-Vinyl-Acetate (EVA) has been the predominant encapsulant material in crystalline silicon (c-Si) photovoltaic modules, favoured for its cost-effectiveness, manufacturing simplicity, low water absorption, high vapor resistance, transparency, and durable weather resistance. EVA held approximately 70% market share in 2023 [14]. Polyolefins (PO) are emerging as a viable alternative, especially in bifacial modules with glass-glass configurations and for Silicon Hetero-Junction (SHJ) cells [14]. The central layer consists of the solar cells themselves, which are the core component responsible for electricity generation. The bottom layer, often referred to as the back cover or rear surface, serves to shield the internal electronics from direct environmental exposure and to support safe operation under high DC voltage conditions. Common back cover materials include glass or polymers, such as Tedlar® [13]. Finally, all components are enclosed within a frame, typically made of aluminium or aluminium alloys, designed to ensure structural integrity and facilitate safe, reliable mounting of the PV module. The junction box, although not considered a layer, is an enclosure typically made of plastic or metal that houses the module's electrical connections [13]. Its primary role is to protect the wiring from external environmental factors while also containing potential hazards in the event of electrical failures [13].

1.3. Main photovoltaic technologies

Depending on the semiconductor material present inside the photovoltaic cell, different PV technologies can be identified. These are the main ones:

- Silicon wafer-based PV modules: Crystalline technology can be divided into monocrystalline (c-Si) or polycrystalline (mc-Si) modules depending on the crystallinity and crystal size in the resulting wafer. Monocrystalline silicon cells are composed by a single crystal of silicon, with a continuous crystal lattice, produced by Czochralski process, the crystal cylinders obtained are then sawn in thin slices, creating the wafers. Polycrystalline silicon cell manufacturers, instead, melt multiple silicon fragments together to obtain a compact crystalline composition. For the mc-Si, efficiency ratings will be lower with respect to the monocrystalline ones, due to the fact that electrons will have less space to move because of the different crystals present in each cell [15]. Today, mc-Si technology is no longer considered competitive in the photovoltaic sector, given the superior efficiency of monocrystalline cells and the reduction in production costs.
- Thin-film PV modules: Here semiconductor material is deposited over a glassy support, in stiff panels, or a plastic support, in the case of flexible panels. Thin-film modules are divided in categories depending on the semiconductor type,

which can be: Amorphous Silicon (a-Si), Copper Indium Gallium (di)Selenide (CIGS) or Cadmium Telluride (CdTe) [15]. This technology is characterized by a very low thickness (few micrometers) of the modules, and efficiency is typically lower than crystalline silicon. Materials used in thin-film solar cells are typically produced using simple and scalable methods, more cost-effective than first-generation cells, which led to their development, adding lower environmental impacts consideration, outperforming renewable and non-renewable sources for electricity generation in terms of human toxicity and heavy-metal emissions. However, this technology has shown to have a shorter operational lifetime also due to larger degradation rates compared to Si-based cells, limiting their deployment, as a matter of fact they hold about 5% of the market share in 2023 [16].

- Organic thin-film PV (OPV): these cells use dye or organic semiconductors as light-harvesting active layer. This technology has created increasing interest and research over the last few years and is currently the fastest-advancing solar technology [15]. Despite the low production costs, stable products are not yet available for the market, nevertheless development and demonstration activities are underway [15]. A non-silicon based thin-film PV technology, which uses Perovskite, a type of mineral very good at absorbing light. In the lab, efficiencies of 25% have been reached, but so far only for small cell areas. Perovskite solar cells suffer from short durability and this is their main criticality at the moment [15].

Solar panel technology has dramatically improved over the years thanks to increasing economic interest and a range of innovative solar panels are now being introduced in the market.

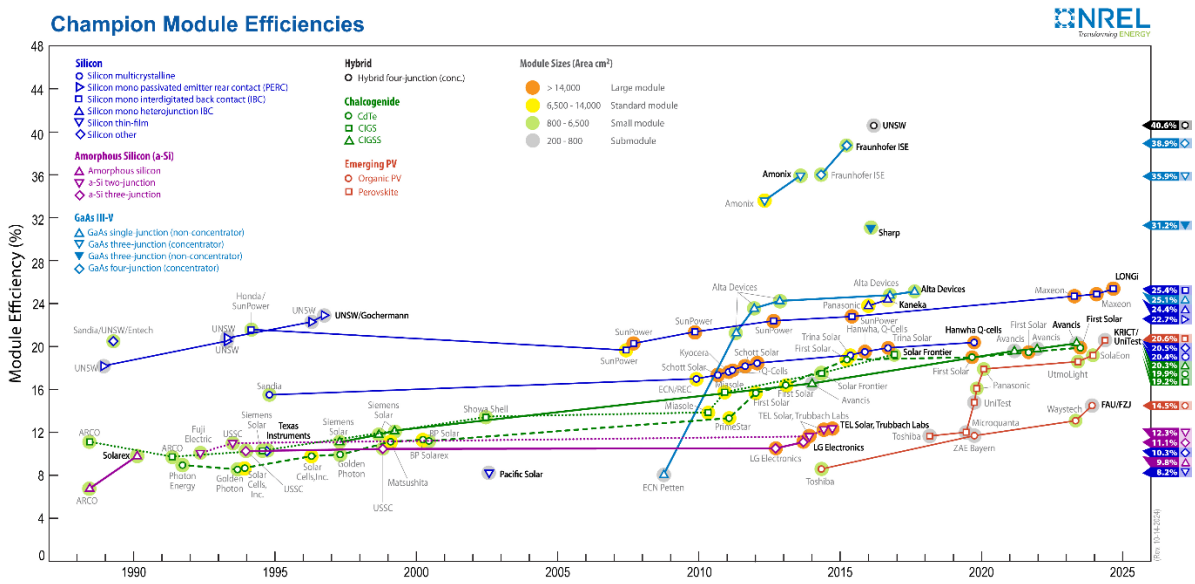

Figure 1.5: Champion module efficiencies [17]

Today, the market is dominated by c-Silicon based PV modules, holding about 95% of the share, with over 70% held by monocrystalline silicon, with different new cell technologies [14]. In the last years a great push towards the use of hetero-junction and organic PV cells has been observed and its market share is going to increase more and more, providing higher efficiencies and performance ratios [14]. Here are presented today's technologies:

- **PERC**: Between the different types of recombination losses, there is one called "surface recombination", it is the one producing losses for traditional c-Si technology. The Passivated Emitter Rear Contact (PERC) solar cell allows PV modules to exceed 20% conversion efficiency after several years of efforts in the industry. This technology includes dielectric surface passivation that reduces electron surface recombination. At the same time, the PERC solar cell reduces the semiconductor-metal area of contact and increases rear surface reflection by including a dielectrically displaced rear metal reflector. This allows photons to be absorbed when going into the cell or out of it, and it also reduces heat absorption. What is more interesting is that bifacial and PERC technologies can be combined. These new and innovative solar cells can deliver up to 18% more power than monofacial solar cells. PERC technology is a cost-effective compromise between efficiency and mass production [18].
- **IBC**: Interdigitated Back Contact (IBC) cell technology has proven to be superior to traditional Aluminium Back Surface Field (Al-BSF) options, but it has the downside of having a more expensive and complex manufacturing process. The main layer of the IBC solar cell is the N-type or P-type c-Si wafer functioning as the absorber layer. The major structural design modification for the IBC solar cells is the inclusion of a diffusion layer, which features interdigitated N-type and P-type layers allowing for the installation of rear side metal contacts. Finally, every metal contact for the IBC solar cell is placed at the back of the cell, leaving the front of the cell entirely free from shading materials. This also allows for installing contacts in a wider area, causing the series resistance of the cells to be lowered. IBC solar cell technology greatly improves the temperature coefficient from -0.387%/°C to -0.446%/°C for traditional options, down to -0.29%/°C. As a result, an IBC solar panel can deliver better performance in hot climate installations. While PERC technology only reduces the busbars, IBC solar panel technology eliminates them, further increasing the effective surface area for photon absorption. In lab tests IBC technology has surpassed PERC technology in efficiency, with IBC achieving 26.7% against the 25.4% of PERC [10]. The major point in favour of PERC over IBC solar cell technology is that IBC technology is more expensive to manufacture. An advantage is that manufacturers can combine both technologies and obtain an even higher-performing PV module [10].

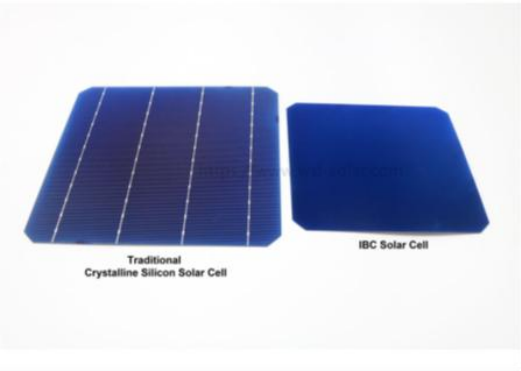

Figure 1.6: IBC cell comparison

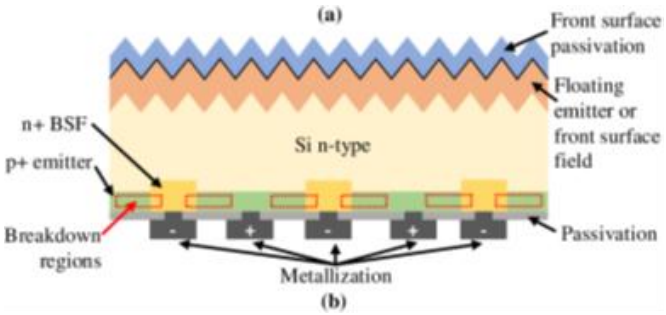

Figure 1.7: IBC cell structure [19]

- **TOPCon**: Tunnel Oxide Passivated Contact (TOPCon) technology belongs to N-type cells. P-type and N-type solar cells are made from a silicon wafer. A N-type TOPCon solar cell installed in a PV module looks identical to a PERC cell. The difference between them lies in the way wafers are doped with chemicals to improve electricity production. P-type cells are doped with boron, while N-type cells are doped with phosphorus. Comparatively, phosphorus degrades less than boron when exposed to oxygen and in addition to that, phosphorus doping adds free electrons to the wafer, increasing efficiency. To manufacture TOPCon cells, tunnel oxide and polysilicon layers are added to the rear side of the cell. TOPCon modules can be manufactured with the same machines as P-type modules, meaning their adoption doesn't require high capital investment for manufacturers. Another major difference is that the passivation process is more laborious for TOPCon solar cells but achieves greater effects. In particular, passivating the rear side with a layer of polycrystalline silicon requires a lot of technical effort but allows the solar cell to handle higher voltages, unluckily the increase of efficiency using this method happens at a slow rate [20]. TOPCon cells convert more sunlight than P-type cells, reaching higher efficiencies than PERC modules, they also have a lower power degradation power during their lifetime, better resistance to high temperatures, making them fit best for hot climates. TOPCon also has a higher bifaciality factor and can perform better in low light conditions, which further extends the electricity generation period during the day and improves the performance over time [21].

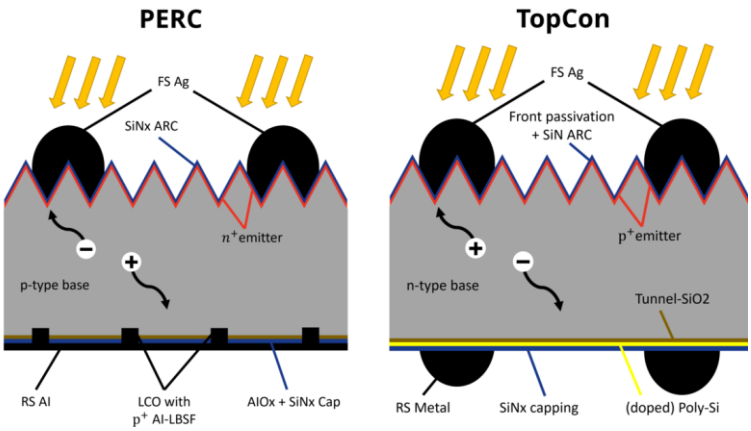

Figure 1.8: TOPCon PERC comparison

- **Heterojunction** (**HJT**): HJT technology is a not-so-new production method that has really grown in interest in the last decade. The technology is currently the solar industry's best option to increase efficiency and power output to their highest levels. HJT combines the best qualities of c-Si with those of a-Si thin-film to produce a high-power hybrid cell that surpasses the performance of the industry's go-to technology, PERC. Multi-junction cell design involves superposing several different cells in a stack. Its goal is to enable a wider spectrum of sunlight to be captured, and therefore to increase overall efficiency [22].

Apart from different cell technologies, it is possible to have also different module designs, the main ones are:

- **Half-cut**: this technology is a modification in the traditional c -Si cell manufacturing process of PV modules. Therefore, half-cut solar panels can be manufactured in combination with PERC and/or bi-facial technologies, resulting into PV modules with reduced power losses and a higher power output. The solar cell is cut in half, as there is less current generated from each cell, this technology can reduce electrical losses by 75%, increases CTM (Cell to Module) power by 3.6%, reduces the effect of partial shading thanks to their unique wiring system and reduce the operating temperature by having less current per cell. Half-cut solar panels show an important reduction in ohmic losses, this aspect is particularly relevant in residential sector applications, where major obstructions and trees can cause high shading, penalizing production [23].

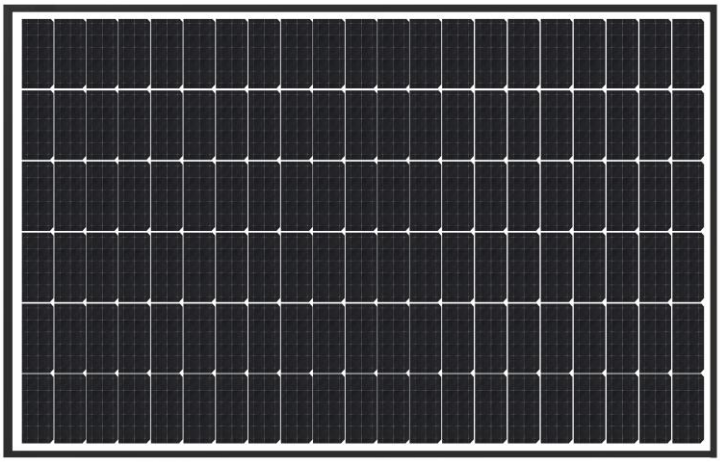

Figure 1.9: Example of Half-Cut module

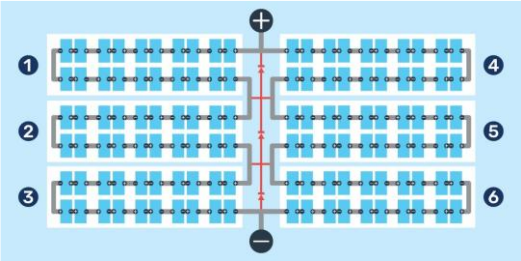

Figure 1.10: Half-Cut connection

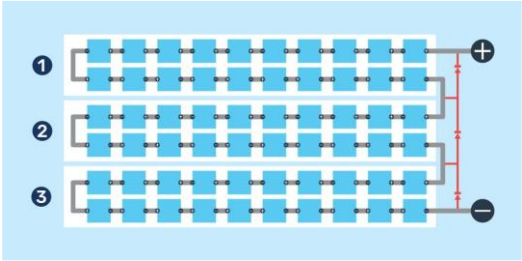

Figure 1.11: Traditional Connection

- **Bifacial**: A bifacial module is capable to harvest sunlight on both its top and bottom sides, differently from monofacial solar panels which only use front side for solar energy production. Bifacials are equipped with solar cells on both the top and rear of the panel. They are usually monocrystalline, although polycrystalline can be used. They are slim and frequently frameless, in fact the hardware used to mount them is realized in order to reduce shading and therefore increase production as much as possible. This means there are only very narrow support rails and corner-only vertical supports. The top of each solar module is covered in protective glass while the backside may be either glass or a clear backsheet. The bottom solar cells absorb the light reflected off the ground, exploiting the normally lost albedo light. To optimize the operation of the underside cells, using superior silicon in monocrystalline cells is preferable [24].

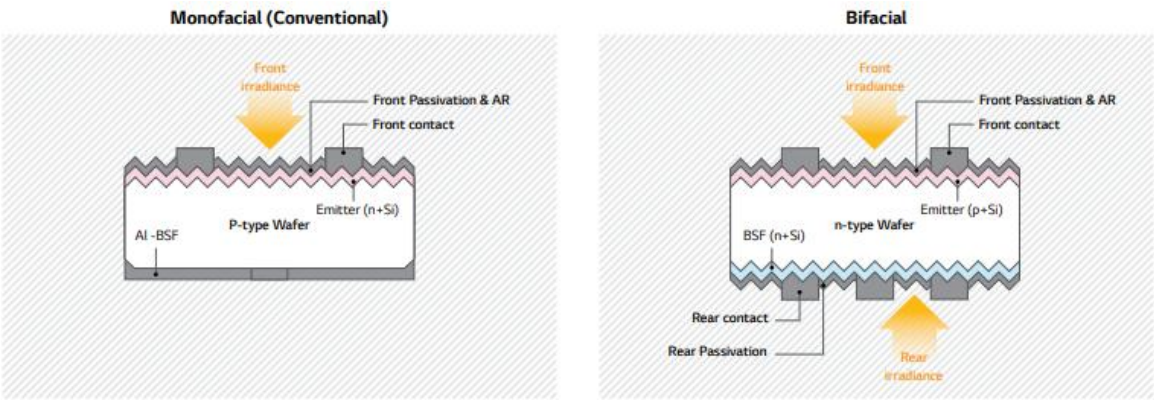

Figure 1.12: Monofacial Bifacial comparison

Concluding, efficiency improvements in PERC technology, the roll out of N-type based products and the deployment of larger wafers in larger modules resulted in higher average module efficiencies and also enabled new module power classes of 600 W and above. Construction of new cell and module capacities in 2022 shifted from PERC to TOPCon and HJT. Improvements in all fields will result in module area efficiency increase: today's mainstream P-type c-Si based modules reach efficiencies of 21.4% that will increase to 22.75% within the next 10 years, while N-type based modules including HJT provide highest power modules with today's efficiencies of close to 22.5% that will increase up to 24% within the next 10 years. Cells using N-type material show the highest efficiency potential of today's cell technology concepts. In fact, TOPCon is expected to gain market share from about 10% in 2022 up to 60% within the next 10 years. TOPCon on N-type is expected to become the dominating cell concept after 2025. HTJ cell technology, the second important N-type concept is expected to increase the 2023 market share of about 9% to over 25% within the next ten years. Moving to the front glass trends, thickness between 2 and 3 mm is mainstream today. Development of modules for special climate markets is expected, varying the bill of material (BOM) and the thickness also due to the increase in frequency of extreme events globally. Modules for special environmental conditions like tropical climate, desert environment, or floating will together account for up to 20% over the next 10 years [14].

2 Photovoltaic module potential failures

The economic success and environmental impact of PV power plants depend deeply on the degradation and service life of PV modules and components. PV modules' lifetime and degradation rate over time directly influences the total yield of electricity, and therefore, the levelized cost of electricity (LCOE) produced [25]. From a financial point of view, degradation of PV modules is important, because it translates directly into maintenance and less power produced, therefore, reduces future cash flows; from a technical perspective, instead, it is necessary to understand its mechanisms, since they may eventually lead to different failures, causing safety issues [26]. PV modules can experience various forms of degradation during their operational life. These alterations impact both the performance and reliability of the modules. Below is a detailed assessment of the most common issues:

- **Delamination**: occurs when the bond between the encapsulant and the module's layers weakens or separates over time. This can lead to reduced protection of the photovoltaic cells, increasing their exposure to environmental factors such as moisture and dirt, thereby accelerating other types of degradation [27].
- **Light-Induced Degradation** (LID): refers to the initial loss of performance in crystalline silicon PV modules due to exposure to sunlight. This phenomenon is typically seen within the first few hours of operation and is caused by the interaction of boron and oxygen in the silicon wafer [27].
- **Encapsulant discoloration**: Over time, the encapsulant material used in PV modules may undergo discoloration, primarily due to ultraviolet (UV) radiation and thermal stress. Encapsulant discoloration can reduce the transmission of light to the solar cells, thereby decreasing the overall efficiency of the module [27].
- **Hotspots**: occur when localized regions of a solar module heat up due to mismatched cells, shading, or defective bypass diodes. These areas experience higher resistance and consequently overheat, which may lead to permanent damage to the affected cells and encapsulation material. Hotspots can be a precursor to severe thermal degradation and reduce the module's efficiency and lifespan. They are critical because they can induce localized melting of materials, accelerate other forms of degradation and lead to further mechanical damage. Detection and prevention of hotspots are crucial in extending the lifespan of the module [27].

Figure 2.1: Fire caused by hotspot induced failure [28]

- **Cell cracking**: is a structural defect where the silicon wafers inside the PV module crack due to mechanical stress during manufacturing, installation, or operation. Cracks may not immediately cause significant power loss but can lead to the formation of micro-cracks, which expand over time due to thermal cycling and external loads (e.g., wind, snow) leading to long term degradation. Micro-cracks allow for thermal and mechanical stresses to propagate damage, often resulting in hotspot formation and eventual failure of the module [27].
- **Potential Induced Degradation** (PID): is a degradation mechanism that occurs due to high-voltage stress between the PV cells and the grounded frame of the module. This effect can lead to leakage currents and reduced power output. PID is particularly relevant in humid environments and at high temperatures [27].
- **Snail tracks**: are discoloration marks on the PV cells that resemble the trail of a snail. While generally considered cosmetic, these marks are associated with micro-cracks in the solar cells, potentially leading to localized efficiency losses and further degradation over time [27].
- **Corrosion/Oxidation:** occurs when moisture or other corrosive elements penetrate the module, usually due to defective sealing or encapsulation. Corrosion typically affects the electrical contacts and interconnects, leading to increased resistive losses and potentially causing module failure [27].
- **Chalking**: refers to the formation of a powdery residue on the back surface of PV modules, typically caused by the degradation of polymeric materials due to UV exposure. In advanced stages, it may be accompanied by cracks in the backsheet and in general by a reduction in the level of insulation, leading to performance degradation [27].
- **Junction box failure**: where electrical connections are housed, it can fail due to poor-quality materials or sealing failure, allowing moisture ingress. Failures can lead to electrical faults, disconnections, and increased risk of fire [27].

Modules are considered damaged when they exhibit observable alterations to appearance, performance or safety due to external and unpredictable factors, including natural catastrophes (hailstorms, snow or wind loads), engineering (manufacturing), transport/ construction (installation), O&M or design errors (soiling, electrical safety system design). In most of the cases damaged modules are still able to produce electricity, but their operating condition might lead to failures and for this reason removing or replacing them is necessary to avoid worse damages [29].

2.1. Cell cracks and frame breakage

Generally, cell cracks can be found inside the silicon, they might either be visible or non-visible. The many methods to detect them are reported in section 2.2. Moreover, cracks can cause an increase in moisture ingress and heat, leading to swelling or deformation of EVA encapsulant, causing power reduction, especially when cracks leave part of the cell electrically insulated, resulting in a dramatic reduction in the current produced by the cell [29]. Phenomena such as wind and snowfall can induce a distributed and alternating load capable of creating fracture points. This happens especially on the surface, mainly in the cells occupying the central area of the module where the greatest deformations occur. Other types of atmospheric agents, such as hail, can instead induce punctual loads on some cells, creating mechanical stresses that lead to crack formation, which usually arise from that point where hail impacted [29]. Many PV modules have been designed and applied for heavy snow load regions, thanks to a snow load test certification. Generally, the inclined surface or top of the module simply allows the snow to fall, but this also shifts the load to the lower parts of the module. Wind and snow have significant impacts on the performance and structural integrity of photovoltaic (PV) modules. High wind speeds can lead to mechanical stress on PV panels and their mounting systems, potentially causing damage such as cracking or displacement [30]. This mechanical stress is particularly critical in regions with frequent storms or hurricanes, where wind loads can exceed design limits. Furthermore, snow accumulation on PV modules reduces their efficiency by blocking sunlight, which leads to lower energy output. While snow typically slides off sloped panels, prolonged snow cover can decrease annual energy production by a measurable margin [30]. Moreover, the weight of accumulated snow adds to the mechanical load on the panels, potentially leading to microcracks or even structural failure in extreme cases. Snow-induced loads, particularly in large volumes, cause bending stress in the PV modules, placing significant strain on the module frame and glass. The glass, typically tempered to withstand impact loads, remains vulnerable to shear stress that can arise from uneven snow loads or thermal expansion, further increasing the risk of cracking [11]. Given the fragility of glass under shear forces, these stresses can result in localized failures, reducing the overall lifespan of the system [31].

3 PV modules imaging techniques and extreme weather tests

3.1. PV modules characterization techniques

To analyze the modules there are many different techniques, each with different response time and limits. Due to its non-destructive and fast measurement technique, Thermography or infrared (IR) imaging, allows to have graphical distributions of characteristic features of PV modules and to find thermal and electrical failures in real time. This technique utilizes the concept of localized heat generation because of the joule effect, caused by poor contacts, shunted cells, or short circuits.

3.1.1. Infra-Red thermography

The main thermal abnormalities which can be detected by IR imaging in PV power plants are:

- Hot spots due to breakage of front glazing, external shading or internal cell problems.
- Heated bypass diodes inside the PV module junction box, due to its activation.
- Heated string fuses in the combiner box, and heated DC and AC cables and connection points.
- The degree of PID degradation by shunts (PID-s).

In general, high temperature gradients indicate strong power loss and inactive areas, while temperature difference in the range of 10°C to 20°C can be considered fine. There are three different types of thermography methods. The most common and applied technique is thermography under steady state conditions, which allows the analysis of PV modules in the field under working conditions. Pulse thermography and lock-in thermography allow a more detailed view of PV modules but both techniques need to be done under lab conditions. [29]

- Steady State: the measurements can be performed during normal operating conditions, assuring that it is done under steady state conditions of the PV module. By means of an appropriate IR-Camera, temperature distribution and temperature differences induced by different light conditions can be measured, comparing different load conditions: at short circuit, at open circuit and at maximum power point. Illuminated outdoor thermography measurements

should be performed on a sunny cloudless day with a minimum irradiation of 700 W/m², and an angle of view sets as close as 90°, but not less than 60° to the module glass plane.

Figure 3.1: IR Imaging with a drone

- Pulse thermography: This method needs an external heat source to generate a dynamic heat flux through the PV module. The instrument used is one or more simultaneous triggered powerful flashlights in front of PV module with an intensity able to raise instantaneously surface temperature from 1K to 5K homogeneously. Then a thermographic camera continuously takes images of PV modules and the resulting pulse phase thermography images will show details of their inner structure. One of the main disadvantages of this method is that infrared detector chip technology is expensive and difficult to use.
- Lock-In thermography: the module is excited and detected at a controlled frequency, to enhance the signal to noise ratio, so that weak heat sources can be detected. In this case cooled IR-cameras in the spectral range from 2 μm to 5 μm, as well as uncooled bolometers from 8 μm to 14 μm are suitable. AS a result of periodic excitation of PV modules which is synchronized with the image recording, thermal differences in the range of 10 μK may be apparent. The necessary excitation of solar cells and modules can be done electrically using a voltage or current source or optically with a light source. The signal is influenced by material properties and various measurement parameters and gives the possibility to identify heat sources and temperature distributions.

3.1.2. UV Fluorescence

When EVA is exposed to sunlight, especially to the UV spectrum, molecules in the encapsulant decompose to form luminophores, which emit fluorescent light, the one recovered in UV fluorescence images. The fluorescent degradation product was found to change to a non-fluorescent product along the edges of cracks in solar cells that are oxidized by oxygen, diffused through the backsheet to the EVA front layer of the module. This effect is called photobleaching and can be used to determine the number,

position and orientation of cell cracks in PV modules, even in a dark outdoor environment. During outdoor measurement, instead, PV modules must be exposed to sunlight to develop luminophores species capable of emitting a sufficient signal. Typically, the longer is the exposure to UV light, the more intensive will be fluorescent emission. To perform the test the camera must be placed perpendicular to the PV panel surface, while a control cell shall be shaded and then illuminated using a white high-power LED with up to one Sun equivalent intensity when on. In this way, the LED enables a very fast periodic modulation of the optical generation rate in the control cell. The images are then sent to the laptop in order to be analyzed. They give the possibility to detect cell cracks in PV cells, which generally appear as dark bars. However, due to bleaching effect at the frame, cracks at the cell edge are not detectable and when grey zones are located along the interconnector, cracks near it are difficult to be identified. [29]

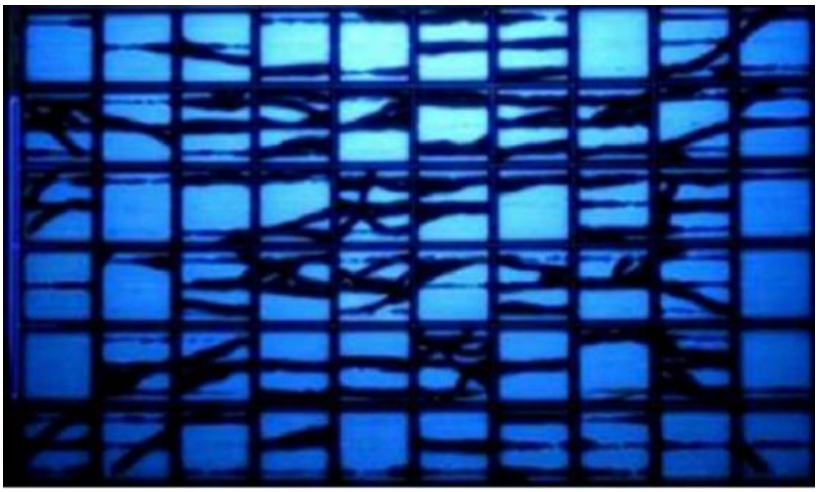

Figure 3.2: UV fluorescence image

3.1.3. Electroluminescence (EL)

In this test the module is supplied by a DC current in forward bias conditions, basically using the module as a bulb, to stimulate radiative recombination in solar cells and detect possible defects thanks to a silicon charged coupled device (CCD) camera [29]. This device can measure photoemission in a dark environment to reduce interfering light. EL imaging is done in a dark environment because the amount of infrared radiation near 1150 nm emitted by the solar module is low compared to the radiation emitted by background lighting, so the dark environment is needed to decrease the background "noise" during EL imaging. Because of these test characteristics, it takes more time than the previously discussed tests to be performed. In addition to that, in multi-crystalline solar cells, crystallographic defects typically also appear as dark lines, therefore the detection of cell cracks by EL imaging is still done by a trained professional since this process has not been automated successfully yet [29]. Electroluminescence test detects defects such as:

- Microcracks
- Shunt faults
- Finger failures
- Potential induced degradation (PID)
- Heavy homogeneous mechanical load (X-crack pattern)

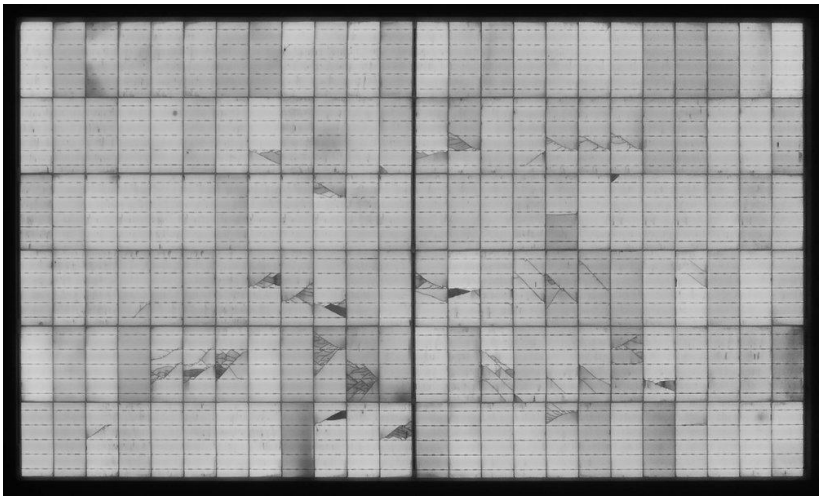

Figure 3.3: EL image

3.2. Extreme weather testing

To ensure resilience against external factors, PV modules undergo thorough testing. The following outlines some of the key tests they must undergo:

3.2.1. Wind load test

Wind load testing is requested to ensure the safety and reliability of PV systems. The test is designed to simulate the effects of wind on PV panels and mounting systems, and to assess their ability to withstand these forces. The test is typically conducted in a wind tunnel, where the PV panels are mounted on a test frame and subjected to a controlled stream of air. The air velocity is gradually increased (up to 61.2 m/s) until the panels reach a critical point of failure. The test is repeated for different wind directions (β = 0°, 180°) and angles of incidence (α = 10°, 20°, 30°, 40°) to ensure that the panels can withstand wind loads from all directions. The results of the wind load test are used to determine the maximum wind speed that the PV panels can safely withstand, the standard value for IEC 61215 is 2400 Pa [11]. In addition to the wind tunnel test, there are several other factors that need to be considered when designing PV systems for wind resistance. These factors include the height and location of the installation, the type of PV panels and mounting system used, and the local building codes. By carefully considering all of those, it is possible to design PV systems that are safe and reliable, even in high-wind areas [32].

3.2.2. Snow load test

The non-uniform snow load test simulates the weight of snow accumulation on the modules and evaluates their ability to withstand the resulting mechanical stress. Due to the inclination, snow will slide down the panel and accumulate unevenly at the bottom edge of the frame, resulting in the lower part of the module needing to withstand greater stress. Additionally, ice may accumulate between the frame and the glass, causing further stress to the PV module. In IEC-62938, non-uniform snow load tests simulate failure types of conditions close to the real application so to reflect real snow impact on the PV modules [33]. The goal of the test is to determine the load limit of the PV module. Six modules are used with five modules tested to their failure limit while the sixth module is stressed with approximately 63% of the mean load of the five modules beyond their failure limit. The modules are initially subjected to a series of tests to ensure they are in good working conditions and are free of defects. This may include electrical tests, visual inspections, and measurements of the module's mechanical properties. Then the snow load is applied to the surface of the PV modules and gradually increased until it reaches the specified test load, (certification is typically for 5400 Pa) or even higher values. The deflection of the PV module under snow load is carefully monitored and measured using specialized instruments such as strain gauges or laser displacement sensors. Then the deflection data is analyzed in order to assess the structural integrity of the module and its ability to withstand the applied load. After the snow load is removed, the PV modules are thoroughly inspected for any signs of damage or deformation that may compromise the module's performance or longevity [34].

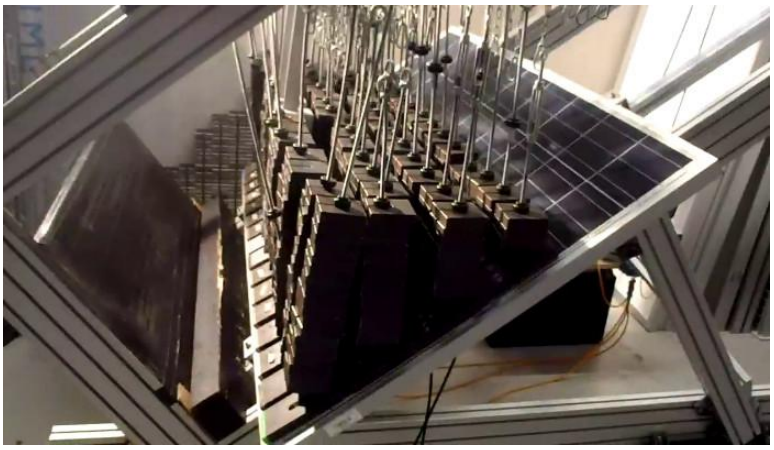

Figure 3.4: Snow Load test

3.2.3. Hail impact test

The hail impact test for photovoltaic modules is governed by two main standards: the IEC 61215, internationally recognized, and the VKF (Vereinigung Kantonaler Feuerversicherungen) standard, specific to Switzerland. Both standards aim to assess

the durability of PV modules under hail impact, but they differ in various technical aspects such as test procedures, impact energies, and certification criteria.

- IEC 61215 specifically addresses the design qualification and type approval of PV modules. Within this standard, the hail test is a crucial component, assessing the module's ability to withstand the impact of ice balls that simulate hailstones. The following are key parameters for the hail test according to IEC 61215:
    - Hailstone size: 25 mm in diameter.
    - Ice ball velocity: 23 m/s.
    - Ice ball temperature: -4 ± 2°C.
    - Ice ball mass: Approx. 7.53 g.

  Test procedure: Ice balls are shot at 11 predefined points on the module, targeting areas such as corners, edges, and the center, which are critical to mechanical stress.

  Impact energy: The impact energy is calculated at 1.99 J.

  Pass criteria: No visible damage to the front surface and no significant degradation in performance (measured by electrical output) is allowed after testing [11].

- VKF Hail Standard was developed by the Swiss Cantonal Fire Insurance Association to evaluate the resistance of building materials, including PV modules, against hail impact in the specific Swiss context. Its test parameters are stricter than the IEC standard, reflecting Switzerland's frequent and severe hail events:

    - Hailstone size: 10 to 50 mm in diameter, depending on the required resistance class.
    - Ice ball velocity: up to 31 m/s for the largest ice balls (50 mm).
    - Ice ball temperature: -20 ± 3°C

  Test procedure: Ice balls are shot at multiple locations of the module with IEC 61215 reference points, additional focus and testing is placed on critical points like edges and corners.

  Impact energy: The maximum energy impact for 50 mm hailstones is 31.5 J.

  Pass criteria: The module must not exhibit any mechanical damage visible to the naked eye. Additionally, the electrical performance degradation must remain within a defined limit (typically 5%) [35].

Parameter	IEC 61215	VKF Hail Standard
Hailstone size	25 mm	10–50 mm (depending on class)
Ice ball velocity	23 m/s	Up to 31 m/s (for 50 mm hailstone)
Ice ball temperature	-4 ± 2°C	-20 ± 3°C
Impact energy	1.99 J (25 mm hailstone)	31.5 J (for 50 mm hailstone)
Test points	11 predefined points	11 IEC points, additional testing on critical points
Pass criteria	No visible damage, no significant power loss	No visible damage, power loss <5%

Table 3.1: Comparison between IEC 61215 and VKF

4 Hail formation and characterization

Scientific evidence confirms that climate change is contributing to the increasing frequency and intensity of hailstorms, as well as the growth in the average size of hailstones. Recent summers, including the extreme hailstorms of 2021, serve as clear and alarming examples of this trend.

Between June 18 and July 31, 2021, Switzerland experienced a series of exceptionally widespread and intense hailstorms, resulting in unprecedented damage to buildings, vehicles, and agricultural land. Insurance companies reported record-breaking losses, with total damages estimated in the hundreds of millions of Swiss Francs. For example, La Mobilière reported 20.000 vehicle damage claims from the June 28 hailstorm alone, while the building insurance company for Lucerne (GVL) processed 18.000 claims (six times the annual average) resulting in CHF 400 million in losses, with over 15% of all buildings in the region affected. Similarly, Schweizer Hagel, an agricultural insurer, received nearly 14.000 damage reports in 2021, with insured compensation exceeding CHF 110 million. These events made 2021 the most expensive year on record for both GVL and Schweizer Hagel, underscoring the increasing severity and frequency of hailstorms [36]. Insurance companies have reported a significant rise in claims as a result of the increasing frequency and intensity of hailstorms across Europe, leading to higher premiums and stricter coverage conditions.

The economic impact of such events extends beyond buildings and vehicles, significantly affecting PV systems, particularly in hail-prone regions like the Alpine area between Lombardy and Switzerland. Even minor hail damage to PV systems, such as cracked glass, can result in repair costs of 100-200 euros per panel, while severe damage requiring full replacement of modules and electrical components can incur costs ranging from hundreds of thousands to millions of euros. These costs include not only the panels themselves but also associated infrastructure. In industrial settings, the additional burden of production downtime can further amplify the financial strain [37]. As hailstorms become more frequent and severe, driven by the effects of climate change, the financial burden on both PV system operators and insurers is expected to escalate. This highlights the urgent need for comprehensive studies on hailstorms and their impacts, particularly on vulnerable infrastructure like PV systems. Understanding the risks and costs associated with hail damage is essential for improving resilience, enhancing predictive models, and developing effective mitigation strategies for the future.

Here are reported the hail report map for Europe in 2023 divided by hail diameter and the relative graphs for hail reports and hail days [48].

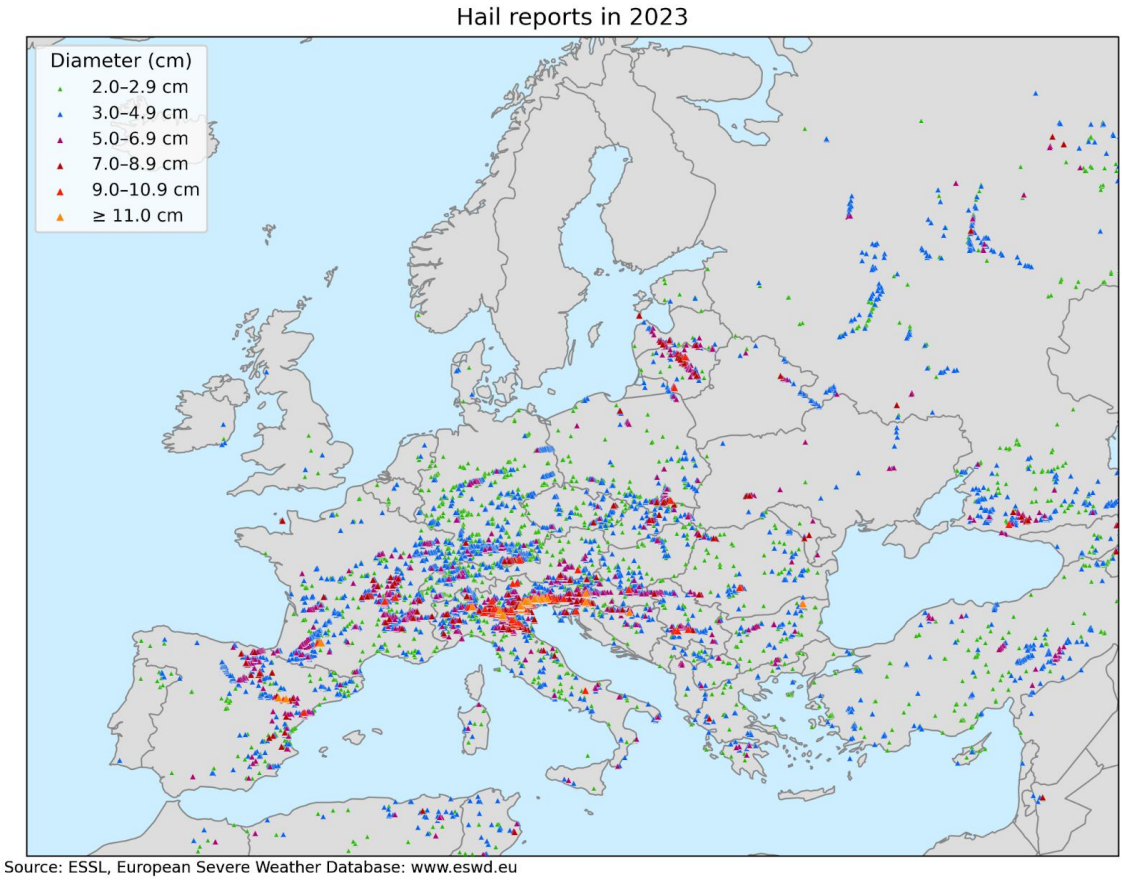

Figure 4.1: Map of reports divided for hailstone diameter

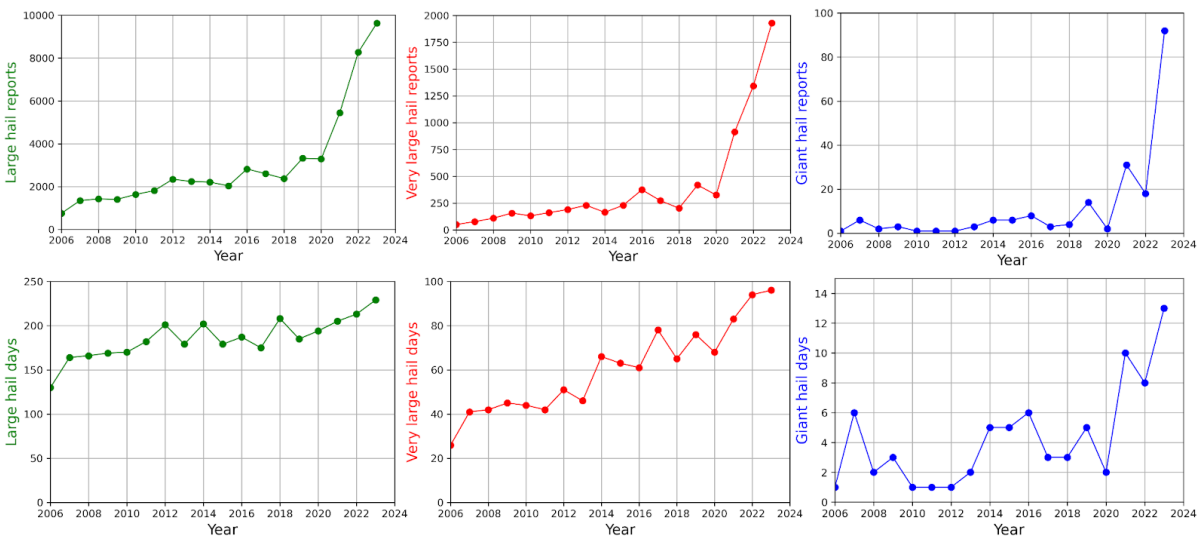

Figure 4.2: Number of reports and days with large (2+ cm), very large (5+ cm), and giant (10+ cm) hail [38]

4.1. Hail Formation

Hail is ice precipitation larger than 5 mm in diameter formed in thunderstorms. Hail particles, known as hailstones, form inside the region of the storm where temperatures are below freezing (around -40°) and there is abundant supercooled liquid water in coexistence with ice particles. Ice particles are drawn through convective storms by their internal winds and can grow quickly in size through collisions with supercooled droplets, which collect on and freeze onto their surfaces. A growing hailstone is kept aloft by strong updraughts (typically, at least 15 m/s) in the storm, until it exits the lifting currents or becomes too heavy to be supported, and falls. Typically, hailstones enter warmer air and partially or completely melt as they fall. When they reach the surface, hailstones exceeding 2 cm in diameter are considered severe and can be destructive. [39]

The processes by which hailstones initiate, grow and melt are called microphysical processes. Convection occurs when air parcels are sufficiently lifted by a triggering mechanism near the ground in a convectively unstable atmospheric cell: triggering mechanisms include local heating or convergent winds, fronts and orographically driven circulations.

The atmospheric cell is considered convectively unstable when the vertical temperature and moisture profiles are such that an air parcel lifted above a certain height - its level of free convection - is more buoyant than its surroundings over a sufficient vertical depth of the troposphere. A parcel lifted above its level of free convection will continue to rise owing to its buoyancy, forming an updraught drawing moist air upwards.

Convective inhibition (CIN) is a measure of the amount of energy that must be supplied for air parcels to reach their level of free convection. Mechanisms for the generation of CIN in lower-atmospheric levels include daytime heating of elevated terrain and differential advection resulting in vertical air-mass stratification, and air-mass subsidence with associated dry adiabatic warming. Moderate CIN is generally favorable for intense deep convection, as it allows for the build-up of stronger convective instability and explosive convective development. If the triggering mechanism is strong enough for the air parcel to overcome the CIN, the parcel will rise and convection will occur. [39]

During the parcel's ascent, the water contained in it cools and condenses into cloud droplets, releasing latent heat and slowing the parcel's rate of cooling, which further increases its buoyancy. The temperature of the atmosphere decreases with height, and the altitude at which the wet-bulb temperature is 0 °C is defined as MLH (Melting Level Height). Above the MLH, condensed water in the air parcel can freeze into ice around nuclei called ice-nucleating particles (INPs). However, while the temperature remains above −40 °C, much of the condensed water in the air parcel will remain in the liquid state and become 'supercooled'. Hailstones grow when hail embryos, which

are typically frozen raindrops or small ice pellets called graupels, collide with supercooled liquid, which freezes onto their surfaces.

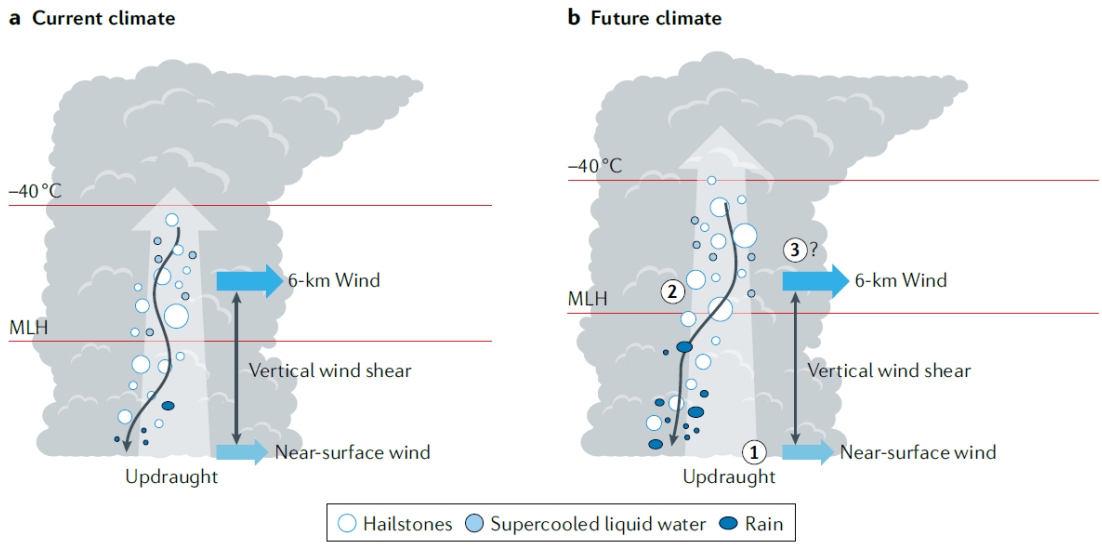

Figure 4.3: Hail formation and expected future conditions

Growth occurs on a continuum between 'dry growth', during which all collected water freezes onto the hailstone's surface, resulting in a low-density layer of air and ice within the hailstone, and 'wet growth', during which some of the water remains liquid long enough to fill any air gaps in the ice before freezing, resulting in ice with a higher density and fewer air bubbles. Dissected hailstones often show multiple layers of different growth types. [39]

Moreover, the concentration of hail embryos can also limit hailstone size, as more embryos competing for the available supercooled water results in smaller hailstones. A large hailstone also requires sufficient time to grow, with the growth time controlled by the updraught strength and the embryo's trajectory through the storm. To become large, the embryo must follow a trajectory that maximizes the time spent in the relatively narrow growth updraught region in which there is abundant supercooled liquid water. [39]

A hailstone can only be supported within the storm while its fall speed is minor or equal to the speed of the updraught suspending it; thus, the updraught speed limits the maximum hailstone size, and the maximum vertical velocity correlates with the maximum size of hailstones that can be produced. As too strong an updraught may eject the embryo out of the high-growth region and most hailstone growth occurs on relatively simple growth trajectories, such as a single pass across the updraught, the production of large hailstones is associated with a broad and moderate-strength storm updraught in which hail embryos can be suspended as they grow. By contrast, abundant supercooled liquid and large numbers of embryos without sufficient updraught strength or growth time may result in large accumulations of small hail. Hail embryo and hailstone trajectories, and, therefore, maximum hailstone size, are

influenced by the lower tropospheric vertical wind shear - that is, the difference in wind velocity with height. Wind shear also organizes the thunderstorm and is crucial to its severity, with damaging hail most likely to occur in supercell-type thunderstorms or organized multicellular convection, both of which require moderate to high shear to form. Studies of hail-favoring environments have typically used vertical wind shear as a proxy variable, and weighted combinations of convective instability and shear indices are often used as a discriminating variable for severe-thunderstorm occurrence. In both Australia and North America, wind shear is at least as important as convective instability for the development of severe thunderstorms. The last important factor affecting maximum hailstone size is the amount of ice melting as they fall below the MLH towards the ground. The smaller the hailstone, the more likely it will melt completely, as larger hailstones are heavier and fall faster; thus, melting during falling shifts the hailstone size distribution towards larger hailstones. [39] Owing to anthropogenic warming, tropospheric water vapor in the future atmosphere is expected to increase by ~7%/°C of warming, consistent with the Clausius–Clapeyron relation. More low-level moisture combined with higher temperatures means that a larger amount of potential energy can be released through the condensation of water vapor in a rising air parcel, thus increasing convective instability. Future projections show expected increases in convective instability over Europe, the USA, Australia and China. Thunderstorm initiation and intensity are very sensitive to low-level moisture and temperature, and the difference between environments with no thunderstorm initiation and those with intense convection can be as small as 1°C in temperature or 1g/kg in moisture content; hailstone size is also highly sensitive to these factors. Greater initial moisture content in thunderstorms is associated with increased hail precipitation rates, and observed and projected increases in hail frequency are linked to increased convective instability. A rise in convective instability is expected to lead to the production of larger hail, owing to stronger updraughts. It is not guaranteed, however, that greater convective instability will always lead to more frequent severe thunderstorms or hailstorms. [39]

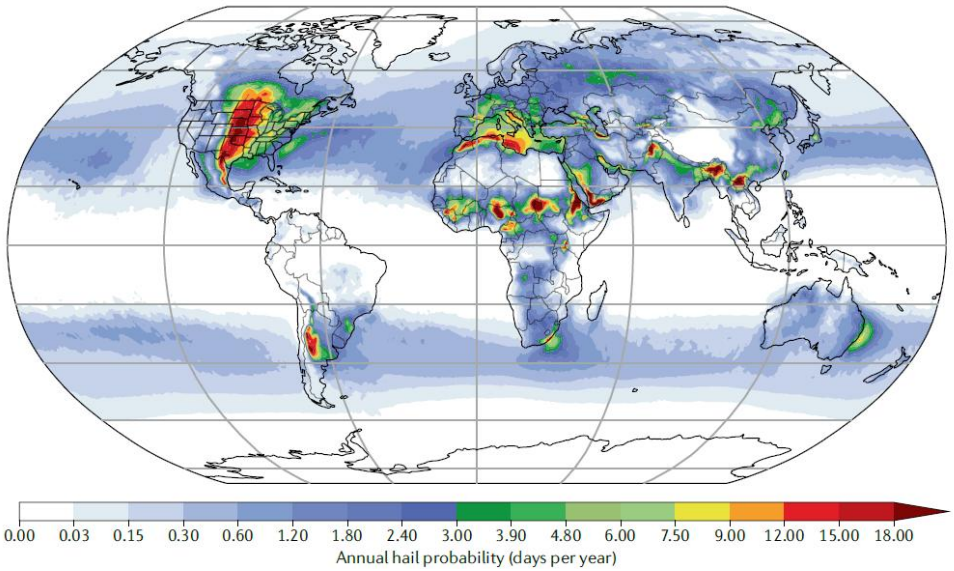

Figure 4.4: Annual hail probability [d/y]

Buoyancy is necessary but not sufficient for convection, and the effects of increasing convective instability on hail can be offset by a coincident change in other hail-relevant variables. For example, a warming of the mid-troposphere can stabilize the lower atmosphere, leading to higher CIN. An increase in overall convective instability can, therefore, be offset by coincident augmentation of the CIN, which can reduce the occurrence of convection and hail. The accompanying rise in MLH driven by this lower-tropospheric to mid-tropospheric warming may also offset the effect of greater convective instability by causing hail that forms aloft to melt before it reaches the ground. Furthermore, greater atmospheric moisture capacity may dampen the updraught strength by making it possible for more condensate to form, even as parcel-based convective instability measures increase. [39] Overall deep-tropospheric vertical wind shear is expected to reduce with climate change, but such changes are difficult to quantify. Expected variations in jet streams and storm tracks that affect large-scale circulation may also have a role in vertical wind shear changes. Despite the importance of wind shear in the development of severe storms, including hailstorms, historical analyses and future projections generally show hailstorm changes that are driven less by changes in wind shear than by changes in convective instability or MLH. This outcome is because changes to wind shear either occur at times when hail is unlikely to form or are outweighed by the relatively greater effect of changes to instability or MLH. Thus, decreases in wind shear generally do not inhibit expected increases in the occurrence of thunderstorm environments driven by rising convective instability. In Europe, wind shear may instead increase when convective instability is high. The atmospheric INP concentration is related to the temperature and aerosol concentrations, but high uncertainty in the simplified relationships used to model ice nucleation has hampered attempts to link predictions of future aerosol concentrations to predicted future INP concentrations and their effects on microphysical processes. In

the warmer troposphere, convective cloud base temperatures and liquid water content may both increase in the future. [39] Such increases could affect hail-growth types by allowing for more supercooled water above the MLH and encouraging the wet growth of larger, denser hail. The amount of hailstone which melts below the MLH depends on the particle's size and density and the relative humidity and temperature profiles, as well as the timespan during which it melts while falling. Increased MLH has led to a shift towards fewer small and more large hailstones in observations in China and France. Changes in hailstone-size distribution affect melting and evaporation rates, downdraught strength and cold-pool intensity, which influence the amount of surface hail and even the storm structures produced. Increased melting may reduce surface hailfall, even if hail production within storms increases. However, because melting rate grows with increasing relative humidity, any reduction in relative humidity of the sub-cloud atmosphere may offset the effects of increased MLH to some degree.

To summarize, it is broadly expected that increased atmospheric temperature and low-level moisture will lead to increased instability, storm updraught strength and liquid water content, all of which support the formation of larger hail; a rising MLH will increase melting of smaller hail; and vertical-wind-shear changes are unlikely to strongly affect hailstorms. These changes underpin expectations that hail frequency at the ground should decrease with time, with larger hail becoming a more common occurrence. [39] Here are presented hail damage caused during the 2023 summer and record size hailstones coming from those recent events.

Figure 4.5: Hailstorm damages in Italy [38]

Figure 4.6: Giant hailstone observed in Italy [38]

Studies that use proxies to identify future environments favorable for hail in Europe mostly project a (slight) increase in hail likelihood. For example, an ensemble of 14 regional climate models (RCMs) shows environmental conditions conducive to severe hail becoming 40–80% more likely across large parts of Europe by the end of the century in a high emissions scenario. Moreover, the likelihood of very large hailstones is estimated to double over parts of central and northern Europe by 2100. In Italy (2004– 2040), one coarse-resolution global-climate simulation projects an increase in hail frequency for spring, summer and autumn. Expected future changes to hailstorms

in Europe are primarily attributed to an increase in convective instability resulting from greater low-level and mid-level atmospheric moisture content. [39]

The composition of hail, which also influences the formation of giant hail, has also been analyzed. Comprehensive elemental analysis attributed an excess of Ca-ions to hail formation. By following the movement of air masses prior to the storm, they estimated that the composition of the hail was a consequence of extensive agricultural activities. The formation of hailstones has also been linked to airborne soil organic matter, where biotic factors have been shown to affect nucleation. Bacteria have been found to catalyze freezing at warmer temperatures, thus influencing weather. The bacterial community in hailstones is typically diverse. Strains from *Actinobacteria* (23 %), *Planctomycetes* (11 %), *Bacteroidetes* (14 %), and *Gammaproteobacteria* (12 %) were the most abundant. Of the latter class, *Pseudomonas syringae* was recognized as important in the formation of larger hailstones. Another important component in the air masses is fragments of terrestrial plants. They have been identified as critical vectors for the bacterial community in the atmosphere, but little is known about their impact on hail formation. Of even greater concern and omnipresent are microplastics. Optical microscopy revealed the presence of particles larger than 50µm. The concentration of fibrous particles of anthropogenic or natural origin was more than four times higher in the largest hailstone and at least twice higher in the cores of the hailstones than in their outer layers.

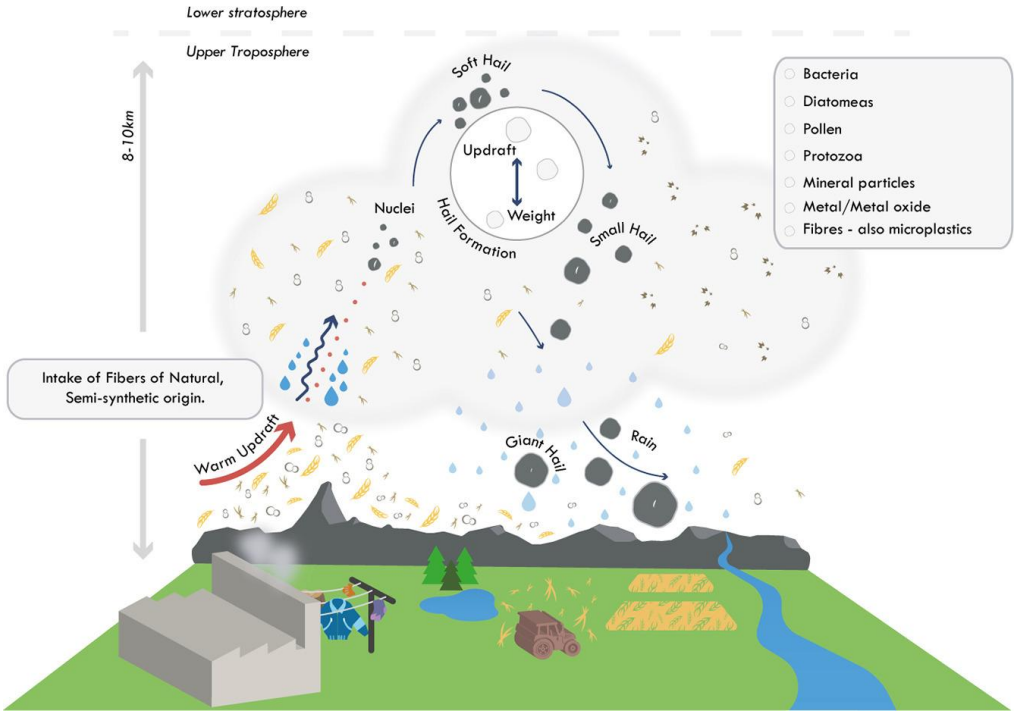

Figure 4.7: Natural and synthetic particles influence in hail formation [40]

The highest concentration was measured in the core of the largest hailstones. In smaller ones were also detected fewer fibers in the outer layers compared to the largest ones. The fractions of the identified sand particles that appeared rounder showed the

opposite trend. The number decreased from the outer to the inner layer, while we could hardly find any in the core of the largest ones. [40]

The initiation of hail growth begins with ice nucleation; a recent study shows that cellulose, a possible constitute of the identified fibers, forms ice nuclei at a lower concentration than desert dust. Such conditions could be readily achieved higher in the atmosphere where a small number of lightweight fibers are sufficient to initiate the growth process. The investigations showed that >90% of the fibers consist of lignocellulose, lignin, and/or cellulose, which suggests they were of natural origin. However, cotton used in clothing also consists of pure cellulose, and dyes are commonly added. Among the particles analyzed, fibers with a polymer origin were also identified. Clothing fibers are similarly braided, containing mixed synthetic and cotton components. [40] The giant hailstones (GHs) carried diverse microorganisms, some of which can nucleate ice, and fibers of natural and anthropogenic origin, among which cellulose has been shown to initiate nucleation. The cores of the GHs consisted mainly of fibers, while small, more spherical particles made up the outer layers. Although performed on a small liter scale, the findings are consistent across all samples and probably reveal an important aspect of the microphysics of a single hailstone. Fibers detected in the GHs were mostly of natural origin and attributed to plants, but some were identified as microplastics and other man-made products that could have additionally affected the glaciation processes in the clouds. Studies suggest that increased concentrations of fibers in the atmosphere, a consequence of man-made activities, could be associated with the formation of GHs. This prediction is supported by the notion that, consistent with the increase in annual GHs reports over the past 30 years, anthropogenic microfiber pollutants have been accumulating in the Earth ecosystem for >70 years. Since the deposition of (semi)synthetic microfibers is high near urban and industrial areas, air masses passing over such an area could increase the risk of giant hailstone formation. [40]

4.2. Hail Texture

Ice in hailstones is characterized by a hexagonal crystallographic structure and an optical birefringence. The long axis of the hexagonal structure, the c-axis, is also the optical axis.

The hailstones show two main characteristics:

- they are structured with several concentric layers composed of alternating fine equiaxed grains and coarse elongated and radially oriented
- they show two texture types with c-axes oriented either parallel or perpendicular to the radial direction.

Such textures are compared with the ones observed in 2 different textures of lake ices, identified as S1 and S2 in the study by M.Montagnat et al. [41]. The S1 type (with c-

axes parallel to the columnar crystals that grew in the radial direction) may result from epitaxial growth from a polycrystalline embryo, while the S2 texture (c-axes in the plane perpendicular to the column direction) may result from the growth from an embryo made of a few crystals with mainly one crystallographic orientation. [41] The core of the hailstone is composed of a large grain surrounded by several smaller grains. A close look at the intersection between the core and the first layer reveals that this layer starts from a fined-grained area, and a porous area with large pores is observed at the transition. This layer is composed of large grains elongated in the radial direction, which is the assumed growth direction. In this coarse-grained layer, the texture is anisotropic, with c-axes oriented preferentially in a girdle perpendicular to the thin section plane. The second layer is a fine-grained layer. This layer is made of small grains, many of them too small to be oriented. The last layer is composed of large, more equiaxed grains, also characterized by a girdle-type c-axis distribution. In this layer, some of the large grains have their c-axes oriented in the growth direction, and some are oriented perpendicular to this direction. All hailstones studied are composed of concentric layers with different grain size, morphology and texture. [41]

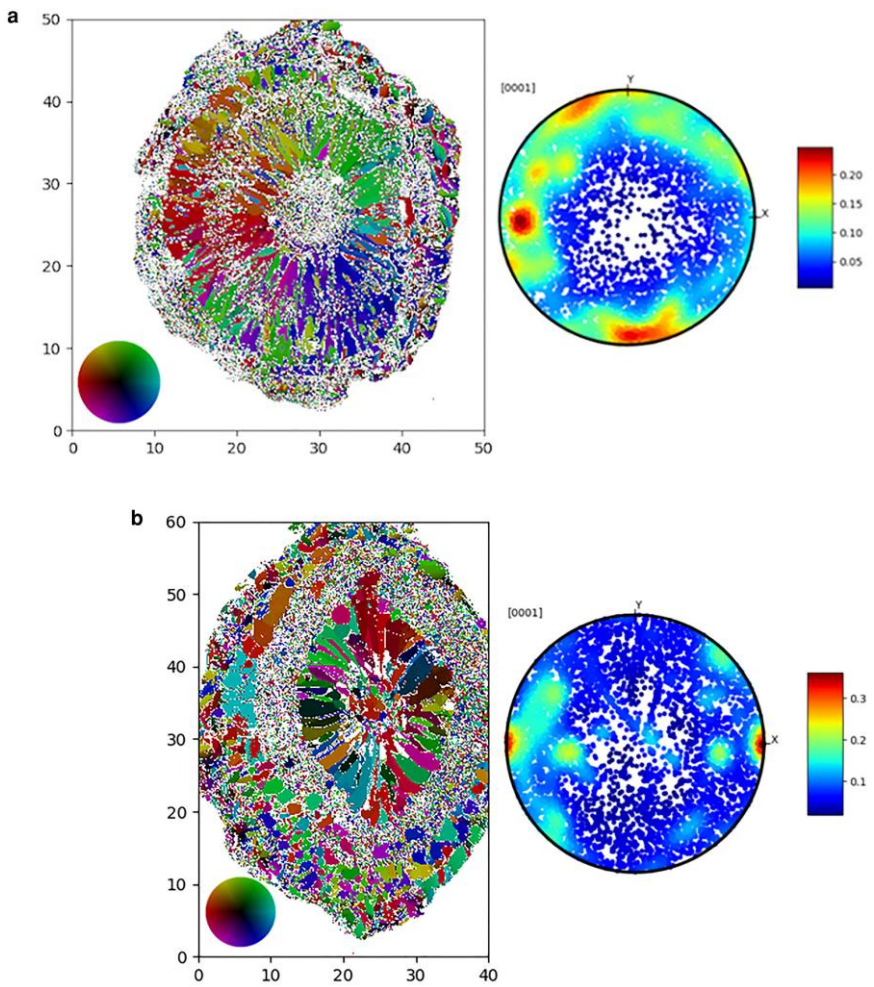

Figure 4.8: Stratification and c-axis orientation in different hailstones [41]

High-resolution measurements of c-axis orientations and microstructures reveal two specific textures.

The first type of hailstone includes samples composed of a nearly single-crystalline core, surrounded by a layer with large grains with c-axes oriented tangentially, perpendicular to the growth direction. These specific crystalline orientations and morphology are comparable to the S2-type lake ice described before. The c-axis orientations would result from a selective growth process, known as competitive growth or survival of the fastest. A closer look at a few individual grains shows that both radial and tangential orientations are present. Based on the grain size observation, is assumed that this is the result of the rapid freezing on the hailstone surface of supercooled droplets present in the cloud, very likely under dry conditions. Observations seem to show that grain orientations present in this fine-grained layer could have impacted the crystalline orientations of the following layer by playing the role of seeds.

The second type of hailstone also presents several layers but with another arrangement. The large grains are characterized by c-axes oriented in the direction of growth. The microstructure of the core is composed of small grains. From this core, the growth process in the subsequent layer seems to have favored a specific texture with c-axes oriented radially along the growth direction. Such a specific texture is shown to result from an oriented seed-based growth, under still conditions. [41]

Crystal growth during hailstone formation could therefore follow mechanisms similar to those well documented for S1 and S2. The conditions necessary to meet S1-type ice (c-axes oriented in the growth direction already present in the seed, and still growth conditions) seem to be satisfied in hailstones within which the girdle-type texture observed in the fine-grained core (very likely resulting from a low porosity graupel embryo) provides the necessary seed orientations for the growth of grains with c-axes in the radial direction. The large dimension of these radially oriented elongated grains, and the low porosity (transparent ice), must result from relatively undisturbed and slow growth conditions. On the contrary, these conditions do not seem to apply to other hailstone types since the core is formed of a limited number of crystals with similar orientations (very likely resulting, in this case, from a freezing droplet embryo). Among all hailstones studied in [41], those with an S2-type texture had cores containing only a few large grains. Spongy wet growth has been identified as a relevant mechanism for the formation of large hailstones for a long time. During wet spongy growth, the hailstone is surrounded (partly or completely) by a liquid water layer resulting from its interaction with droplets in the cloud. [41]

4.3. Hail characteristics

The masses of measured hailstones are found to be 50% of the mass of solid ice spheres, considerably lower than ones of solid ice spheres, usually taken into account during testing procedures. This lower mass could, in part, be due to liquid water draining out of the hailstone cavities between impact with the ground and measurement. The equivalent spherical diameter D_{eq} is the diameter of a frozen spherical particle of the same mass. We find from our data that the ratio of the equivalent spherical diameter to the maximum physical diameter (the diameter of the largest dimension of the hailstone) decreases with increasing size. The giant hailstones are consistent with this trend. Small graupel deviate significantly from solid ice spheres, because of having high ratios. The extreme form of these partially melted graupel that fall to the ground at near-sea level altitudes would be large raindrops. They maintain nearly their same physical diameter, with some melting, but move up toward the solid ice sphere curve. [42]

A measure of how circular the hailstones are is given by the parameter "area ratio"; this ratio is the ratio of the cross-sectional area of the particle to the area of a circle with the same maximum dimension. With increasing size, the area ratio decreases slightly, on average. The terminal velocity of an ideal hailstone is calculated as:

$$V_t = \sqrt{\frac{4\delta_{hail} D_{hail} g}{3\rho_{air} C_d}}$$

where δ is the ice density [kg/m^3], g is the acceleration of gravity [m/s^2], ρ_{air} the air density [kg/m^3] and C_d the drag coefficient [-]. For hailstones, measured values of terminal velocity are below the expected values for solid ice spheres for sizes below about 20 mm and is close to it for sizes above 20 mm. Therefore, the terminal velocities of the hailstones should be lower than those for solid ice spheres at the smaller sizes, approaching those of spheres for the larger sizes.

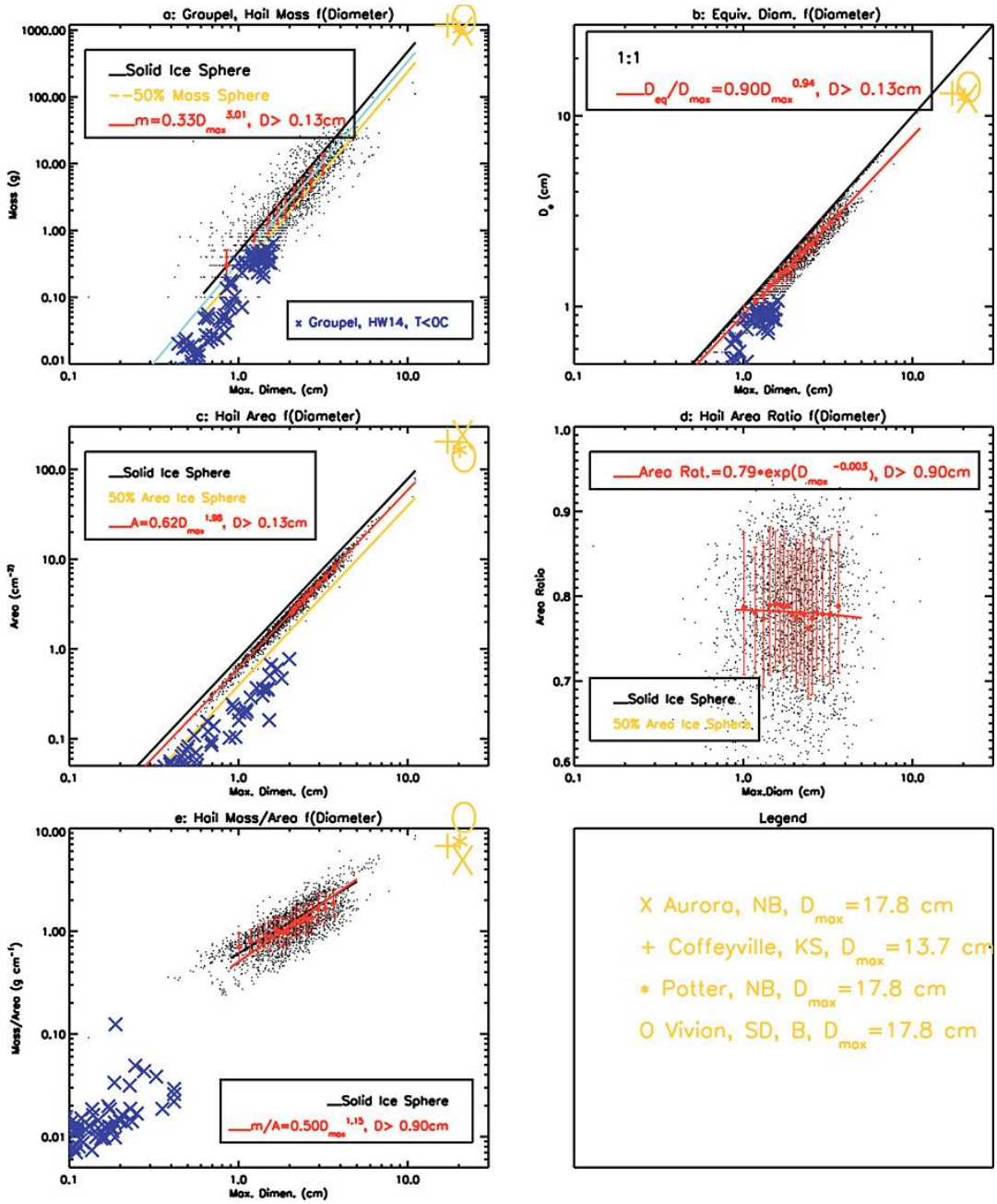

Figure 4.9: Data from hail characterization study [42]

The terminal velocities of the larger hailstones, however, depart from the curve, consistent with their departure from sphericity. Also note that at a given size, there is considerable variability in the terminal velocities, resulting from the variability in stone masses and cross-sectional areas, which reflects the underlying statistical variability in the growth processes.

The KE shown as a function of the major diameter for small diameters is noted above the Laurie curve in Figure 4.10, but then KE curve from measurement crosses the Laurie curve, toward lower relative values for sizes greater than about 2 cm.

The giant hailstones also follow the same trend and reside below what would be expected using the Laurie curve. If equivalent diameter is used, data converge toward the curve with very good agreement at sizes above 2 cm, including the giant hailstones. This result shown in Figures 4.10 and 4.11 argues that hailstone shapes and their associated masses and areas must be considered to produce a more complete picture of hailstone kinetic energies and subsequent damage relationships. It is important to consider the variability of the kinetic energy at a given size, due to variability in their masses and areas.

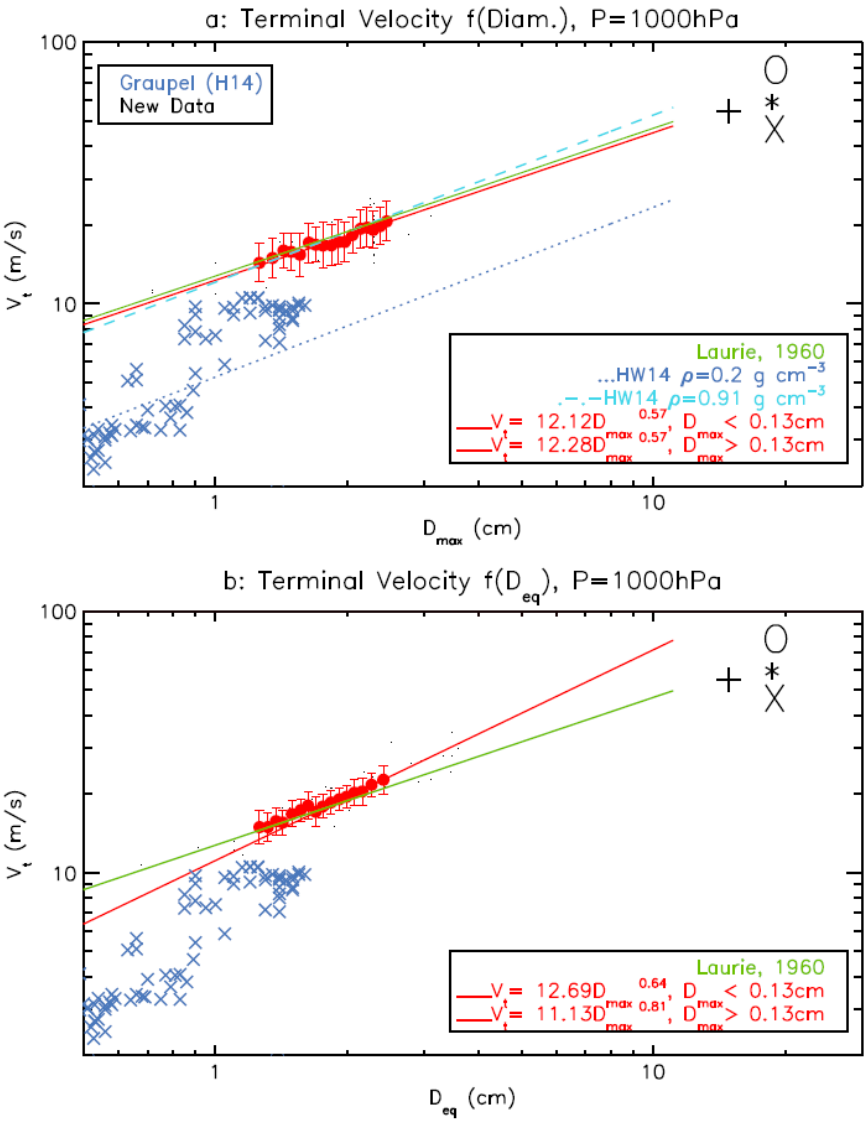

Figure 4.10: Terminal velocity per D_{max} and D_{eq} [42]

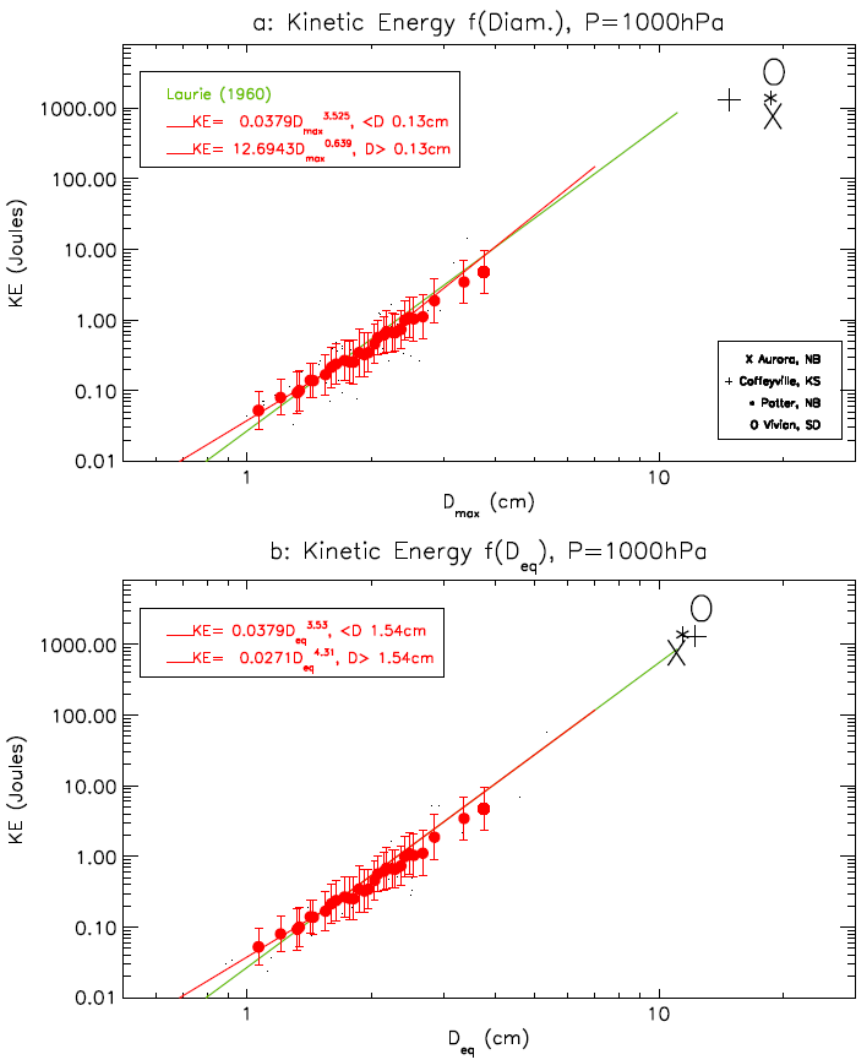

Figure 4.11: Kinetic energy per D_{max} and D_{eq} [42]

At a particular size, it is hailstones with the highest kinetic energy that presumably produce the most severe damage for a given impact (The true damage potential is also related to the concentration of hail on a given surface area and the size distribution). For sizes <3 cm, data suggest that hailstones will, on average, have a larger kinetic energy than that shown by the curves. Above this diameter, the curve will overestimate the average KE for what would be considered the most damaging hail. The giant hailstones fit within the extrapolated curves for the 20 to 80 percentiles. The equivalent diameter for these giant hailstones illustrates the importance of accounting for the shape of hailstones in any application that makes use of V_t and KE. [42]

4.4. Characterization of impact

The conventional way of monitoring forces in an impact experiment is using load cells, or accelerometers. A load cell is usually placed behind the target in an impact test in order that the measuring device is shielded from direct contact with the impactor. Alternatively, impactor materials such as ice balls have been directed at a thin plate which was instrumented with strain gauges at the back to monitor the response behavior of the plate as a target. With these experimental setups the amount of force recorded by the load cell, or inferred from strain gauge readings, is strictly speaking not the maximum contact force generated by the impact given interferences by inertia forces derived from the motion of the target when struck. [43]

The model for the evaluation of the impact forces is based on a two-degree-of-freedom spring connected lumped mass which comprises the frontal mass (m_1) representing the ice impactor cruising at velocity (v_0) and a rear mass (m_2) representing the target. The stiffness of the frontal spring for modelling the interaction of the ice specimen with the surface of the target is modelled as non-linear visco-elastic, while the rear spring in this model has linear elastic properties (with stiffness k_2) to emulate the flexibility of the target. The governing equation characterizing the non-linear force–displacement (or force-indentation) relationship of the frontal spring can be written as:

$$F_c = k_n \delta^p + D_n \delta^p \dot{\delta}$$

where Fc is the contact force generated at the point of contact; k_n is the non-linear stiffness coefficient; p is the exponent characterizing the non-linear behavior of the spring (taken as 1,5 by Hertzian contact theory); D_n is the damping coefficient; δ is the indentation of the impactor into the surface of the target expressed as the relative displacement and $\dot{\delta}$ is the rate of indentation expressed as the relative velocity defined by:

$$\delta = x_1 - x_2$$

$$\dot{\delta} = \dot{x_1} - \dot{x_2}$$

where x_1 and x_2 are the time-dependent displacements, and $\dot{x_1}$ and $\dot{x_2}$ are the time-dependent velocities, of the impactor and target, respectively, during the impact. [44]

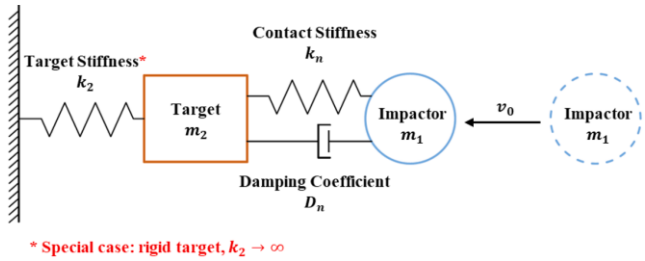

(a)

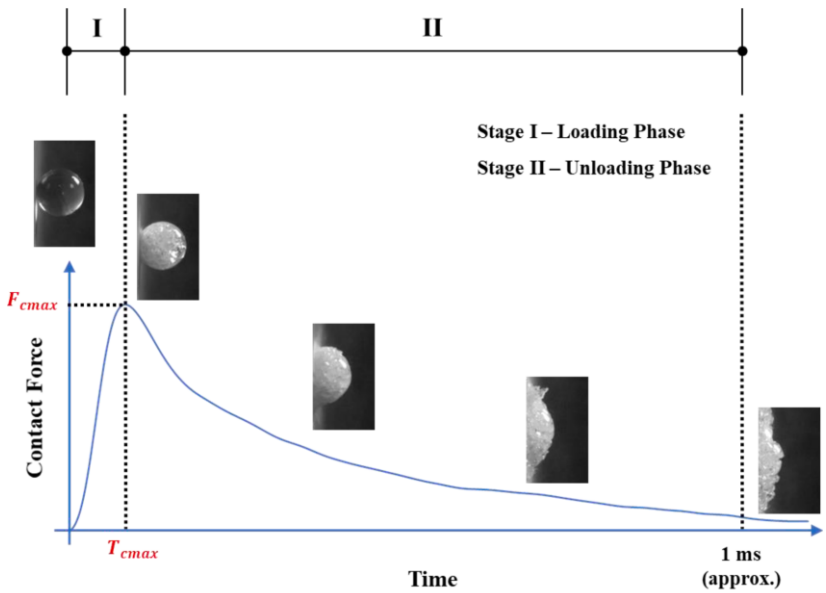

(b)

Figure 4.12: Analytical model and impact phases [44]

The time instance when the ice specimen makes initial contact with the surface of the rigid target marks the start of Stage I (the loading phase) of the impact. In a matter of less than half a millisecond, the magnitude of the contact force increases monotonically until reaching the peak. Crack initiation and propagation was observed to occur in the ice specimen changing its internal structures as shown by the high-speed camera capture. Cracks were initiated at the frontal face of the ice sphere which was in direct contact with the target. Cracks soon propagated rapidly to the rear part of the sphere. This is evident by the initially clear and transparent appearance of the sphere (at t = 0 μs). A milky and translucent appearance of the sphere was seen as the contact force reached the peak. During the process, internal bonding within the ice specimen ceased to remain strong and could diminish abruptly. As a result, the inertia force delivered by the impact was lowered, as only part of its mass was engaged in the (almost) instantaneous transfer of momentum to the target. [44]

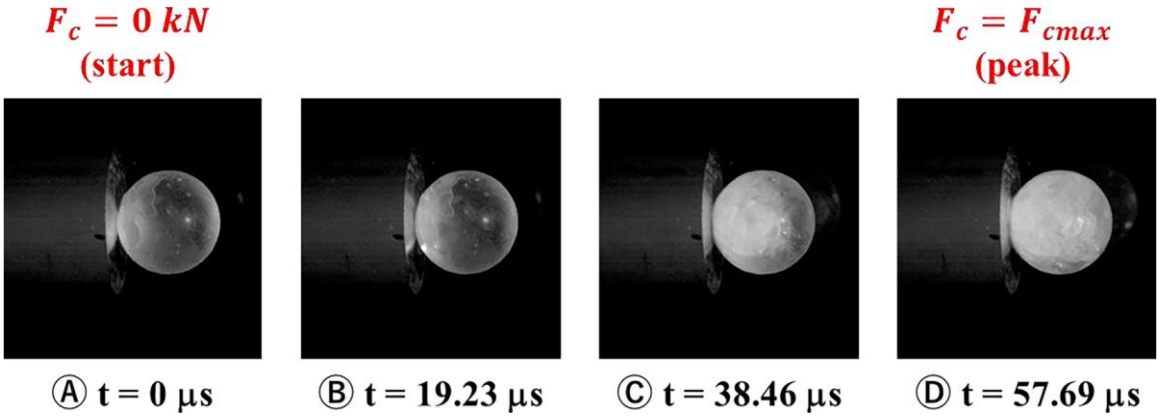

Figure 4.13: Loading Phase [44]

As soon as the contact force reaches the peak, Stage II (the unloading phase) of the impact commences. While unloading, which takes approximately 10 times the amount of time for the loading to occur, the ice specimen starts to disintegrate into tiny debris and then spread radially. As this happens, the contact stiffness (k_n) experiences substantial reduction. [44]

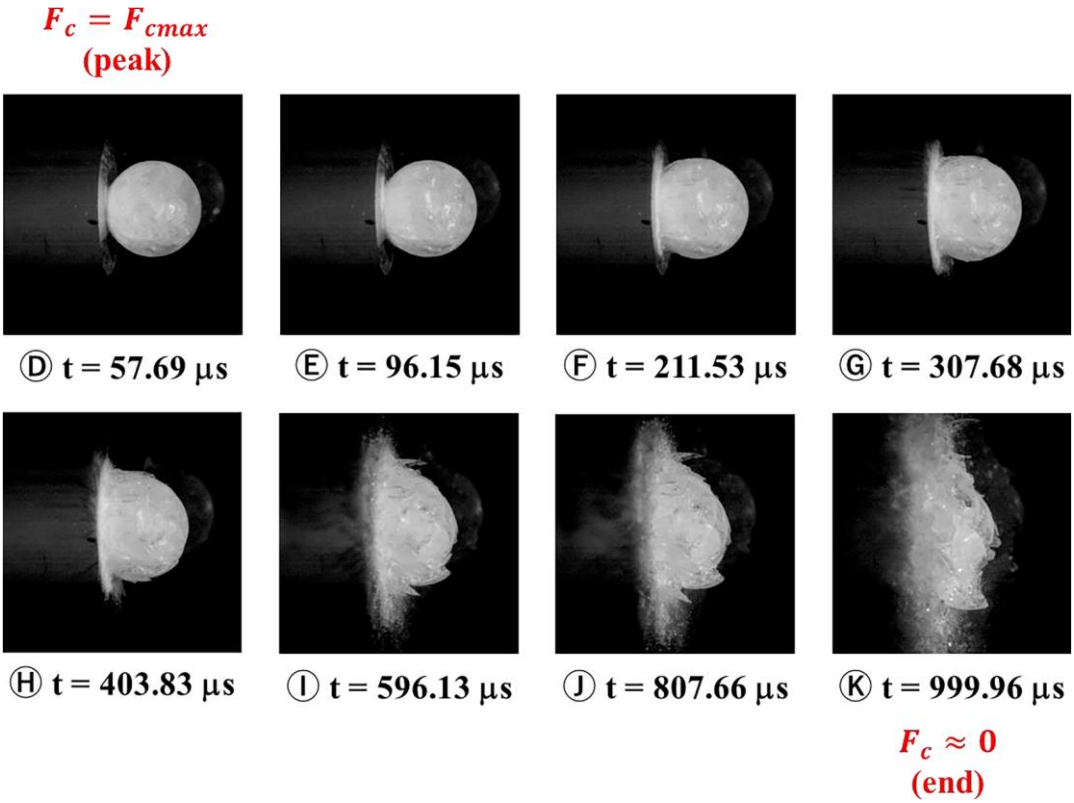

Figure 4.14: Unloading phase [44]

The study of fracture mechanics of hailstones and iceballs is complicated by shape, surface roughness, and material types. The shape problem is due to spherical or oblate objects that are not typically used in materials testing. The stress/strain curve created by plotting σ_c against strain (ε) has numerous points defined by the shape or change of slope of the curve. The shape makes hailstone and iceball tests unique among

materials testing professionals. Factors such as the ratio of dry to wet growth (e.g., clear ice, opaque ice, and trapped bubble structures), the mean growth layer temperature, and other environmental conditions will also affect the compressive strength. As the hail diameter increases, F_o becomes more uniform. The average F_o increases with diameter, too. These trends show that as hail grows larger, it tends to be stronger and more uniform. One probable reason for the increase in F_o is that it is proportional with the increase in diameter; the hailstone structure type is also a probable reason. Large hail is sometimes formed by cyclic growth produced by cycling up and down in the updraft/downdrafts of the cloud cell. With each cycle, growth rings form inside the hailstone. All hail growth varies between dry and wet growth types; dry growth freezes on contact, while it takes longer for wet growth to freeze, allowing dissolved gases time to escape. [45]

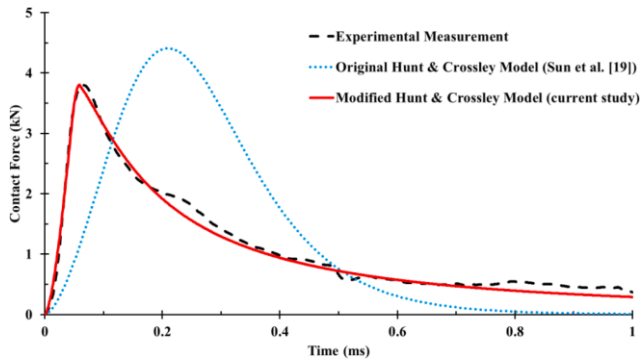

(a)

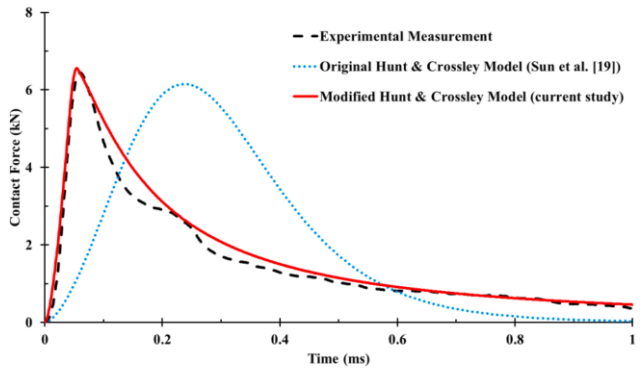

(b)

Figure 4.15: Numerical vs experimental results

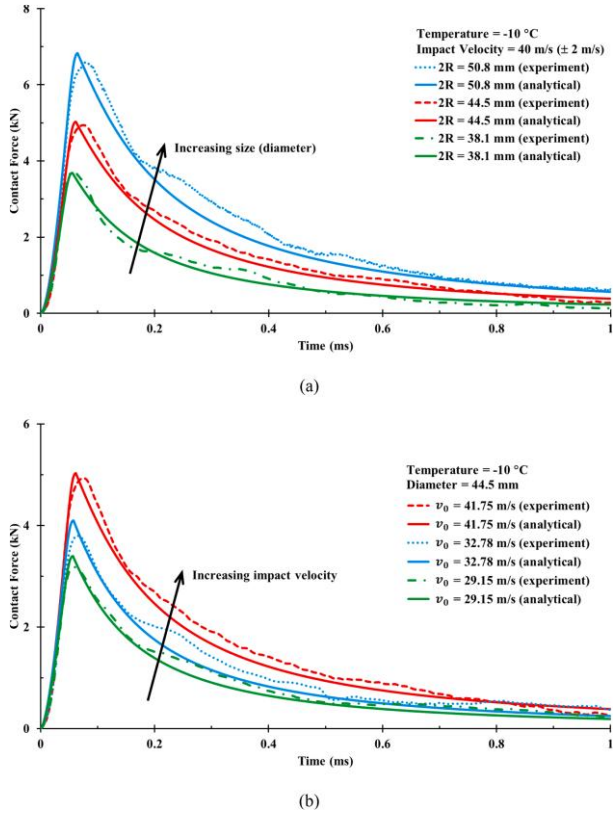

Figure 4.16: Influence of velocity and diameter

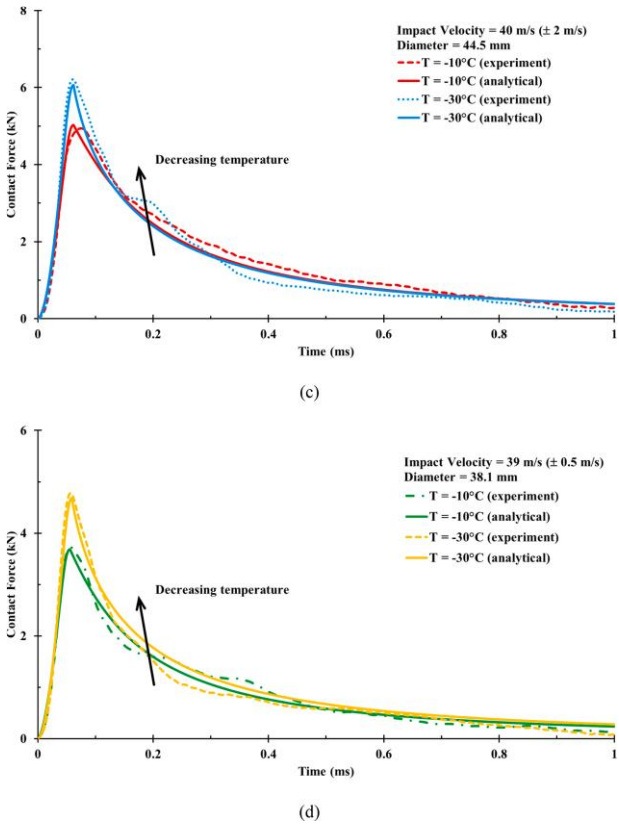

Figure 4.17: Influence of temperature

Another interesting observation is that the spread of the data for uniaxial σ_c and peak F_o is reduced with increasing diameter. This is further evidence that small-hail F_o is much more variable than larger hail, because crack length must increase as hail grows larger; hail structure, with cyclic growth, results in compressive load increases, and the variance of the data is reduced. [45] The data collected provides reliable evidence of the F_o of natural hailstones. Comparison between this data and the one collected from measurements of iceballs (often used in impact tests) provide reliable evidence that F_o is higher for pure ice than natural hail. Both hail and iceball data sets were collected using similar instruments and methods. The relationship between hail and iceballs allows investigators, engineers, meteorologists, manufacturers, testing labs, and educators to mathematically relate natural hailstones to iceballs.

5 Experimental setup and test methodology

All the tests made during the experimental activity have been performed at the PVLab of SUPSI (University of Applied Sciences and Arts of Southern Switzerland) located in Mendrisio, Switzerland. The PVLab (Photovoltaic Laboratory) is an accredited laboratory specialized in the characterization of PV modules, with a strong focus on performance and reliability. The lab offers a comprehensive range of tests, including current-voltage measurement, electroluminescence, insulation resistance, and advanced environmental stress tests such as *"Damp Heat"*, *"Thermal Cycling"*, *"Hail Resistance"*, and *"UV exposure"*. In the following chapter all the equipment and setups for the test correlated to the experiment will be briefly described.

5.1. Darkroom and characterization tests

Characterization tests like "*Visual Inspection*", "*Photoluminescence Imaging*", "*Electroluminescence*" and "*Power Measurement at STC*" are all performed inside the darkroom with very specific setup. The darkroom is a room whose walls are coloured with a specific black paint able to reduce the reflection of light and IR waves, in order to minimize the external noise on the measurements and picture of the tested modules. The darkroom is divided in two sides: at one side all the equipment for the PM_STC and on the other side the one for VI, EL, UV.

The most important tool for the PM_STC test is a solar simulator called PASAN III B; its purpose is to generate a pulse of light (also called flash) with a spectrum the most similar possible to the solar spectrum. At STC the flash irradiates around 1000 W/m^2. For each power measurement, multiple flashes are needed, while an electronical load sets the voltage, so that the I-V curve can be estimated. Each flash is a 10 ms pulse and requires 30 s of recharge time, in order to maintain the cell temperature under control and reduce Xenon lamps degradation. According to IEC 60904, the flasher results as A+, A+, A+ category, which is the highest achievable category, in Spectral Matching, Spatial Non-Uniformity and Temporal Instability. Power measurements are performed with a repeatability of 0.5% and best uncertainty of measurement of 1.6%.

Category	Classification	Criteria
Spectral matching	A+	Spectral match of all bins 0.875-1.125
Spatial non-uniformity (S)	A+	$1\% < S < 2\%$
Temporal instability	A+	$STI \leq 0.25$, $LTI \leq 0.1$

Table 5.1: Classification criteria for PASAN III B

In addition to that, for this measurement are needed a mounting structure for the module and a PC to start the measurement and compute the data collected.

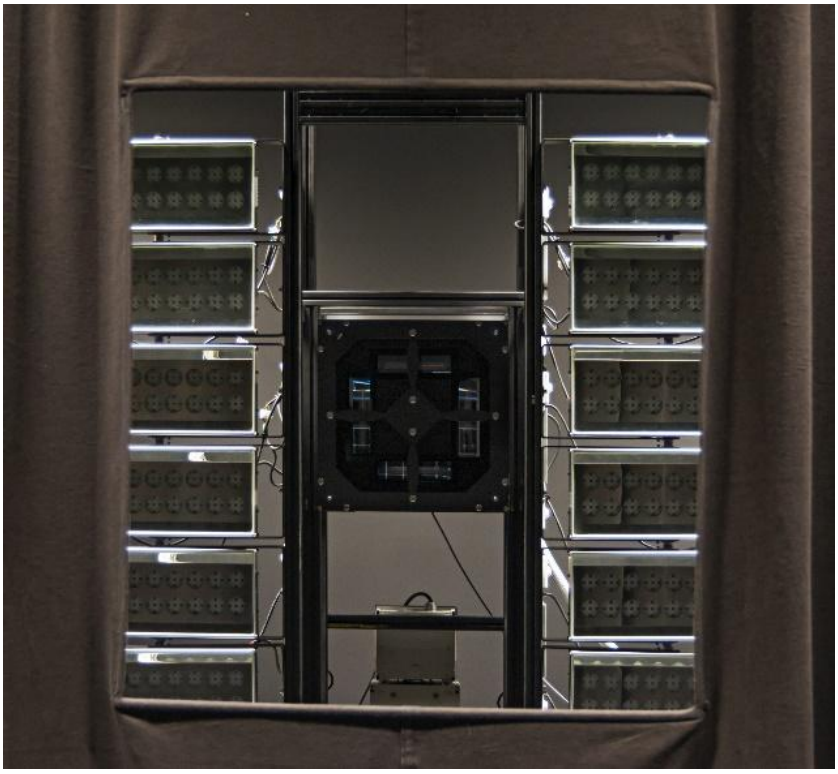

Figure 5.1: PASAN III B solar simulator

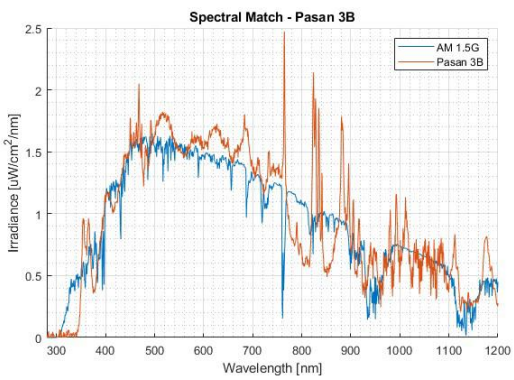

Figure 5.2: PASAN III B spectral match

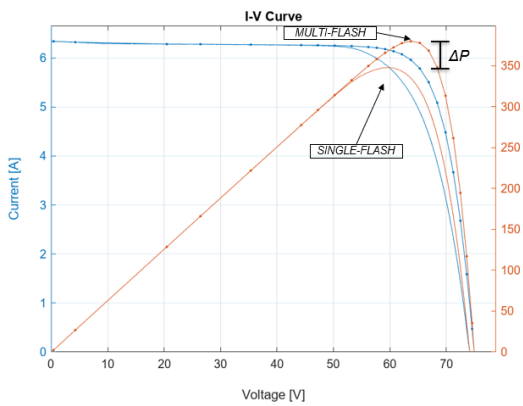

Figure 5.3: I-V curve estimation

Regarding VI, El and PL, the important tool for these tests is the high-resolution multispectral camera PhaseOne® iXM-MV150 , with a resolution of 150Mpx, equipped with a Linos 60 mm f/4 lens and manual focus. Once adequately positioned the camera and adjusted the focus (PL/VI and EL requires different focus because of the different wavelength emitted or reflected) different equipment is needed for the tests. VI requires two flash units positioned at 45° angle to the surface of the module to reduce glass reflection; a color checker table is also positioned close to the module for the digital color correction of the taken picture. The specific equipment for the PL is composed of 4 UV lamps (positioned 45° angle to the module too) and UV filter to reduce the reflection of the radiation on the front glass of the module. At last, the setup for the EL just requires of a power supply connected to the module (needed to make the module emit IR radiation). For all the three tests are also needed the mounting structure for the modules and a laptop connected to the camera to take pictures and elaborate them digitally.

Figure 5.4: EL test station in the darkroom

Figure 5.5: High-resolution camera

Figure 5.6: Objectives

During the HAR runs, with the scope of analyzing the formation and evolution of the cracks, EL images have been taken after each shot. For this reason, the setup for the EL must be changed drastically. First, the high-resolution camera must be moved outside of the darkroom, in proximity of the HAR testing equipment. For this purpose, the camera must be equipped with an IR filter, in order to reduce the effect of natural light on the picture. Lastly, a power supply for the EL is needed.

5.2. Static mechanical load test and equipment

The purpose of this test is to determine the ability of the module to withstand a minimum static load. The minimum required design load for a particular site will depend on construction, applicable standards, building codes, probability of event occurrence, design assumptions and location/climate and might require higher sampling rates and other safety factors. The test must be conducted at 25±5°C in a relative humidity not exceeding 75%. A standard test is composed of three cycles, each of them divided in two steps; the first one is a push test (for at least 1h) while the second step applies a pull pressure, both on the front glass of the module. It's possible to apply a push pressure during the second, but the force must be applied on the back side instead.

The testing apparatus is mainly composed of a rigid base which enables the modules to be mounted, that it's allowed to deflect freely during the test, instrumentation to monitor the electrical continuity of the module during the test, a system made of 15 suckers able to reach up to 15000 Pa of pressure (to be distributed uniformly on the module) and able to keep this pressure (pull or push) for a continuous time.

Figure 5.7: Mechanical load test

5.3. Damp heat test and equipment

This test is designed with the scope of determine the ability of the module to withstand the effects of long-term penetration of humidity. The only requirement for this test is a climatic chamber able to maintain a temperature of 85±2°C and a relative humidity of 85±2% for a test duration of 1000±48h.

5.4. Hail resistance test and equipment

To have a better understanding of how the hail tests are performed, this chapter will provide a brief description of the methodology to be followed according to currently valid normative (IEC 61215 or VKF one for Swiss territory). The equipment required for the test is mostly composed by the structure for the correct mounting of the module, the air cannon for shooting the ice balls and all the measuring and preparation setup.

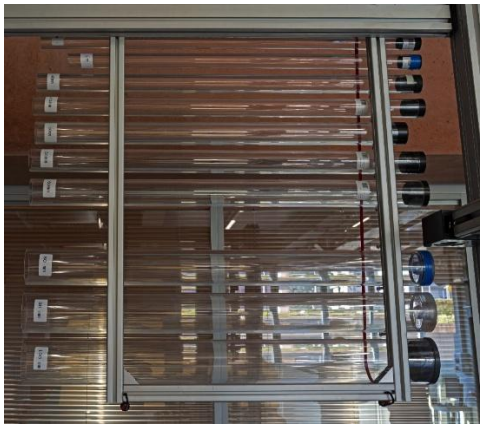

Figure 5.8: Tubes for air cannon

Figure 5.9: Hail resistance test

Analysing in detail the process from the beginning, the first step is the preparation of the iceballs; for this purpose, different moulds of various diameters are required. These

metal moulds are used to cast the iceballs from ice cubes (made of optically clear ice, denser than standard ice). Once the ice balls are made, they must be stored in a freezer at -4°C (IEC 61215) for a time between 1h and 48h or -20°C for a time of at least 48h (VKF); usually in this last case it's suggested to not exceed 4/5 days of storage unless the iceballs will start losing the ideal shape. After the storage period, the ice balls are ready to be shot on the module, targeting 11 or 16 specific positions at speed/kinetic energy according to the normative and depending on the chosen ice ball diameter. The first 11 shots locations are the same for both standards, while the last 5 shots are performed only following the VKF standard normative.

Shot No.	**Location of the impact points**
Pos.	Description
1	Any corner of the module window, not more than one radius of ice-ball from the module edge
2	Any edge of the module, not more than one radius of ice-ball from the module edge
3, 4	Over the circuit near interconnects (i.e. cell interconnects and bus ribbons)
5, 6	Over edges of the circuit (e.g. individual cells)
7,8	On the module window, not more than half diameter of ice ball from one of the points at which the module is mounted to the supporting structure
9,10	On the module window, at points farthest from the points selected above
11	Any point which may prove especially vulnerable to hail impact like over the junction box
12÷16	Other possible weak points, framing and mounting structure

Table 5.2: Impact location according to VKF

Both IEC and VKF consider an impact velocity of a hailstone following the hypothesis of a free-falling sphere with fixed parameters such as ice and air density, drag coefficient ecc. According to the literature, the terminal velocity is calculated as:

$$V_t = \sqrt{\frac{4\delta_{hail} D_{hail} g}{3\rho_{air} C_d}}$$

where δ is the ice density [kg/m^3], g is the acceleration of gravity [m/s^2], ρ_{air} the air density [kg/m^3] and C_d the drag coefficient [-], estimated as 0,5 in the literature. To be considered valid, each shot must follow certain requirements regarding ice ball mass, diameter and impact velocity (IEC 61215) or just kinetic energy (VKF) with proper tolerances. Shots with velocity/kinetic energy higher than the ones according to the normative can be considered valid if the tested module is not damaged. When the shot has a lower kinetic energy/velocity than requested, it cannot be considered valid, so the shot must be repeated. According to VKF, the test must be conducted at an ambient temperature of 20°C ± 2°C and RH 50% ± 20%. The cannon is formed by a tube (selected with the right diameter depending on the ice ball diameter) attached to an air pressurizer and mounted on a movable arm. The air pressure is adjusted depending

on the diameter and the mass of the ice ball. The module passes the test if after all 16 valid shots, the glass is not broken and the cells are not badly damaged. The measurement equipment is mostly composed by an ice ball velocity sensor, a balance for the mass and a calliper for the diameter. The kinetic energy is calculated from the measured parameters. Each shot parameter must be recorded and included in the final report.

min	**DIAM**	max	min	**MASS**	max	min	**VEL**	Max	min	**ENE**	max
[mm]			[g]			[m/s]			[J]		
23.75	**25**	26.25	7.15	**7.53**	7.91	21.85	**23.0**	24.15	1.78	**2.0**	2.31
33.25	**35**	36.75	19.67	**20.7**	21.74	25.84	**27.2**	28.56	6.57	**7.7**	8.86
42.75	**45**	47.25	41.71	**43.9**	46.10	29.17	**30.7**	32.24	17.74	**20.7**	23.95
52.25	**55**	57.75	76.19	**80.2**	84.21	32.21	**33.9**	35.60	39.51	**46.1**	53.35
61.75	**65**	68.25	125	**132.0**	139	34.87	**36.7**	38.54	76.22	**88.9**	102.91
71.25	**75**	78.75	193	**203.0**	213	37.53	**39.5**	41.48	136	**158**	183

Table 5.3: Requirements and tolerances for some iceball diameters according to IEC 61215

Class	**Nominal Diameter**	**G_{min} Minimum Mass**	**G_{max} Maximale Mass**	**v_R Reference Speed**	**Min. Energy Class Level E_{min}**	**Max. Energy Class Lvel E_{max}**
	[mm]	[g]	[g]	[m/s]	[J]	[J]
HW 1	10	0.43	0.51	13.77	**≥ 0.04**	**≤ 0.09**
HW 2	20	3.46	4.04	19.48	**≥ 0.69**	**≤ 1.0**
HW 3	30	11.68	13.65	23.85	**≥ 3.5**	**≤ 4.4**
HW 4	40	27.70	32.35	27.54	**≥ 11.1**	**≤ 13.2**
HW 5	50	54.09	63.18	30.79	**≥ 27.0**	**≤ 31.5**

Table 5.4: Requirements and tolerances for some diameters according to VKF

6 Experiment

The experiment is mostly focused on studying the consequences of hail impact on a PV module in different pre-aging conditions and with different angles of incidence. while monitoring damages on the cells and measuring the power losses. The purpose is to mimic the different working conditions on the field (different tilt angles and aging) and investigating the hypothetical possibility of reducing damages on a module adjusting the tilt angle using an actuator, especially in case of modules with trackers, as suggested in [46]

Briefly, angles of incidence of 90°, 60° and 45° and pre-aging conditions such as accelerated aging due to "*Damp Heat Test*" or mechanically stressed due to "*Mechanical Load Test*" have been selected for the hail resistance testing.

For this purpose, multiple modules of the same model are needed. From all the different models of module available in PVLab's storage, a module made by ARRES (model Arres 3.0 Premium L 420) has been selected for this set of experiments. This is a 420W_P glass/backsheet framed module equipped with a 4mm tempered front glass. Cells for this type of module are monocrystalline TOPCON n-type half-cut. This module is classified as HW5 class for hail (i.e. it's certified as able to withstand ice balls up to 50mm diameter without glass breakage or major damages on the cells). Datasheet for this type of module is attached to the appendix.

6.1. Design of experiment

For this experiment, nine modules of the previously mentioned model have been selected; in particular, five of them are new modules (i.e. they didn't go through pre-aging mechanism), two of them have been previously aged through "*Damp Heat*" and the remaining two went through mechanical stress due to "*Mechanical Load*". More precise descriptions of these tests and the equipment needed are presented in the following chapters.

These nine modules are divided into:

- One "*Reference Module*": this module is selected between the new modules and doesn't go through hail resistance testing; precisely, this module is selected as reference and it's selected as the module with average electrical performance and without major defects on the cells.

- One "*Demo Module*": this is a new module tested for hail with an angle of incidence of 90°; in addiction to that, this module is the first one to be tested and it has been useful to finalize the starting hypothesis regarding the testing procedure and the adequacy of the parameters selected for the "Hail Resistance Test", and to calibrate the equipment.
- One "*90° New Module*": this is one of the new modules and it's tested for hail with an angle of incidence 90°.
- One "*60° New Module*": this is one of the new modules and it's tested for hail with an angle of incidence 60°.
- One "*45° New Module*": this is one of the new modules and it's tested for hail with an angle of incidence 45°.
- Two "*DAH Module n*": these two modules are the ones pre-aged through a "*Damp Heat*" accelerated aging and are tested for hail with an angle of incidence of 90°. Both went through 200h of DAH.
- Two "*MEL Module n*": these two modules are the ones pre-aged through a "*Mechanical Load*" stress and are tested for hail with an angle of incidence of 90°. The two modules went through different MEL cycles; the first one had to withstand positive pressure up to 15000 Pa, while the second one up to 5400 Pa negative pressure.

As previously mentioned, the main goal of this experiment is to monitor and try to evaluate the impact of hailstones on a PV module in terms of electrical/power losses and damages on the cells. To do so, multiple power measurements and electroluminescence pictures are required. Starting from this assumption, the tests performed on each module is divided in three steps:

- **Pre-Characterization**: in this first step the module is inspected visually (performing a "*Visual inspection*", "*Photoluminescence*" and "*Electroluminescence*") and then electrically measured ("*Power measurement at STC*"). The prementioned tests are useful to have a "picture" of the initial condition of the modules before hail testing cycle. During this phase is also chosen the "*Reference Module*"
- **Hail Resistance Testing**: during this step each module (except the reference one) went through a cycle of "*Hail Resistance Test*", power measurement ("*Power measurement at STC*") and "*Electroluminescence Test*". The procedure for the HAR is designed as a non-standard procedure consisting of six or seven shots each, which will be described in detail in the following chapters. This step will continue until the front glass is broken by an iceball impact.
- **Final Measurements**: once the front glass is broken, a final step consisting of an inspection (visually and through EL imaging) and a power measurement is performed.

Module Name	Reference Module	Demo Module	90° New Module	60° New Module	45° New Module
Angle of Incidence [°]	\	90°	90°	60°	45°
Pre-Aging Condition	New	New	New	New	New
Label	23/P09-C5	23/P09-C4	23/P09-C6	23/P09-C7	23/P09-C9
Pre-Characterization	VI (+PL)	VI (+PL)	VI (+PL)	VI (+PL)	VI (+PL)
	EL	EL	EL	EL	EL
	PM_STC	PM_STC	PM_STC	PM_STC	PM_STC
Hail Resistance Testing (until glass breakage)		HAR (r1)	HAR (r1)	HAR (r1)	HAR (r1)
		EL (r1)	EL (r1)	EL (r1)	EL (r1)
			PM_STC (r1)	PM_STC (r1)	PM_STC (r1)
		HAR (r2)	HAR (r2)	HAR (r2)	HAR (r2)
		EL (r2)	EL (r2)	EL (r2)	EL (r2)
			PM_STC (r2)	PM_STC (r2)	PM_STC (r2)
		...	....	....	....
		HAR (rx)	HAR (rx)	HAR (rx)	HAR (rx)
Final Measurements	VI	VI	VI	VI	VI
	EL	EL	EL	EL	EL
	PM_STC		PM_STC	PM_STC	PM_STC

Module Name	DAH Module 1	MEL Module 1	MEL Module 2	DAH Module 2
Angle of Incidence [°]	90°	90°	90°	90°
Pre-Aging Condition	DAH	MEL	MEL	DAH
Label	23/P09-C2	23/P09-C10	23/P09-C11	23/P09-C1
Pre-Characterization	VI (+PL)	VI (+PL)	VI (+PL)	VI (+PL)
	EL	EL	EL	EL
	PM_STC	PM_STC	PM_STC	PM_STC
Hail Resistance Testing (until glass breakage)	HAR (r1)	HAR (r1)	HAR (r1)	HAR (r1)
	EL (r1)	EL (r1)	EL (r1)	EL (r1)
	PM_STC (r1)	PM_STC (r1)	PM_STC (r1)	PM_STC (r1)
	HAR (r2)	HAR (r2)	HAR (r2)	HAR (r2)
	EL (r2)	EL (r2)	EL (r2)	EL (r2)
	PM_STC (r2)	PM_STC (r2)	PM_STC (r2)	PM_STC (r2)
	....	....	....	....
	HAR (rx)	HAR (rx)	HAR (rx)	HAR (rx)
Final Measurements	VI	VI	VI	VI
	EL	EL	EL	EL
	PM_STC	PM_STC	PM_STC	PM_STC

Table 6.1: Summary of the modules and design of experiment

6.2. Specification about the "*Hail Resistance Test*" cycle

Once designed the experiment, the parameters and target points for the hail test must be defined. From previous tests on similar modules (in terms of maximum power, technology of the cells, glass tempering and thickness) emerged a glass breaking point kinetic energy close to the one for around 65mm diameter iceball. Considering part of the purpose of this experiment is creating and monitoring cracks during the process of hail testing, it's been decided to shoot 50mm iceballs on the module (the module is HW5 class). As previously mentioned, during the hail testing cycle, each HAR test is designed to be a non-standard test; form this point, each of the HAR tests and related EL and PM_STC will be referred as "run". For each run, an amount of six shots is

performed: the first five of them on undamaged cells (one on the middle, two on the edges and two on the corners respectively) while the sixth one hitting a weak spot or cell, usually directly on cells with dark zones, caused by low temperature during the soldering phase of the module, or pre-existent cell defects. During third and fourth run also a seventh point close to junction boxes is targeted. For simplicity, before choosing the target points, the module is ideally divided in four equal parts (upper/lower and right/left); the first four runs target only cells in one of these parts, while the fifth one targets points on the remaining non-impacted cells (when possible). In addition to that, targets too close to the module's frame are avoided (where the front glass is more fragile to projectile impacts).

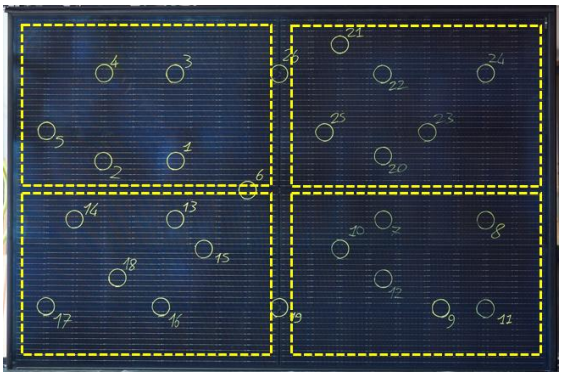

Figure 6.1: Example of target locations

Shot Number	Target Positions	Comment
1	Middle of a cell	
2	Cell Edge (Vertical)	
3	Cell Edge (Horizontal)	
4	Corner between cells	
5	Corner between cells	
6	Weakest point of the module	*TbD for each module
7	Junction box position	*HAR (r3) and HAR (r4)

Table 6.2: Target location's choice criteria

The impact velocity for the first run it's planned to start with the VKF standard for 50mm ice ball (30,79 m/s), then increasing it of a +25% for each subsequent run.

	Diameter [mm]	Velocity ref. [m/s]	Ek ref. [J]	Amount of shots	Eq. Iceball Diameter [mm]	Comments
HAR (r1)	50	30,79	27,00	6	*50,00*	**Standard VKF*
HAR (r2)	50	38,49	42,18	6	*55,90*	
HAR (r3)	50	46,19	60,75	7	*61,24*	
HAR (r4)	50	53,89	82,68	7	*66,14*	
HAR (r5)	50	61,59	107,99	6	*70,71*	
HAR (rx)	50	**=Vhar1*(1+0,25*(x-1))**				

Table 6.3: Impact velocity, kinetic energy and equivalent diameter per HAR run

After every successful HAR test, PM_STC and EL tests are performed to monitor the evolution of the performance of the module and the cells' conditions after multiple iceballs impact. The HAR cycle stops once the front glass is broken and following the last power measurement and EL picture are taken. The next plot presented shows the nominal kinetic energy of the iceballs shot during the n runs of HAR. The red line represents the equation used for the calculation of the kinetic energy in function of the diameter of the iceball, according to VKF standard, while the points on the axis have coordinate y equal to the nominal kinetic energy of the run and x equal to the equivalent iceball diameter, defined as the diameter of the hypothetical iceball having

the same kinetic energy (calculated according to VKF) as the nominal one of the correspondent HAR run. This because, as previously stated, in this experiment the HAR tests are non-standard test where the iceball diameter is maintained constant for each run, while the velocity is upscaled by a factor run by run.

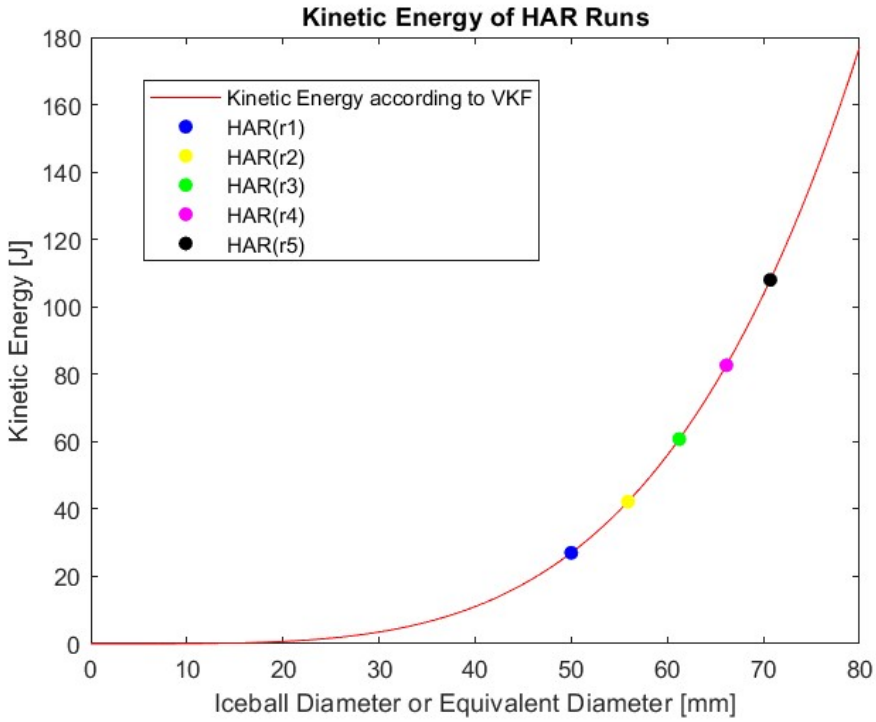

Figure 6.2: KE in function of diameter and equivalent diameter per HAR run

6.3. Pre-characterization and choice of reference module

The first task is the choice of the reference module; once all the tests (VI, PL, EL and PM_STC) are performed, a comparison between the new modules is done. The chosen module is the one with an average Pmax and without major defects recognizable from the EL picture. From the power measurements emerged an average Pmax of 397.26 W. Considered both the Pmax and the EL pictures of the modules, the chosen reference module is the one labeled as “23-P09/C5”.

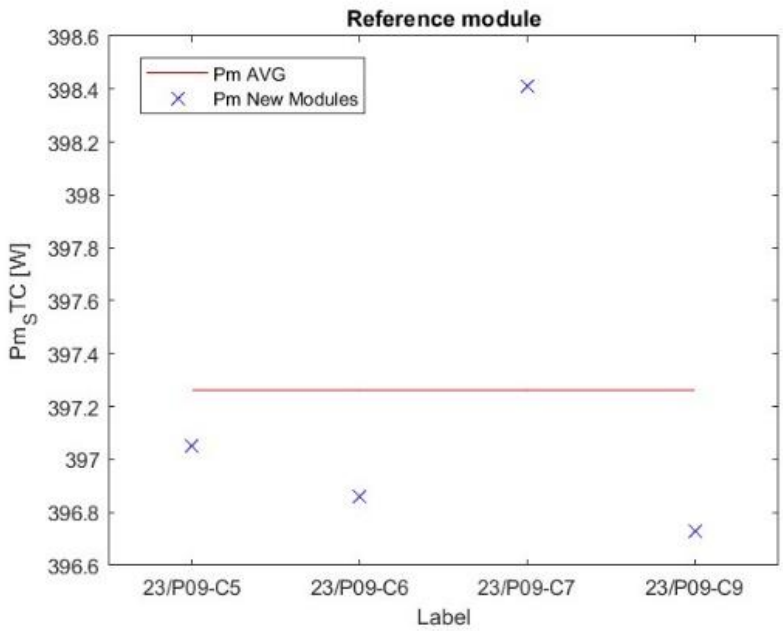

Figure 6.3: P_{max} new modules

From the EL pictures of the modules, multiples initial cell defects can be recognized; most of them can be correlated to the manufacture of the cells or modules, especially because of thermal stress during the soldering phase (that leads to chips on the vertical edge of the cells, close to the fingers) or because of cold soldering (leading to darker areas of the cells in the EL). Other frequent type of defects is the presence of chips on horizontal edges of the cells on the top part of the module. All the types of cell defects found on the cells before the HAR cycle are described more in detail in the chapter regarding the Crack Analysis. On average, the Pmax of pre-age module is slightly lower than the new ones.

	Label	DAH (y/n)	MEL (y/n)	Pm_pre [W]	FF_pre [%]
REF.	23/P09-C5	n	n	397,05	80,05
DEMO	23/P09-C4	n	n	394,45	79,61
	23/P09-C6	n	n	396,86	79,85
	23/P09-C7	n	n	398,41	80,37
	23/P09-C9	n	n	396,73	79,78
DAH 1	23/P09-C2	y	n	393,12	79,48
MEL 1	23/P09-C10	n	y	391	78,99
MEL 2	23/P09-C11	n	y	395,35	79,71
DAH 2	23/P09-C1	y	n	389,05	78,60

Table 6.4: P_{max} and FF per module

7 Results

7.1. Mechanical impact on front glass

In this chapter, mechanical impact of iceballs on the front glass will be analyzed. Figure x shows the points correspondent to the highest kinetic energy of an iceball shot on the modules and the equivalent diameter of the iceball. Data collected show that 90° modules' (both new and pre-aged modules) front glass breaks when impacted by an iceball's kinetic energy around 60/80 J (typical values for third and fourth run of HAR test), consequence of an impact velocity around 45/55 m/s. The data distributes inside a range. The modules impacted at 60° and 45° had the glass broken for higher impact energy, close to 105/110 J (during the fifth run of HAR test). This confirms the initial hypothesis that impacts having incidence angle of 90° makes the mechanical impact of iceballs on the module more severe, while for incidence angle of 60° and 45° part of the kinetic energy of the projectile is lost because of fragmentation of the iceball and ice shards deflection. Figure 5.2 shows the data collected from the tests on new modules (90°, 60° and 45°) and the tendency line (second grade polynomial fit) in terms of maximum kinetic energy impacted on the module in function of the angle of incidence. The polynomial fit is expected to reproduce a sinusoidal function in some way; in this experiment the maximum is between 60° and 45° degrees because of low data collected for new modules, especially when the incidence angle is non 90°.

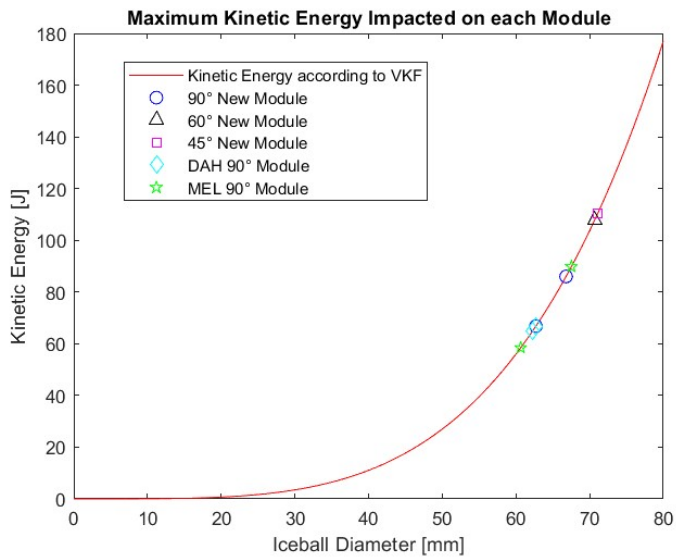

Figure 7.1: Measured maximum kinetic energy withstood by modules

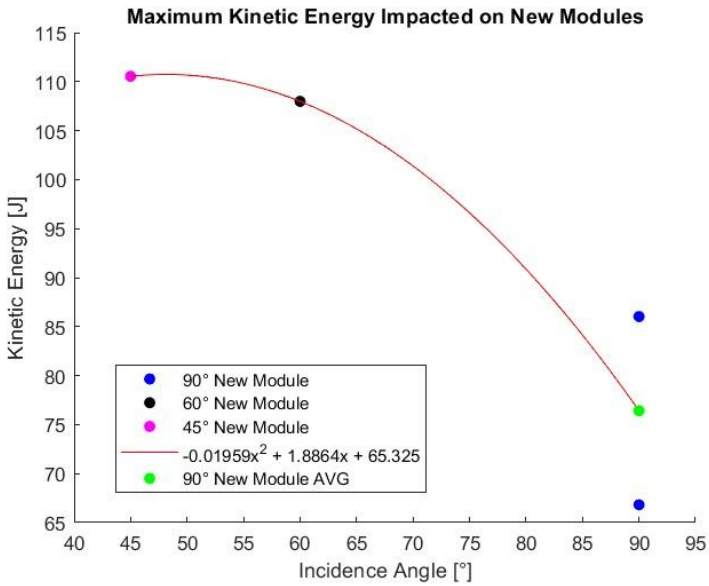

Figure 7.2: Comparison between module with different incidence angle

MODULE	Nominal Iceball Velocity [m/s]	Max Kinetic Energy [J]	Equivalent Diameter [mm]	Last HAR run
REFERENCE	/	/	/	/
DEMO	46,19	66,82	62,71	3
90° NEW	53,89	86,02	66,80	4
60° NEW	61,59	107,98	70,71	5
45° NEW	61,59	110,54	71,12	5
DAH 1	46,19	66,79	62,71	3
Hard MEL	46,19	58,43	60,65	3
MEL	53,89	89,82	67,53	4
DAH 2	46,19	64,77	62,23	3

Table 7.1: Glass breakage kinetic energy and HAR run per module (measured)

7.2. Electrical parameters and performance

In this chapter, effects of the iceballs impact on electrical parameters will be discussed. As mentioned in the previous chapters, after every successful HAR run a PM_STC test is performed. This implies that a power measurement is performed after 6 or 7 shots after the previous one, depending on the current run number. In the following plots, "Delta_X(rn)" is the difference between the measurement after the nth run (either successful or unsuccessful) and the one during the pre-characterization phase; when referred to "Delta_P_{max}", "Delta_I_{sc}" or "Delta_V_{oc}", those variables are calculated as following:

$$\text{Delta_X(rn)} = (\text{X_HAR(rn)} - \text{X_Pre})/\text{X_Pre} \qquad [\%]$$

where "X" could be "P_{max}" or "V_{oc}" or "I_{sc}", "rn" indicates the number of HAR run correspondent to that measurement, "X_HAR(rn)" is the measurement after the nth

HAR run (either successful or unsuccessful), "X_Pre" is the measurement made during the pre-characterization phase.

Figure x summarizes the maximum power loss in percentage between the pre-characterization and the measurement made after the last successful HAR run, i.e. the last one before the glass is broken, for all the modules considered in the experiment. Results shows that in no case the damage induced to the modules and to the cells leads to a power loss higher than 2% (around 7W). Later in this chapter, data will be analysed more in detail, comparing modules and EL to correlate the power losses to cell damages. "Demo module" is not included in this analysis, because there are no measurements done during the HAR testing phase. Figure x shows Delta_P_{max} calculated after each run for each module; as expected, P_{max} decreases after almost every HAR run. It's important to remember that the measured data have an uncertainty, so it's possible to have measured data of P_{max} higher than the previous measurement for the same module.

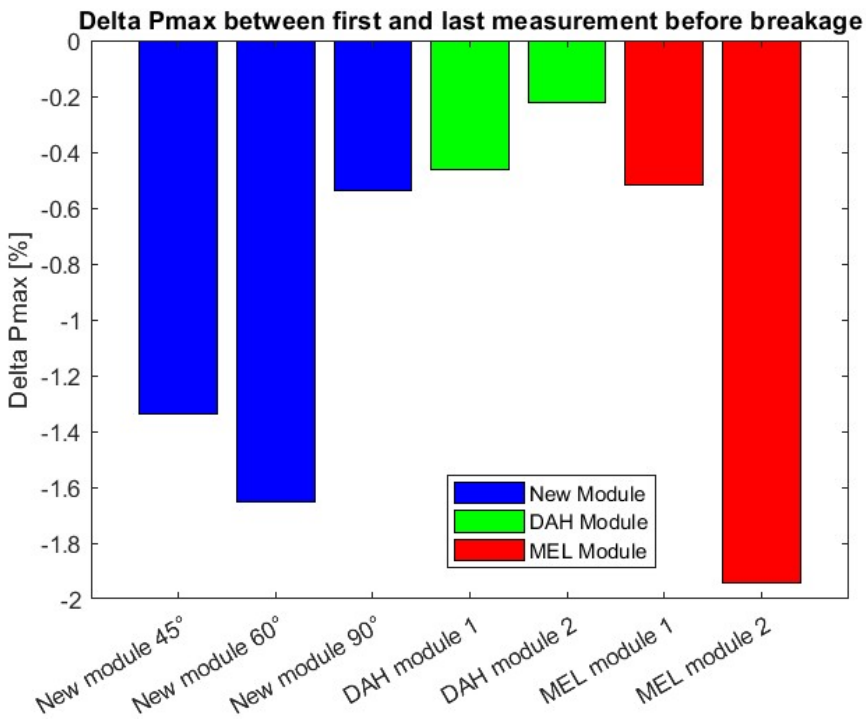

Figure 7.3: Delta_P_{max} per module

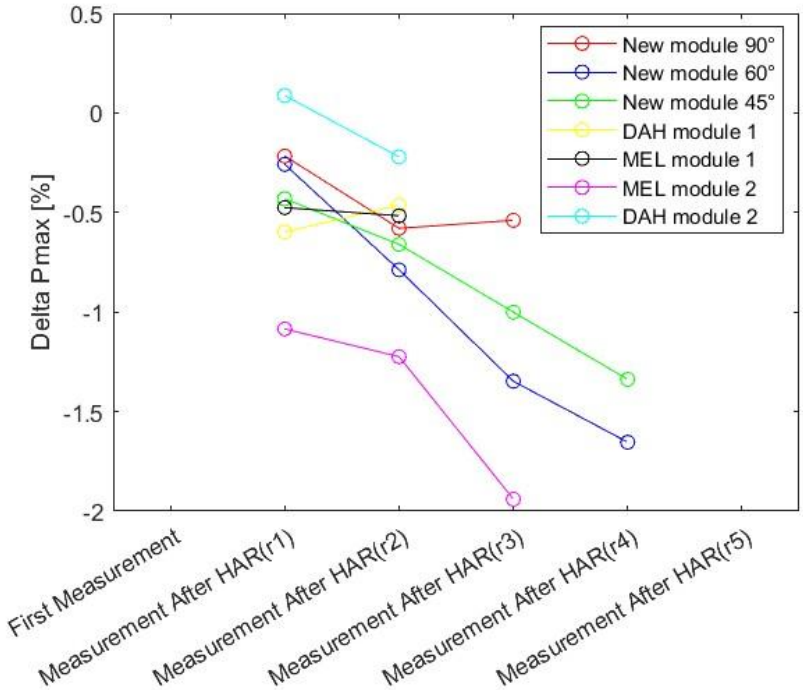

Figure 7.4: Evolution of Delta_P_{max} during HAR cycle

The first relevant comparison is between the new modules with different angles (90°, 60° and 45°). As shown in Figure 5.5, the first thing to notice is the major difference in Delta_P_{max} between the "*90° New Module*" and both "*60° New Module*" and "*45° New Module*"; for the first one is around -0,5% while for the other two modules Pmax drops of around 1,2%-1,4%. This happened mostly for a couple of reasons: the initial condition of the modules (60° and 45° modules have a higher number of pre-existent defects) and the different number of runs (so a higher number of generated cracks) they have been through during the HAR cycle. In particular, last measurements on the modules before glass breakage are after the 3rd HAR run for "*90° New Module*" and after the 4th run for "*60° New Module*" and "*45° New Module*". This means that the "*90° New Module*" has been already impacted with 19 iceballs, while the other two ones have been impacted 26 times; consequently, a pre-existent defect's transition to crack is more likely to occur, and once a new crack is generated, it gets worse after every shot during the HAR cycle (mostly due to the vibrations generated on the module). Comparing the EL pictures before and after the HAR cycle, keeping in mind the last relevant EL picture is the one after the last successful run before the glass breakage, it's possible to notice that newly damaged cells on "*60° New Module*" and "*45° New Module*" also generated dark areas due to damages on electrical connections on those cells, so a loss of active area of those cells. For the same reason, Delta_P_{max} for "*60° New Module*" is higher than the one for "*45° New Module*", in absolute values.

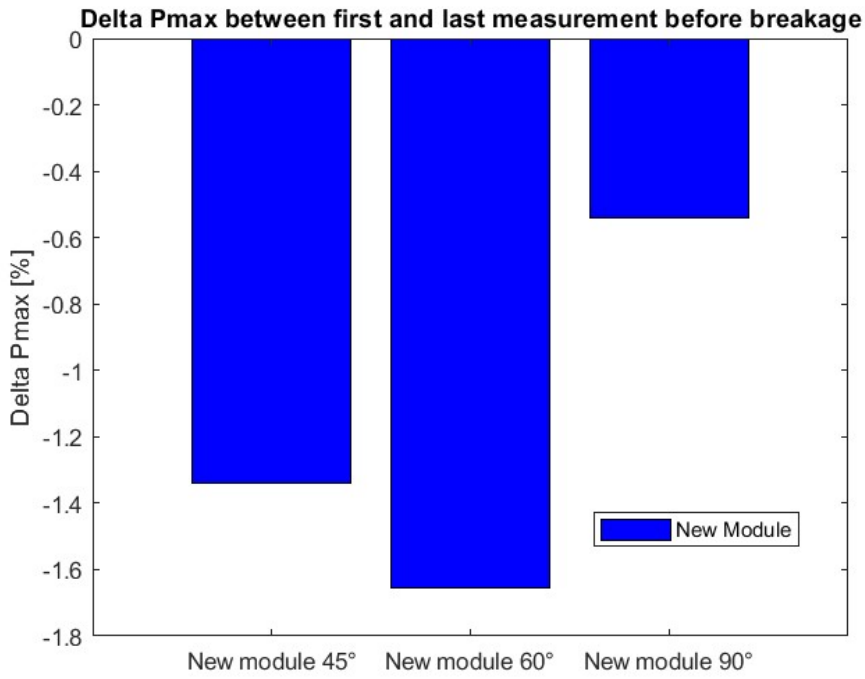

Figure 7.5: Delta_P_{max} per module. Comparison for different angle of incidence

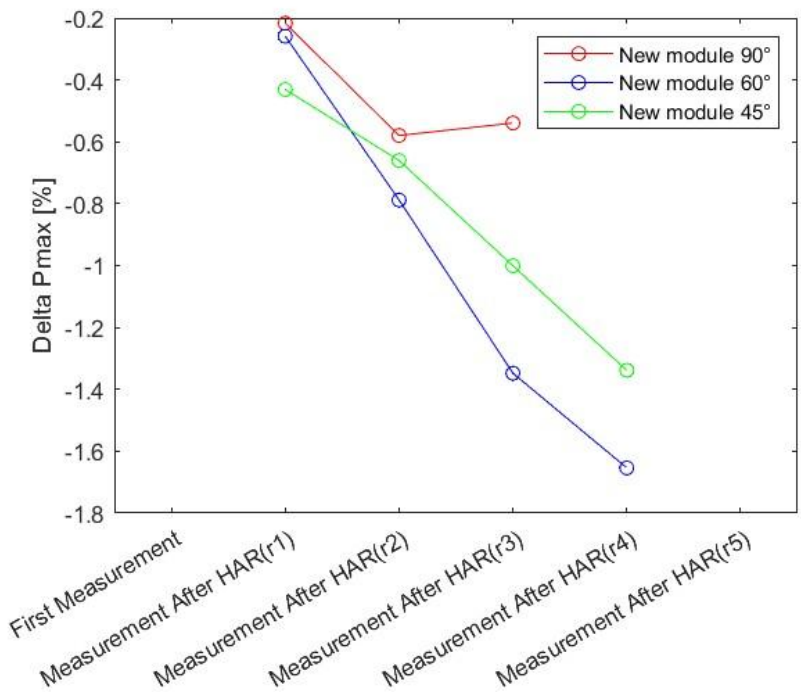

Figure 7.6: Evolution of Delta_P_{max} during HAR cycle. Comparison for different angle of incidence

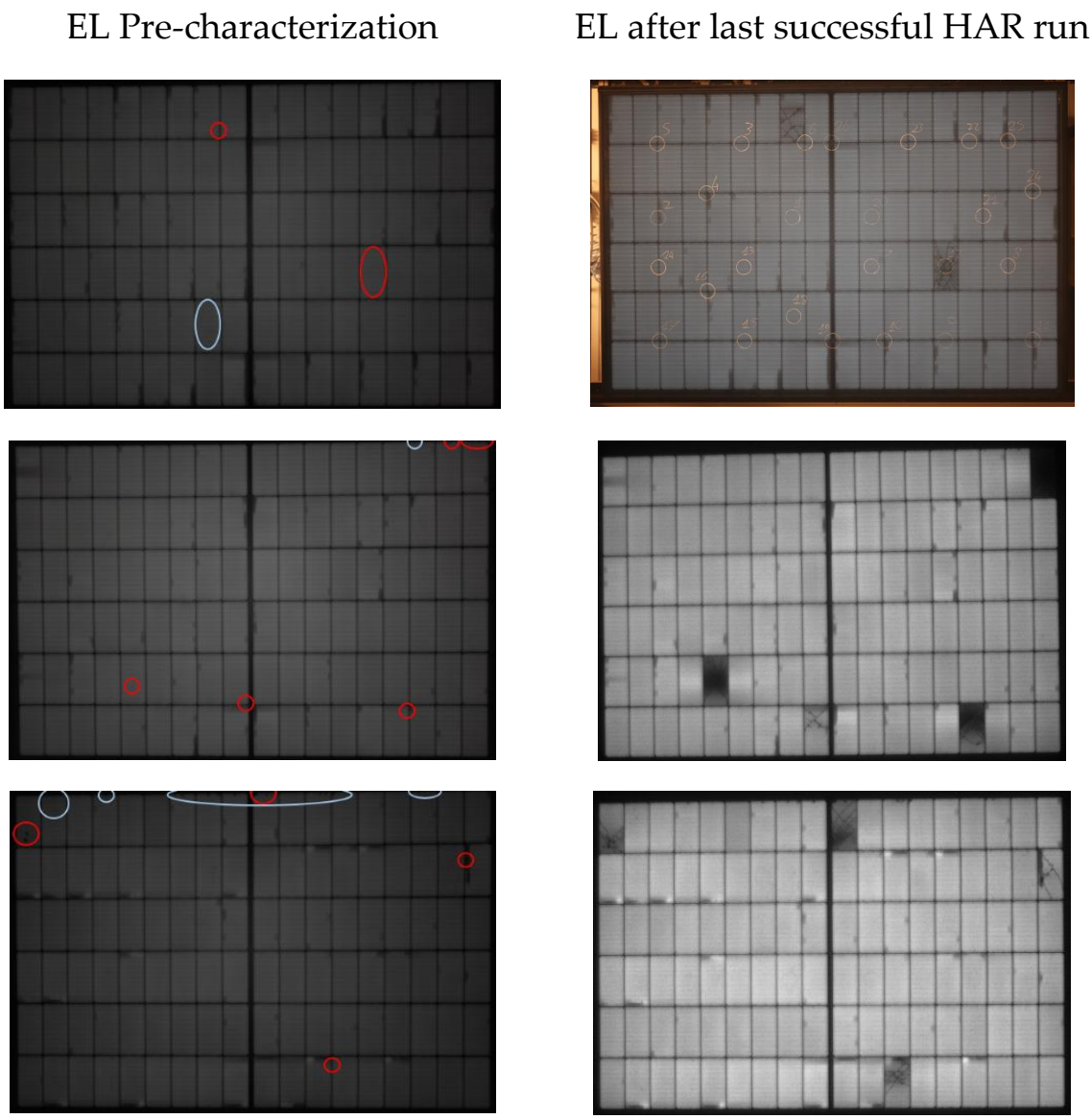

Figure 7.7: Comparison between EL pre-characterization and last measurement before glass breakage. From the top: *90° New Module*", *60° New Module*", *45° New Module*"

Comparing the prestressed modules (the two "*DAH Modules*" and the two "*MEL Modules*") with the "*90° New Module*", and considering Delta_P_{max} it is possible to confirm the previous hypothetical correlation between the number of iceball impacted on the module before the last considered measurement and the power loss; in fact, "*MEL Module 2*" and "*90° New Module*", that are the only ones whose glass survived 3 complete HAR runs. It's also important to highlight that both "*MEL Modules*" have part of the pre-existing defects already developed into cracks because of the MEL process, especially "*MEL Module 1*" because of the harsher "*Mechanical Load*" conditions. This also effects the number of new cracks generated on these modules, in fact "*MEL Module 1*" during the HAR cycle have increased damages on the already

cracked cells instead of generating new ones while "*MEL Module 2*" shows both phenomena at the same time; in this case there are also some cells which showed highly damaged cells and darker areas because of damages on electrical connections, leading to an higher performance decrease. Meanwhile, the two modules aged trough DAH present no or just a few new cracks, but the cells are not so badly damaged to lead to a relevant power loss. In the specific case of "*DAH Module 1*", during the 3rd run of HAR, a previously visually undamaged cell developed a crack and dark zones; despite that, the following bar plot doesn't show a relevant power loss on that module because the glass broke during the same run, so the power measurement considered is the previous one. This particular case will be analysed later in the chapter regarding the crack analysis.

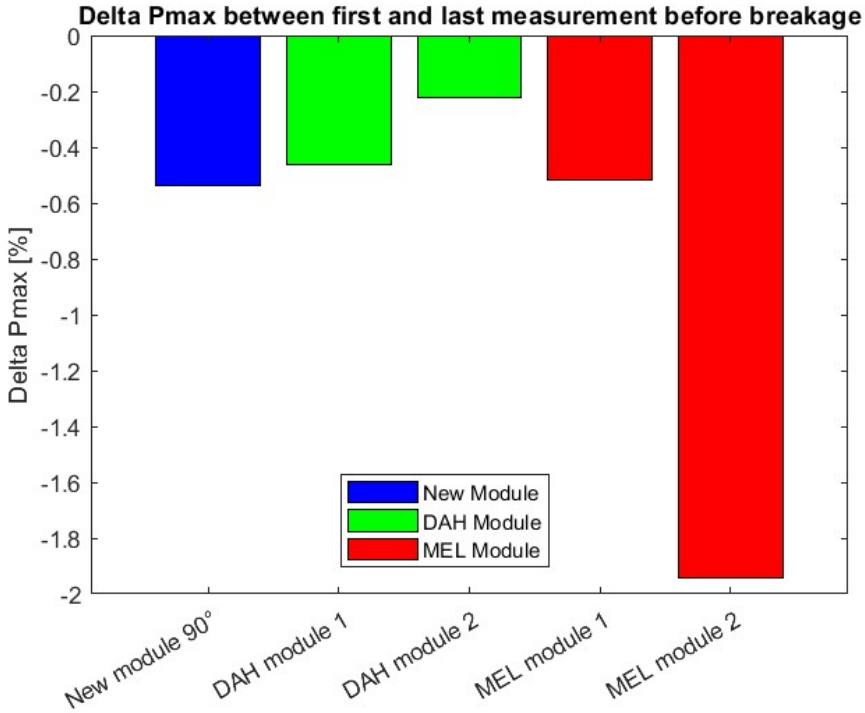

Figure 7.8: Delta_P_{max} per module. Comparison for different aging condition

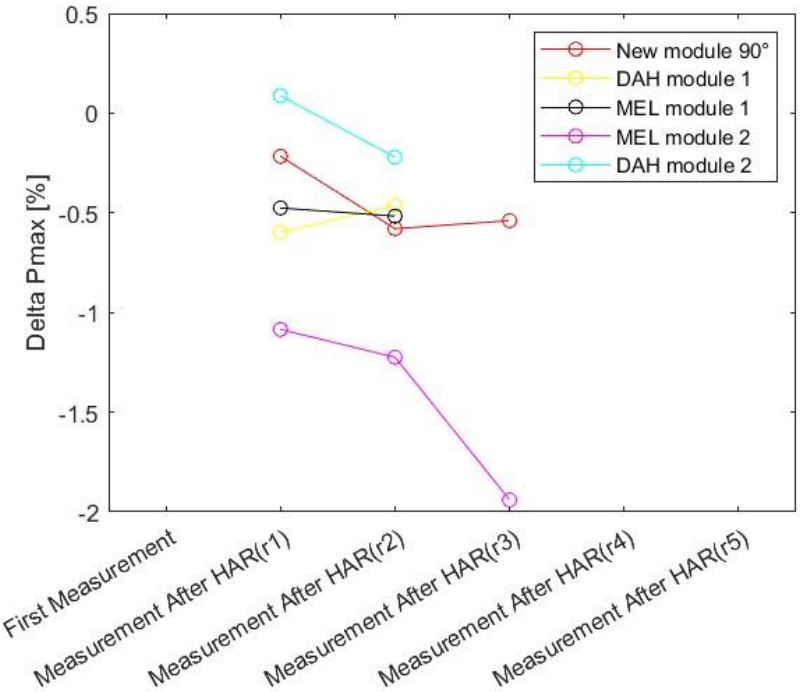

Figure 7.9: Evolution of Delta_P_{max} during HAR cycle. Comparison for different aging condition

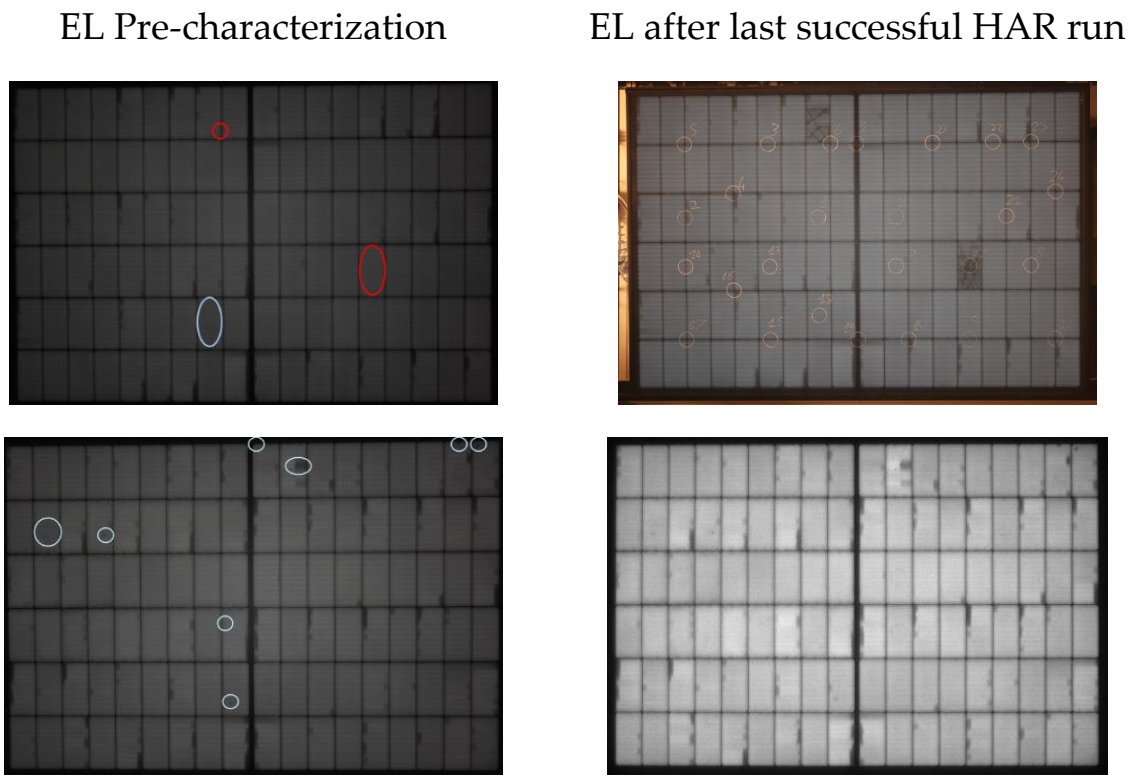

Figure 7.10: Comparison between EL pre-characterization and last measurement before glass breakage. From the top: *90° New Module", "DAH Module 1*

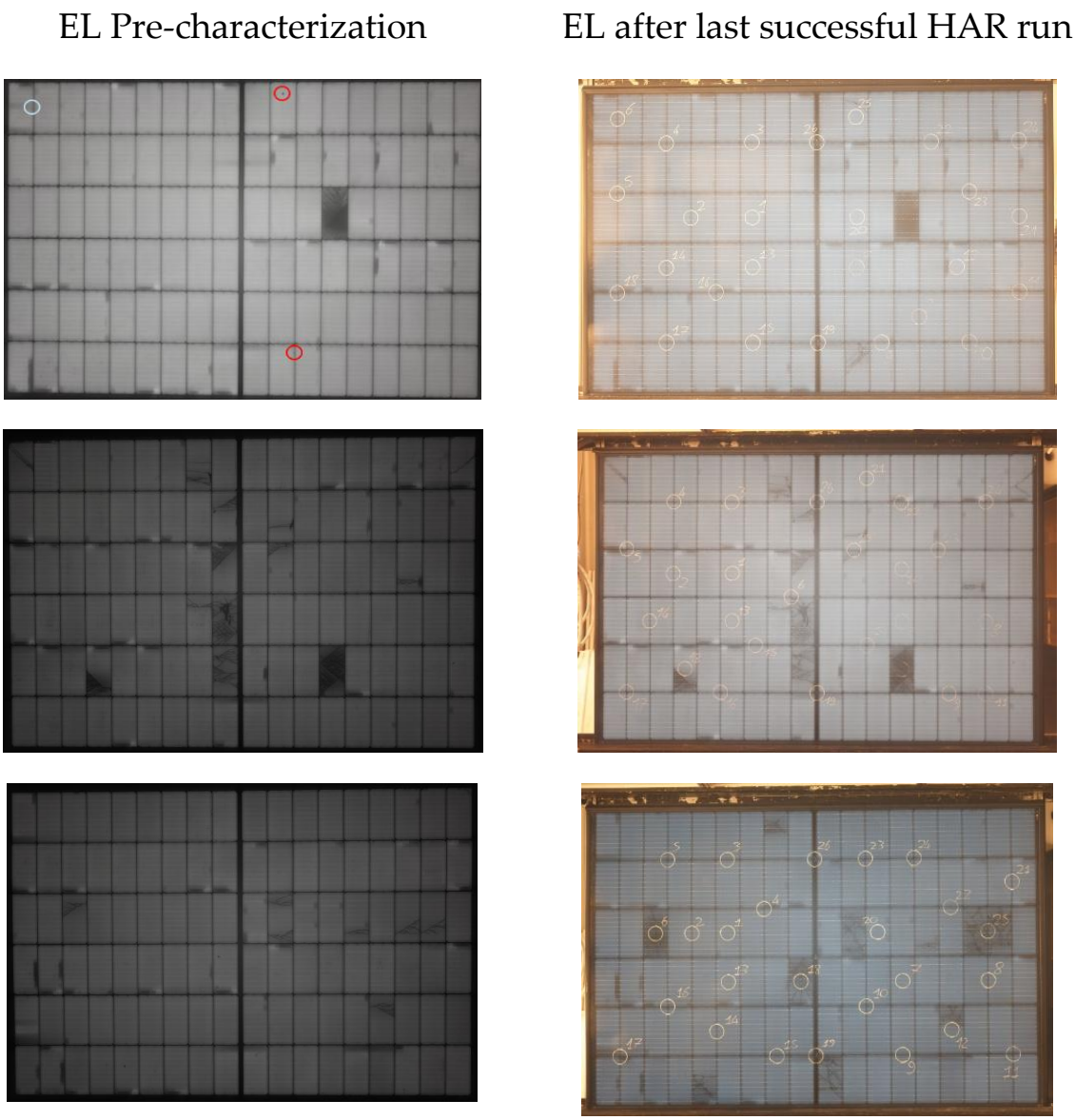

Figure 7.11: Comparison between EL pre-characterization and last measurement before glass breakage. From the top: "*DAH Module 2*", "*MEL Module 1*", "*MEL Module 2*"

Other important parameters to be considered are V_{oc} and I_{sc} and their variation during the HAR cycle. Measurements data shows that the variation of V_{oc} for all the modules it's unpredictable and gets to a maximum of around 0,3%, that's way lower in order of magnitude compared to the variation of I_{sc} and is compatible with the measurement uncertainty. Because of that, the variation of I_{sc} follows the one of P_{max}, with a maximum decrease around -1,6% because of loss of active area of the cells.

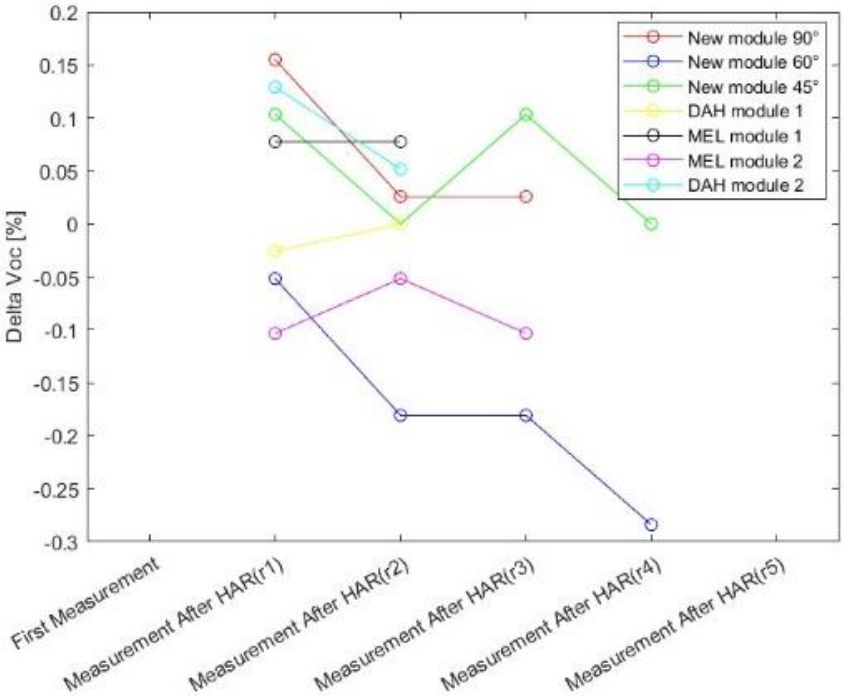

Figure 7.12: Evolution of Delta_V_{oc} during HAR cycle

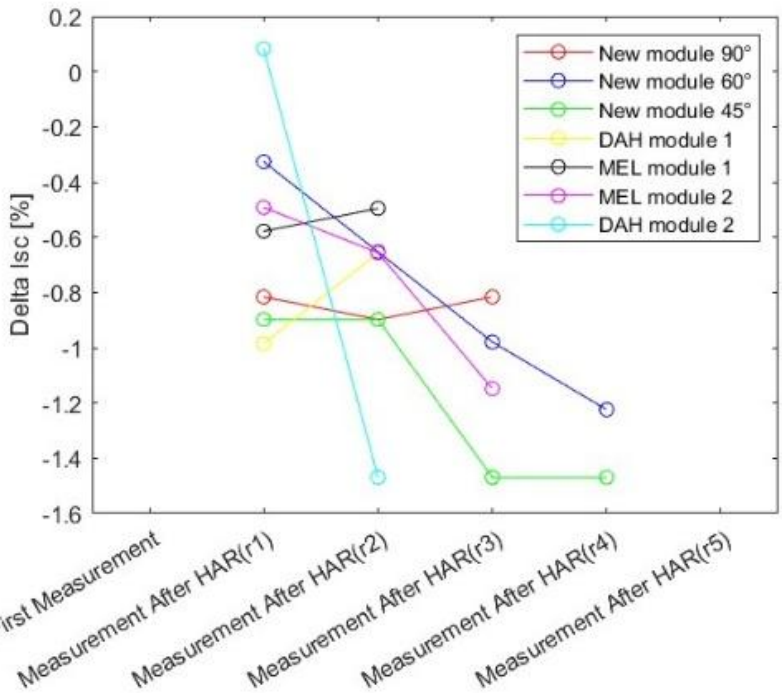

Figure 7.13: Evolution of Delta_I_{sc} during HAR cycle

The following plot shows the difference of P_{max} between the first measurement and the last one after the glass is broken during the HAR cycle; it can be observed an average power loss around 15-30%; this is a consequence of the cells' breakage due to stresses

and vibrations on the module during the glass breakage and because of the variation of optical transmittance of light through the broken glass.

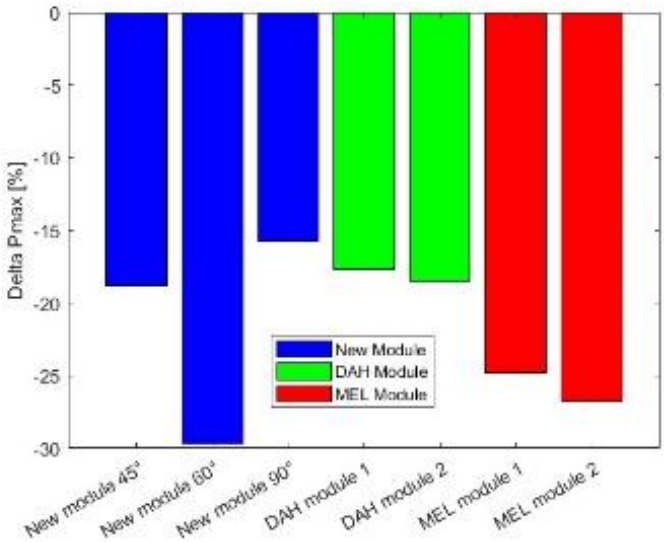

Figure 7.14: Delta_P_{max} per module after glass breakage

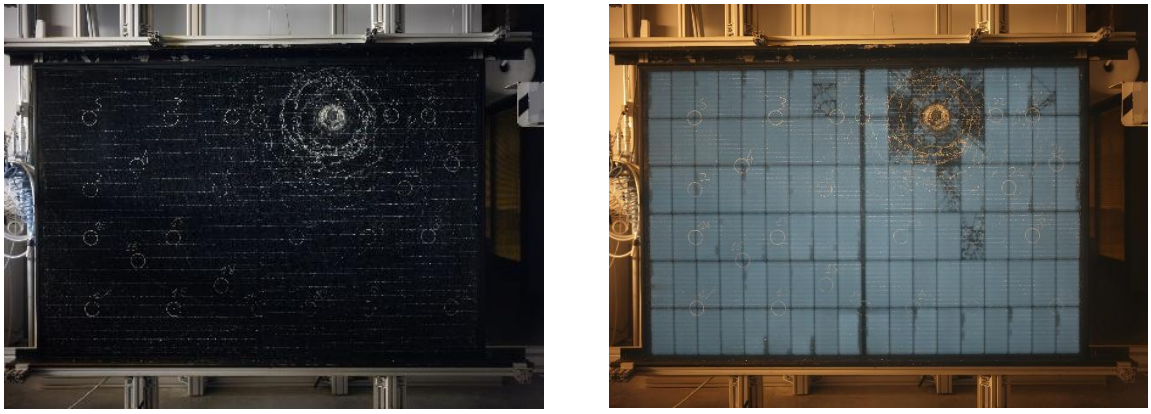

Figure 7.15: VI and EL of a module with broken front glass

7.3. Crack formation and kinetic energy

In this chapter, a brief analysis of the Kinetic Energy correspondent to the shots that generated new crack or broke the modules' front glass is performed. In the following plots, markers are differentiated for shapes and filling; the different shapes represent different angle of incidence or prestress conditions(precisely the circles for 90° angle of incidence new modules, squares for 60° angle of incidence new modules, stars for 45° angle of incidence new modules, triangle for 90° MEL modules and diamond for 90° DAH modules), while the different filling differentiates the shots that generated new cracks, empty marker, with the ones that broke the glass, filled ones. From this plots, two important observations can be deduced; first, the most cracks, especially

considering only the modules impacted perpendicularly, have been generated during the 2nd or 3rd runs of the HAR cycle, except a few cases of direct hits (6th shot) or cells with more severe types of pre-existent defects ,which usually evolved into cracks in the first few impacts, (different types of defects will be discussed in detail in the chapter regarding the crack analysis), either in case of perpendicular impact of the iceball or modules impacted at 60° or 45°; and second, the distribution of cracks generated for tilted modules shows that for non-perpendicular impacts is shifted around higher values of impact kinetic energy. It's important to remember that the difference between the total number of cracks generated on the different modules is highly dependent on the number of pre-existent defects, the severity of those defects and the number of shots impacted on the module.

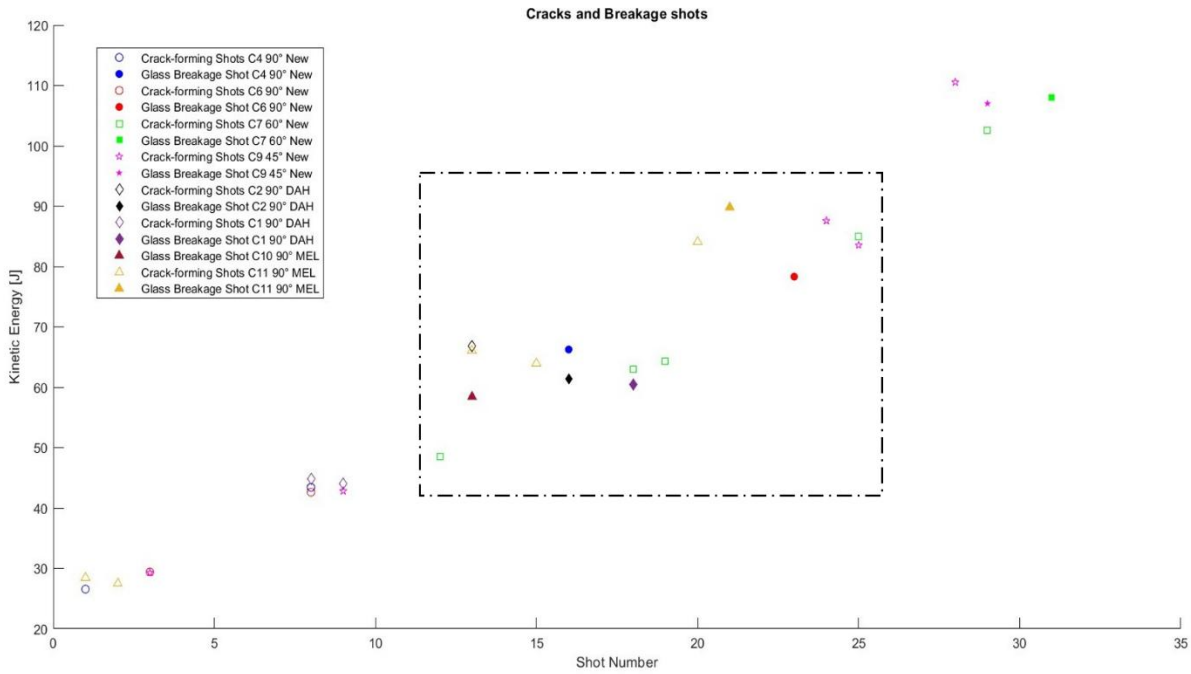

Figure 7.16: Crack-forming, glass breaking shots and kinetic energy. Complete

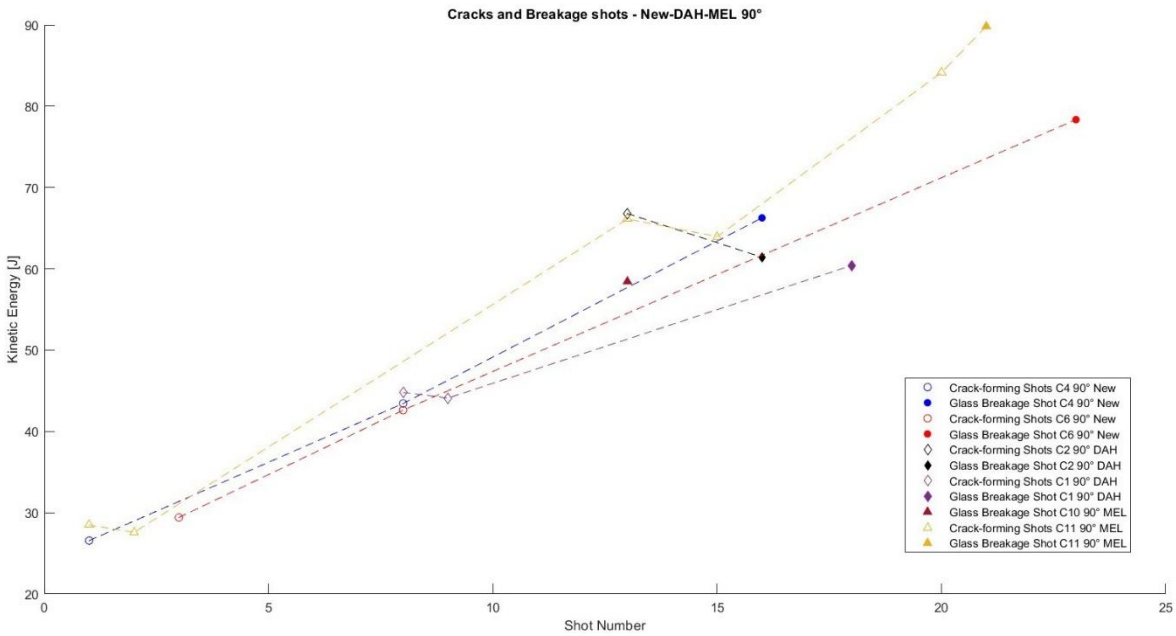

Figure 7.17: Crack-forming, glass breaking shots and kinetic energy. Comparison between different angles of incidence

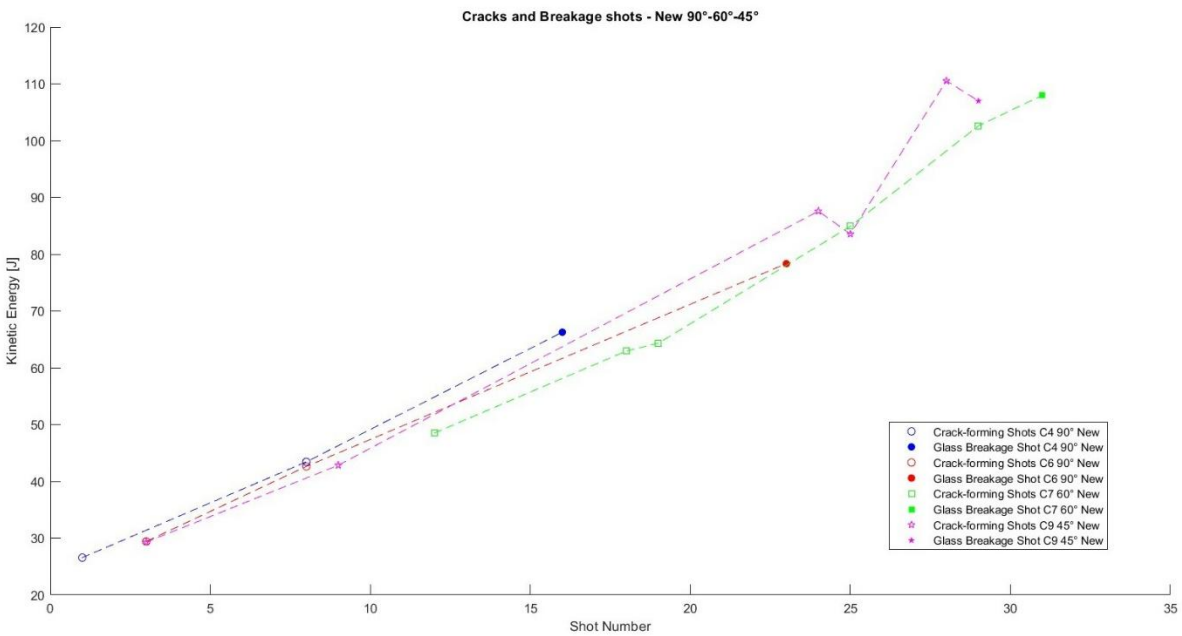

Figure 7.18: Crack-forming and glass breaking shots and kinetic energy. Comparison between different pre-aging conditions

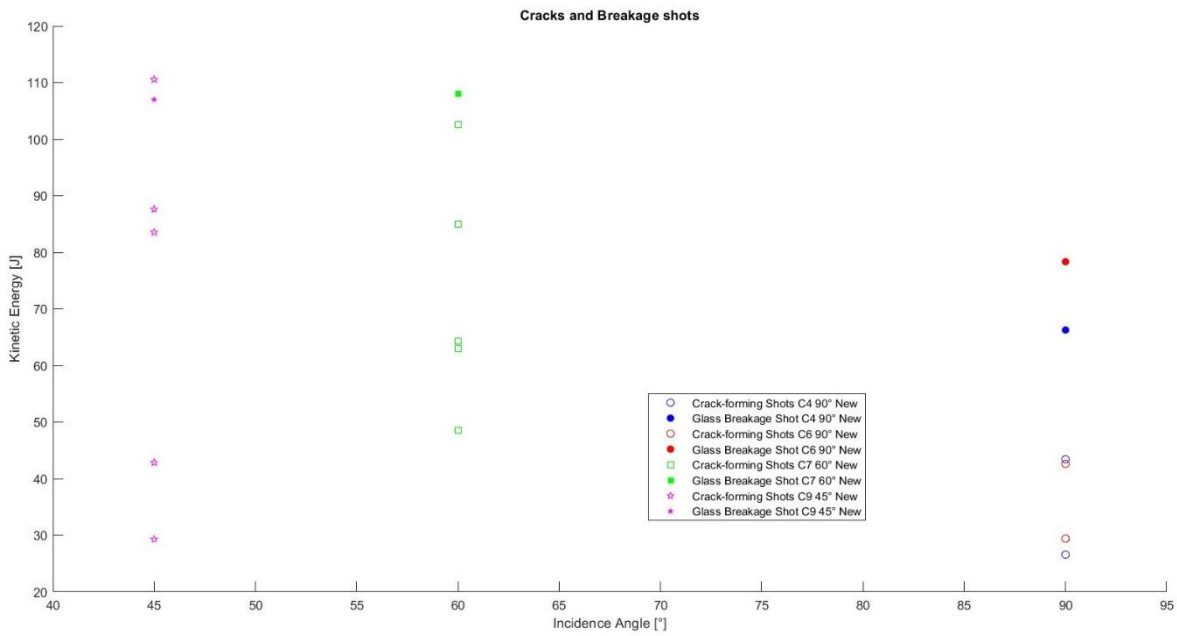

Figure 7.19: Crack-forming, glass breaking shots and angle of incidence.

7.4. Crack Analysis

In this chapter will be analysed the new cracks generated on the cells and their evolution during the HAR cycles. To do so, have been collected EL pictures after each shot to have a complete history of the modules' cells at any time during the experiment. First thing first, a brief introduction on the different types of pre-existent defect and the possible causes will follow. During the experiment, 7 major types of defects have been identified:

- **Dark zones** on the cells: this type of defects is the most found on the modules considered for this experiment; they can be easily detected from the EL pictures. These defects present themselves as darker parts on the edges of the cells, because of a low performance part of the cell. These dark zones are mostly due to low temperature soldering. These types of defects lead just to a loss in the performance of the cells/module, but don't initiate cracks, so in the following analysis they won't be considered.
- **Scratched cells**: this type of defects usually manifests as darker lines like scratches on the cells and are visible through EL pictures. Similarly to dark zones, also this type of defects is consequence of imprecisions during the soldering phase, with consequent contact between the soldering tool and the cell causing these types of lines. Like dark zones, these defects don't initiate cracks.
- **Thermal punctures**: this type of defects manifests as darker spots or points on the cells and are visible through EL pictures. Similarly to scratches, also this

type of defects is consequence of imprecisions during the soldering phase, with consequent contact between the soldering tool and the cell causing these dark points. These defects don't initiate cracks.

- **Chips on vertical edges**: this type of defects manifests in form of little fractures on the side edges of the cells. Those defects can be detected on cells in EL pictures, and they appear as darker lines (compared to scratches) starting on a vertical edge in correspondence of the fingers. These defects are due to excessive thermal stress on the cell during the soldering process.
- **Chips the corner of the cell**: this type of defects manifests in form of little fractures on the corner of a cell. Those defects can be detected on cells in EL pictures, and they appear as darker lines (compared to scratches) starting on corner. This type of defect is similar to chips on vertical edges. In the considered module, this type of defect has been found only once.
- **Chips on horizontal edges**: this type of defects manifests in form of little fractures on the top edge of the cells. Those defects can be detected on cells in EL pictures, and they appear as darker lines (compared to scratches) starting on the top horizontal edge. All the cases detected during the experiment are found on the first row of cells of the modules.
- **Punctures**: this type of defects manifests in form of dark points inside the area of the cells. They are easily recognizable in an EL images as they appear darker than the thermal ones. This type of defect is usually due to poor manufactory or damages during the handling of the module.

In addition to those, modules pre-stressed through MEL present creeps and cracks caused by the mechanical stress previously applied.

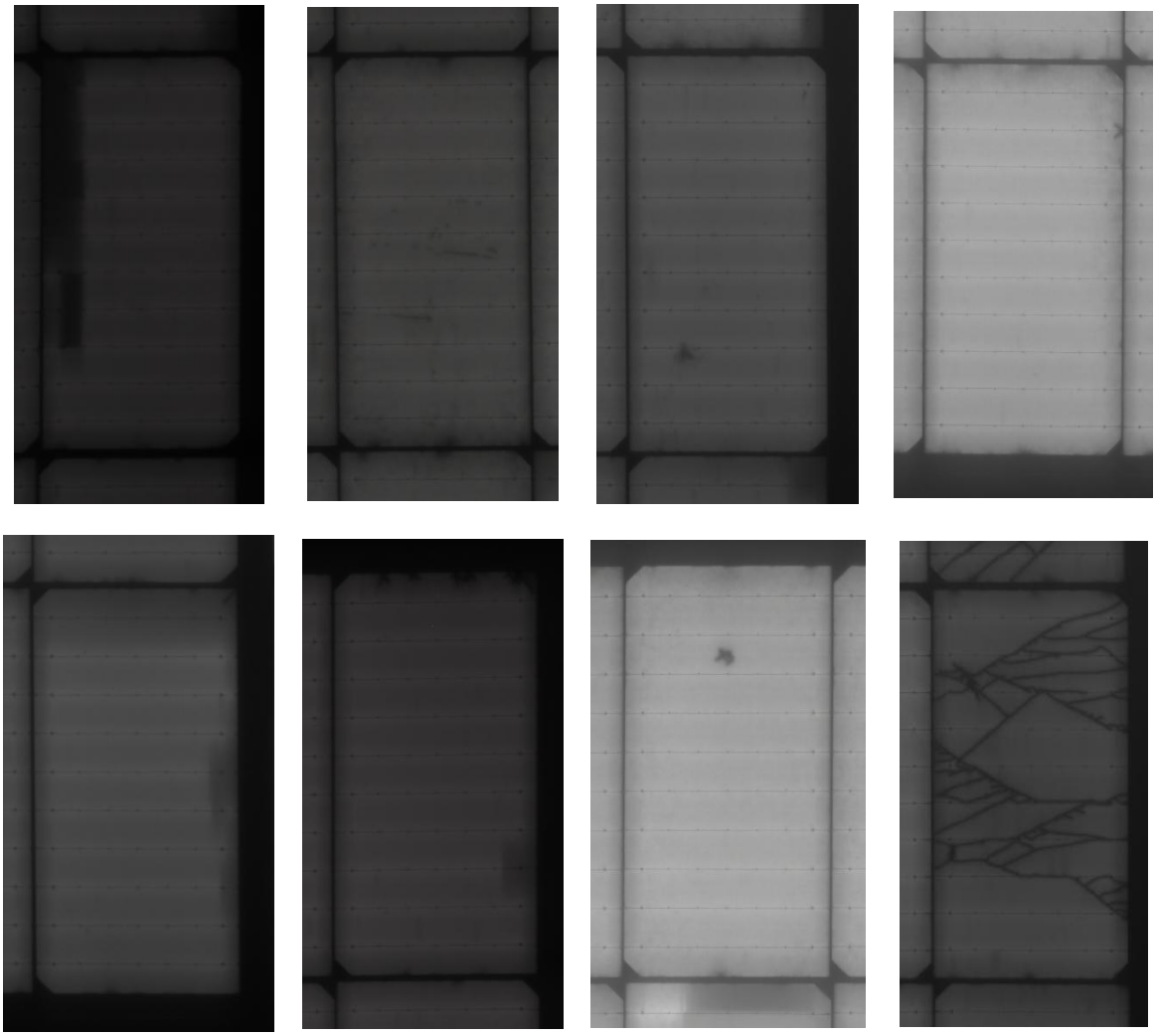

Figure 7.20: examples of types of defects on cells. Top row, from left to right: Dark zone, scratches, thermal puncture, chip on vertical edge. Bottom row, from left to right: chip on the corner, chips on horizontal edge, puncture, cracked cell due to MEL

For the crack analysis, there are a few steps to be followed; first, once collected all the EL picture during the pre-characterization stage, each of the defected cells have been identified and divided into the different types of defects (this part is also important for the previously mentioned choice of the 6th shot of each HAR run). Once the HAR cycle is over and all the EL pictures after each shot are collected, a complete frame of the generation and evolution of cracks. For better visualization, from the EL pictures are extrapolated detailed pictures of each cell where new cracks are generated or pre-existent cracks from MEL enlarged during the HAR cycle; then, those pictures are used as a basis for animations showing the evolution of each damaged cell during the HAR cycle, starting from the EL picture correspondent to the shot before the crack is generated. An example of these animation will be showed in the appendix.

The following plots collects all the data regarding the various cracks' formation divided by type. The first important thing to look for is the amount of crack generated

on previously damaged cells divided per type of initial defect, in order to understand the severity of these flaws; from the graph can be deduced that, as expected, mechanical puncture or handling damages on cells are the most likely to develop into cracks when the module is impacted by iceballs, followed by chips on vertical edges (as mentioned above caused by overly high stresses during the soldering phase) and ones on horizontal edges. Between these two types of chips, ones on horizontal top edges are the most common on the modules chosen for the experiment, and a good amount of the cells having this type of defect shows multiple chips on his top edge; despite that cells damaged on the vertical edges are more likely to generated crack. During the experiment, the only one cell with a chip on the corner generated a crack, but, considering such a low amount of data, this result won't be taken into account. Lastly, damages correlated to high temperature or contact with the soldering tool such as scratches or thermal punctures never initiated cracks during the experiment.

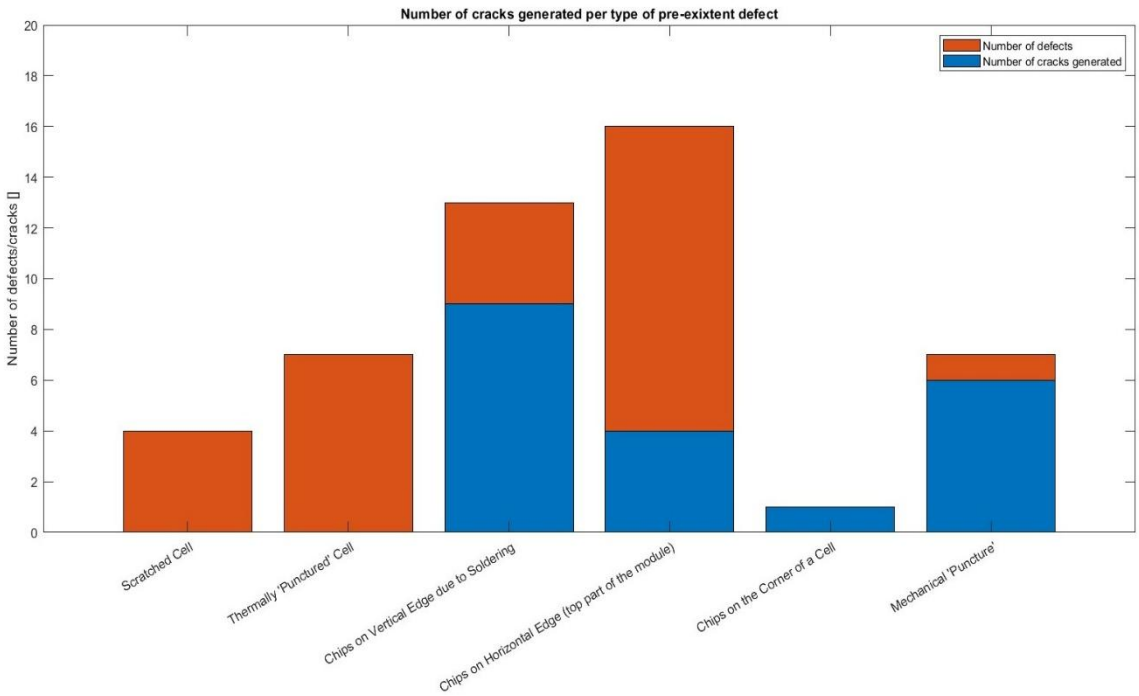

Figure 7.21: number of initiated cracks divided per type of defect

The second important thing to analyse is the distribution of the new cracks formed divided per type in function of the HAR run when they start developing. In the plot, cracks generated by iceball hitting directly on the flawed cell are highlighted. In accordance with the previous observation regarding the severity of pre-existing defect, the plot shows that mechanical puncture and chips on vertical edges usually creates cracks during the first runs, so lower impact kinetic energy, while chips on the top horizontal edges usually required higher kinetic energy or direct hits to initiate a crack; the ones documented occurred starting from 4th run, both on tilted module or perpendicular impacts of iceballs. In addition to the previously mentioned types of defects, in this plot are also shown cracks generated on cells without any visible pre-existent flaw; of the 3 documented cases, 2 of them occurred on modules impacted

perpendicularly and all of them required a direct hit on the previously considered intact cell. Considering the same type of plot fixing the different angles of incidence also allows to conclude that also the cracks formed on tilted modules required a higher kinetic energy or direct hits to develop. It can be also observed that from this experiment emerged that 50% of the new crack initiated from chips on the top horizontal edges are result of a direct impact on that cell.

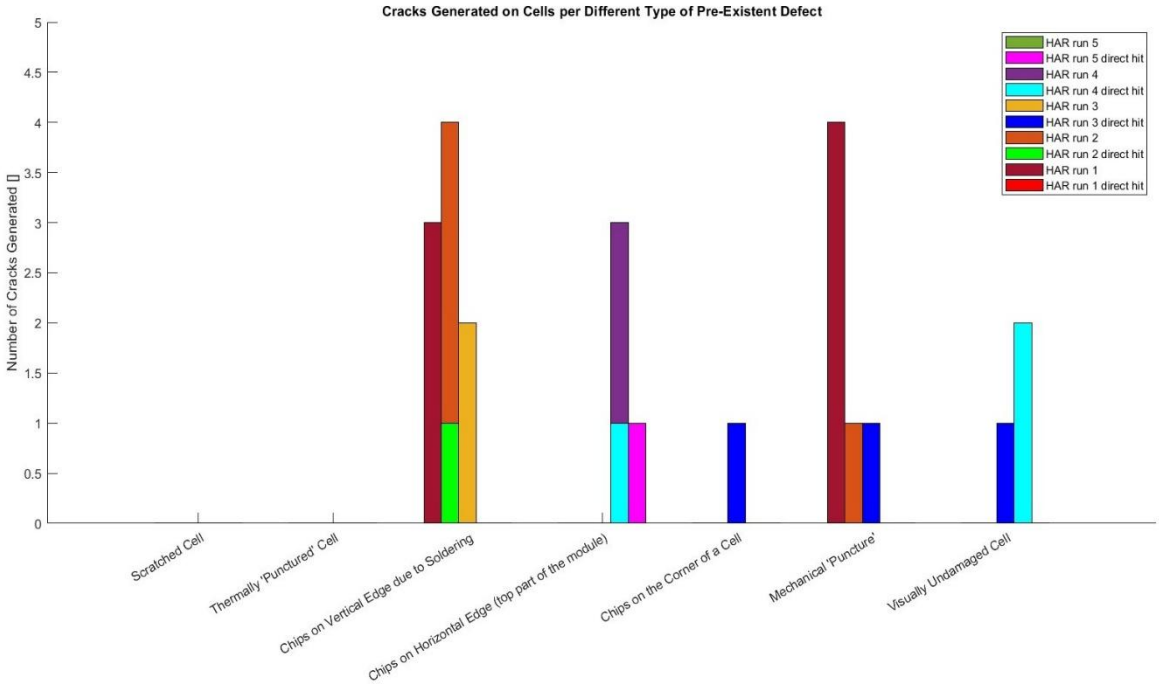

Figure 7.22: number of initiated cracks divided per type of defect and HAR run

Lastly, from the EL images is possible to deduce that once a cell is cracked, it becomes more fragile to subsequent impacts; this causes already damaged cells to rapidly fall into worse situations and possible electrical disconnections of partial area of those cells, even without breaking the glass, leading to a loss of performance of the modules.

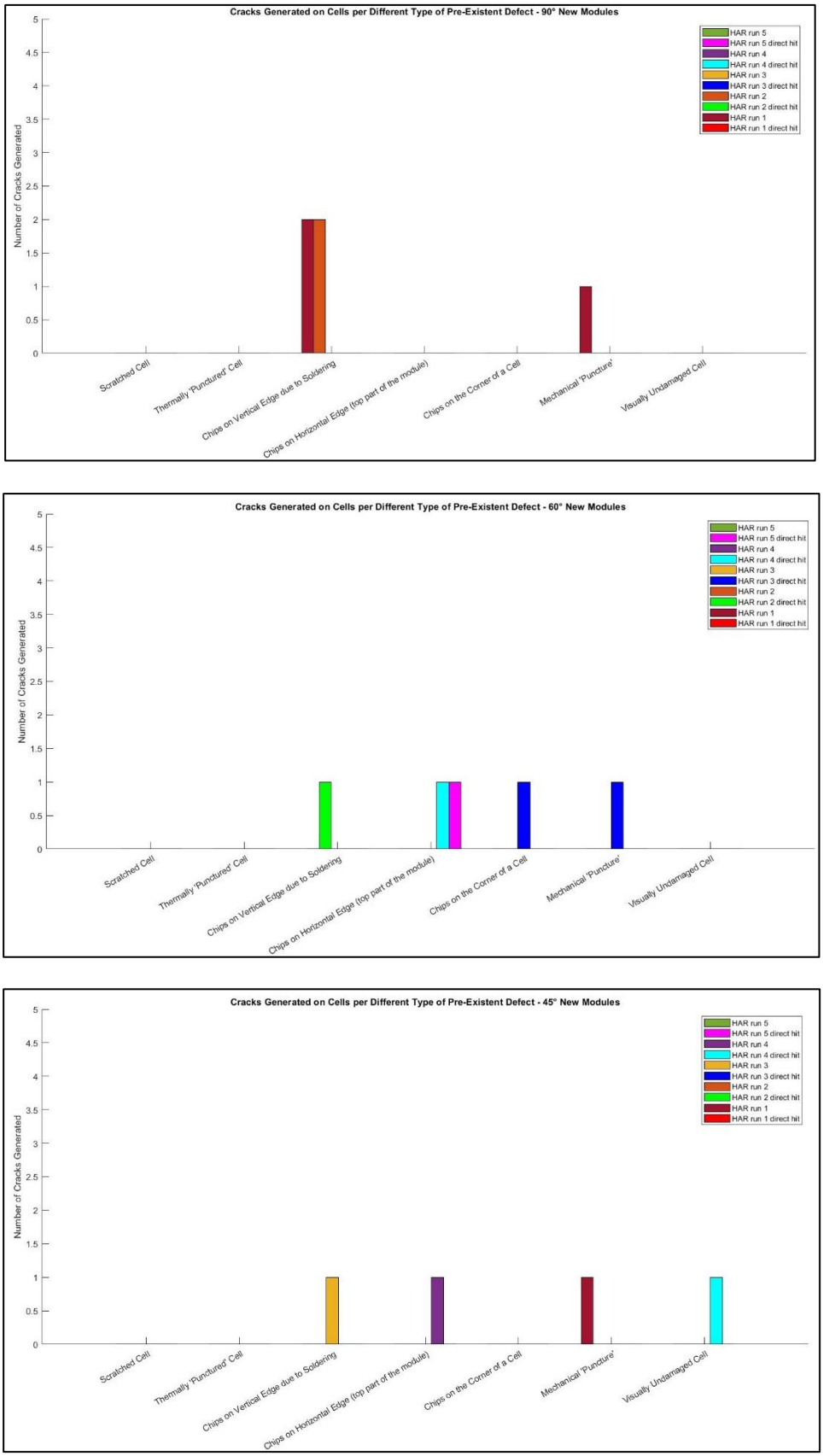

Figure 7.23: number of initiated cracks divided per type of defect and HAR run. Comparison of new modules between different angles of incidence. Top 90°, center 60°, Bottom 45°

8 Conclusions and future developments

The experiment highlights how much the different conditions of incidence angle and aging conditions impacts on the behaviour a module have when impacted by iceballs. The first important conclusion is the one regarding the mechanical impact on the front glass and the cells; from the collected data can be deduced how much changing the tilt angle and so the incidence angle allows the module, both glass and solar cells, to withstand bigger impact kinetic energies from the iceballs, as expected. The data collected show how also the formation of cracks from the pre-existent defects on the cells is shifted towards higher impact kinetic energies on tilted modules. Another important founding is how a high amount of iceball impacts helps the cracks to enlarge and so decreasing the active area and creating electrical disconnections of part of the cells, causing a decrease in the performance of the module. The electrical parameters, especially I_{sc} and P_{max}, decreased following the severity of the damages created on the cells, which are mostly dependent on the amount of iceballs' impact withstood; the higher Delta_P_{max} is observed in modules where the new cracks generated also dark zones, easily detectable on EL pictures. V_{oc} variability during the HAR cycle is on the same order of magnitude of the uncertainty of measurement, even if it slowly decreases, so can be considered almost constant. Most of the new cracks are generated on cells with pre-existent defects. From the crack analysis emerges how the different types of cell defects have different probability of generating cracks; mechanical punctures on the cells and chips on the side edges are the most likely to initiate new cracks, while lightly scratched cells or chips on the top edges (close to the top frame) rarely generated cracks, or they did when hit directly with an iceball. It also important to notice how the most severe defects initiate cracks when the module is impacted with lower kinetic energy, and usually during the first few shots. Few visually perfect cells cracked during the experiment, usually when hit directly by iceball having kinetic energy close to the one documented for the glass breakage of the module having the same incidence angle.

In future experiments, it could be interesting to increase the number of modules tested, both having similar or very different characteristics, especially on tilted modules in order to have a more precise interpolation of the data on the kinetic energy needed to break the glass and understanding the variability of those data. It could be also meaningful to try making multiple shots with a kinetic energy similar but lower than the one documented for the glass breakage to try to find a threshold where the impacts crack a visually perfect cell without breaking the glass.

Bibliography

[1] H. C. Kim and V. Fthenakis, *Photovoltaics: Life-cycle analyses..*

[2] F. W. Zwiers, X. Zhang and Y. Feng., *Anthropogenic influence on long return period daily temperature extremes at regional scales.*

[3] R. Lombardia, *Danni maltempo, da lombardia richieste per 207 milioni, 2019..*

[4] F. E. M. Program., *Hail damage mitigation for solar photovoltaic systems, 2022..*

[5] IEA, *Solar pv, 2023..*

[6] Swissolar, *Statistica sull'energia solare 2023: Ancora una volta oltre il 50% di crescita del mercato.*

[7] IEA, *Photovoltaic Power Systems Programme (IEA PVPS). Trends in Photovoltaic Applications 2023.*

[8] T. D. OpenCourseWare, *Solar Cells R4: Chapter 4 - Solar Cell Operational.*

[9] L. Lighting, *What is the polarity of LED lights?.*

[10] *Ibc solar cells.*

[11] *Iec 61215: Terrestrial photovoltaic (pv) modules – design qualification and type approval.*

[12] F. Sfolcini, *Ageing and Reliability Assessment of Photovoltaic Systems. Master's thesis, Politecnico di Milano, Energy Engineering - Ingegneria Energetica.*

[13] EcoProgetti, *The Structure of Photovoltaic Module..*

[14] ITRPV, *International Technology Roadmap for Photovoltaic..*

[15] IEA, *Iea technology guide, 2023..*

[16] Fraunhofer, *Fraunhofer photovoltaics report..*

[17] NREL, *Champion Photovoltaic Module Efficiency Chart, 2023..*

[18] Sunpower, *What is perc solar cell technology?.*

[19] A. Calcabrini, V. Kambhampati, P. Manganiello, Z. Miro and I. Olindo, *The relevance of the cell's breakdown voltage in the dc yield of partially shaded pv modules..*

[20] R. Technologies., *TOPCon Solar Cells – Product Overview..*

[21] Solarwatt, *Topcon solar cells..*

[22] *What are heterojunction (hjt) solar panels?, 2019..*

[23] *Half-cut solar panels, 2023..*

[24] *Bifacial solar panels..*

[25] *Benchmarking utility-scale pv..*

[26] NREL, *Photovoltaic degradation rates: An analytical review..*

[27] C. Del Pero, N. Aste, F. Leonforte and F. Sfolcini, *Long-term reliability of photovoltaic c-si modules – a detailed assessment based on the first italian bipv project..*

[28] GExperience, *Amazon Has Closed Solar Rooftops Last Year After Fires and Explosions..*

[29] IEA, *Review of failures of photovoltaics modules, 2014..*

[30] *Solar pv and extreme weather..*

[31] M. Paggi, M. Corrado , A. Infuso and I. Berardone, *Fatigue degradation and electric recovery in silicon solar cells embedded in photovoltaic modules*, 2014.

[32] PVQUAT, *Wind load..*

[33] IEC, *IEC 62938:2020 - Photovoltaic (PV) modules - Non-uniform snow load testing, 2020..*

[34] PVeurope, *Testing modules for resistance to inhomogeneous snow load..*

[35] VKF, *Vkf hail resistance test: Guidelines for evaluating building materials and photophotovoltaic,* 2022.

[36] J. Kopp, K. Schröer, C. Schwierz, A. Hering, U. Germann and O. Martius, *The summer 2021 switzerland hailstorms: weather situation, major impacts and unique observational data.*

[37] K. Heltsley, *Impact of hail on solar panels all you need to know..*

[38] T. Pucik, *Hailstorms of 2023,* 2024.

[39] T. H. Raupach, O. Martius, J. T. Allen, M. Kunz, S. Lasher-Trapp, S. Mohr, K. L. Rasmussen, R. J. Trapp and Q. Zhang, *The effects of climate change on hailstorms.*

[40] M. Kozjek, D. Vengust, T. Radošević, G. Žitko, S. Koren, N. Toplak, I. Jerman, M. Butala, M. Podlogar and M. K. Viršek, *Dissecting giant hailstones: A glimpse into the troposphere with its diverse bacterial communities and fibrous microplastics.*

[41] M. Montagnat, M. Bourcier, C. C. Bauer, P. D. Bons, A. Philip, P. Deconinck and P. Hereil, *Texture characterization of some large hailstones with an automated technique,* 2021.

[42] R. Wright, I. M. Giammanco and A. J. Heymsfield, *Terminal velocities and kinetic energies of natural hailstones.*

[43] J. Sun, N. Lam, L. Zhang and D. Ruan, *Contact forces generated by hailstone impact..*

[44] S. Shi, N. Lam, S. Chen and Y. Cui, *An analytical approach for modelling contact forcing function of hailstone impact.*

[45] M. B. Phelps and I. Giammanco, *Evaluating the compressive stress of hail and its relationship to freezer ice balls.*

[46] RETC, *2024 PV Module Index Report.*

[47] C. E. Reviews, *Solar Panel Components and Construction..*

[48] M. Solutions, *PV Module Judgement Criteria (Rev 5.0),* 2021.

[49] E. Cadoni, D. Forni, M. Dotta, M. Caccivio and G. Bellenda, *Advanced characterisation of photovoltaics for hail resistance.*

A Appendix

Example of EL animation for the “crack analysis”: frame by frame on “Demo Module”

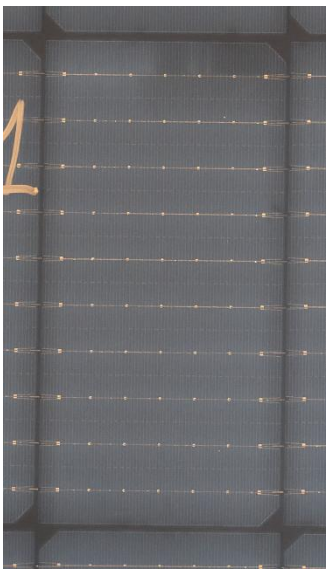	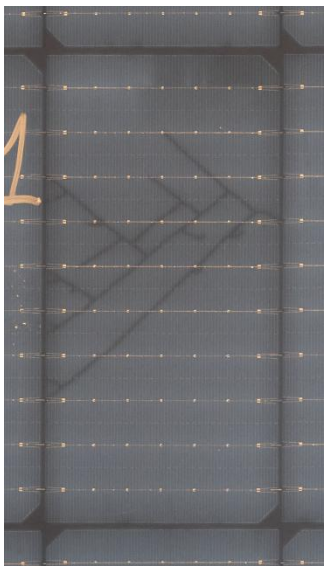	
Pre-characterization	After shot 1	After shot 2
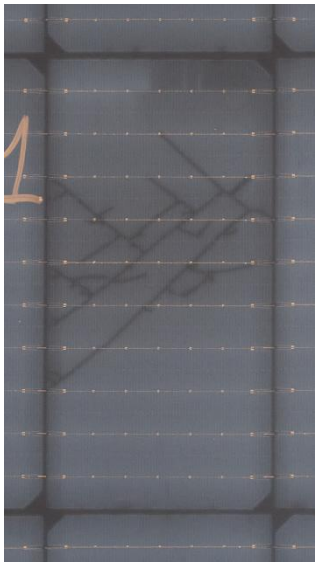	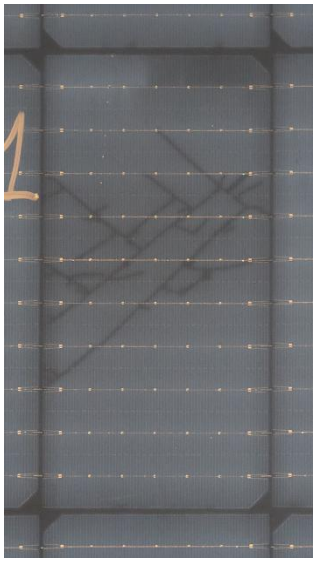	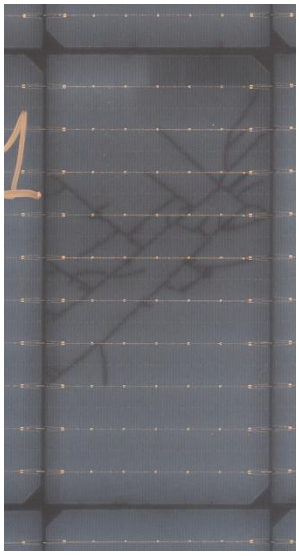
After shot 3	After shot 4	After shot 5

	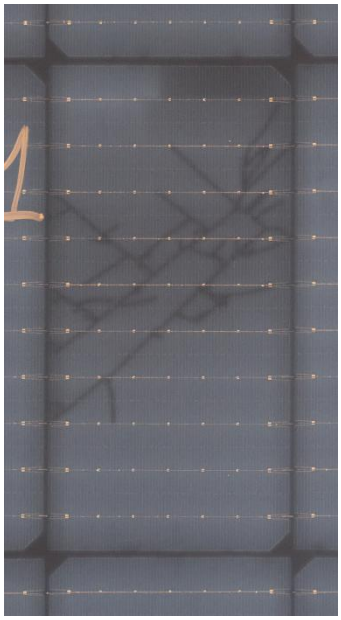	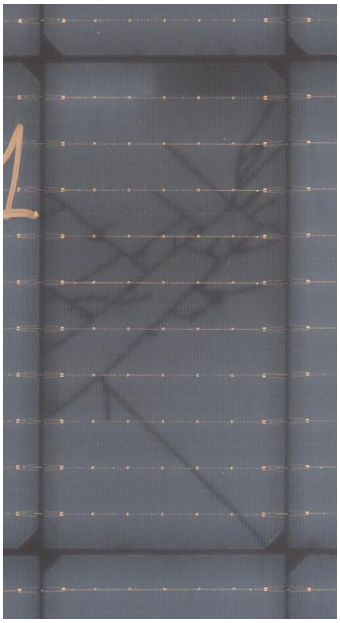
After shot 6	After shot 7	After shot 8
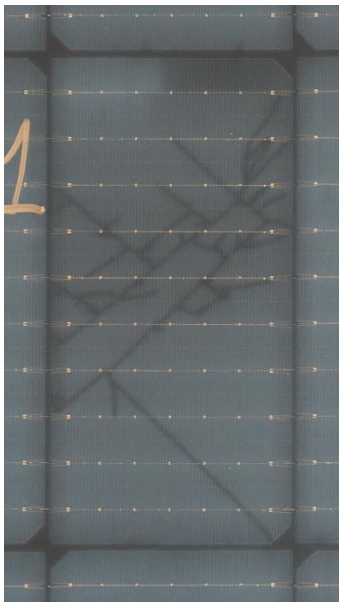	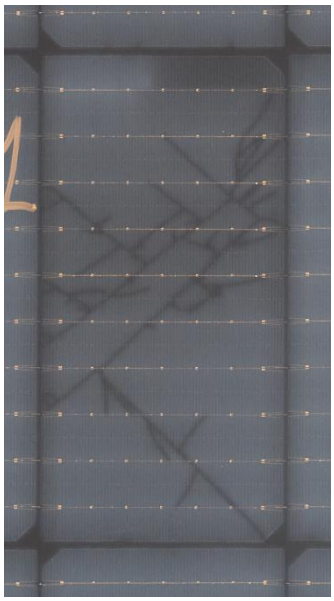	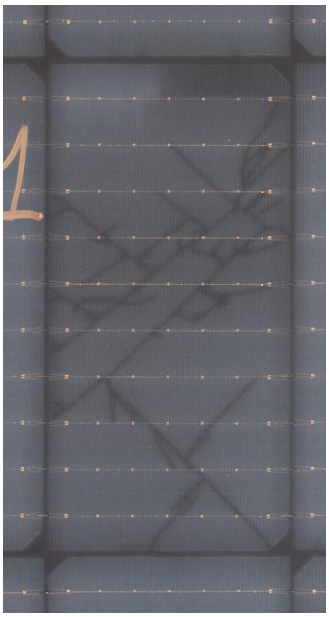
After shot 9	After shot 10	After shot 11

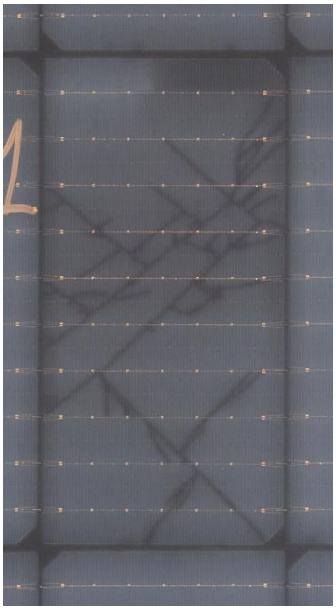		
After shot 12	After shot 13	After shot 14
After shot 15	After shot 16 (broken glass)	

Arres 3.0 Premium L 420

Die Lösung für gehobene Ansprüche

ARRES INDACH SOLARSYSTEM

Die Arres Premium L Module für Indachlösungen überzeugen durch höchste Qualitätsansprüche zum top Preis-Leistungsverhältnis.

Das deutsche Soluxtec Hochleistungs-Solarmodul NTYPE TOPCON mit Half-cut Technologie ist mit 4 mm starkem, gehärtetem Sicherheitssolarglas ausgestattet.

Schweizer Qualität
Sowohl die Entwicklung und stetige Weiterentwicklung des Systems, als auch der Montage- und Qualitätsmanagementprozesse erfolgt in der Schweiz.
25 Jahre lineare Leistungsgarantie, 10 Jahre Produktgarantie.

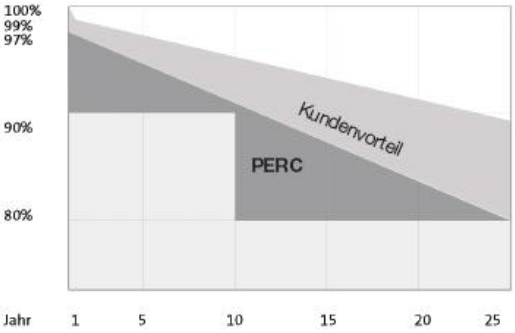

Leistungsgarantie über 25 Jahre

Hauptmerkmale auf einen Blick
Optisch ansprechende Gestaltung mit schwarzem Rahmen und schwarzer Rückseitenfolie sowie verdeckten Leiterbahnen
Optimierte Glasoberfläche mit sehr niedrigen Reflexionswerten
Ausgezeichnete Leistung bei Schwachlichtverhältnissen
Optimiertes Leistungsverhalten bei hohen Temperaturen
Überragende Hagelwiderstandsklasse: HW 5
100 % Elektrolumineszenzprüfung (EL) bei jedem Modul
100 % Europäische Produktion

Vorteile auf einen Blick
Bestes Preis-/Leistungsverhältnis für ein DE/CH Produkt
Schnelle Montage und einfache Demontage
Sehr hohe Stabilität
Ansprechende ästhetische Lösung
Gute Hinterlüftung möglich dank geringer Höhe des Rahmenprofils
Hohe Servicefreundlichkeit

ISO 9001:2015 ISO 14001:2015 PV CYCLE PID SAFE

stiftung elektro-altgeräte-register® ear
WEEE-REG.Nr. 70010859

Herstellung
ISO 9001: 2015: Qualitätsmanagementsysteme
ISO 14001: 2015: Umweltmanagementsysteme

Info
Rastermasse und Massskizzen auf Anfrage oder unter arres.ch

Leistungsdaten bei Standardtestbedingungen (STC)
(STC: 1000 W/m², Modultemperatur 25 °C +/-2°C, AM 1,5 – acc. IEC 60904_3)

Arres 3.0 Premium Modul L 420

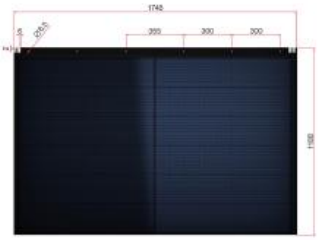

Elektrotechnische Kennwerte		
Nennleistung	Pmax [Wp]	420
Kurzschlussstrom	Isc [A]	13.73
Leerlaufspannung	Voc [V]	38.52
Strom	Impp [A]	13.04
Spannung	Vmpp [V]	32.24
Moduleffizienz	[%]	21.43
Max. Systemspannung	[V]	1500
Klassenbreite	[Wp]	– 0/+4.99
Rückstrombelastbarkeit	I_R [A]	25A
Pmax Temperaturkoeffizienten	[%/°K]	– 0.30
Voc Temperaturkoeffizienten	[%/°K]	– 0.28
Isc Temperaturkoeffizienten	[%/°K]	+ 0,03
Nennbetriebstemparatur der Zelle	(NOCT) [°C]	45 +/– 2

Technische Details	
Zellenzahl	108 Half-cut
Zellentypen	NTYPE TOPCON M10
Glas	4 mm thermisch gehärtetes und profilitertes Glas
Rückwand	Langzeit-UV-beständige Isolierfolie (TÜV geprüft)
Rahmen	Aluminium, schwarz eloxiert
Anzahl der Dioden	3
Anschlussdose	IP 68
Stecker	Sträubli Evo2
Anschlusskabellänge	2 x 1200 mm
Gewicht	26.5 kg
Modulmasse (Packmass)	29 Module, 1854x1284x1272 mm (LxBxH)
Betriebstemperaturbereich	– 40 bis + 85 °C

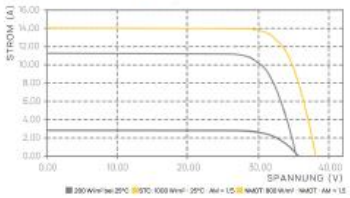

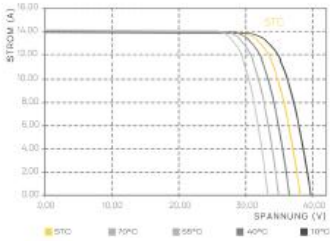

Zulassungen, Zertifikate, Normen	
max. Druck	5.40 kN/m2 IEC/EN61215 2nd Ed.
max. Sog	2.40 kN/m2, IEC/EN61215 2nd Ed.
Hagelbeständigkeit	Geprüft bis 50mm Durchmesser bei 30.8 m/s Hagelschutzklasse 5, Schweizerisches Hagelschutzregister
Betriebssicherheit	Class A, Schutzklasse II, IEC/EN61730
Modul-Garantie	10 Jahre Produktgarantie, 25 Jahre lineare Leistungsgarantie
Montage nach	SN EN 50583 - Montagekategorie A

Die Spezifikationen unterliegen technischen Änderungen und Prüfungen ohne vorherige Veröffentlichung.
Die Solarmarkt GmbH behält sich das Recht der endgültigen Auslegung vor.

Solarmarkt GmbH, Neumattstrasse 30, 5000 Aarau, Schweiz, +41 62 200 62 00, info@arres.ch, **arres.ch**

ARRES
INDACH SOLARSYSTEM

Version 1/23

List of Figures

Figure 1.1: P-N junction 4
Figure 1.2: Effect of T on I-V curves 6
Figure 1.3: Effect of G on I-V curves 6
Figure 1.4: PV module assembly 7
Figure 1.5: Champion module efficiencies 9
Figure 1.6: IBC cell comparison 11
Figure 1.7: IBC cell structure 11
Figure 1.8: TOPCon PERC comparison 12
Figure 1.9: Example of Half-Cut module 13
Figure 1.10: Half-Cut connection 13
Figure 1.11: Traditional Connection 13
Figure 1.12: Monofacial Bifacial comparison 14
Figure 2.1: Fire caused by hotspot induced failure 16
Figure 3.1: IR Imaging with a drone 20
Figure 3.2: UV fluorescence image 21
Figure 3.3: EL image 22
Figure 3.4: Snow Load test 23
Figure 4.1: Map of reports divided for hailstone diameter 28
Figure 4.2: Number of reports and days with large (2+ cm), ... 28
Figure 4.3: Hail formation and expected future conditions 30
Figure 4.4: Annual hail probability [d/y] 32
Figure 4.5: Hailstorm damages in Italy 33
Figure 4.6: Giant hailstone observed in Italy 33
Figure 4.7: Natural and synthetic particles influence in hail formation 34
Figure 4.8: Stratification and c-axis orientation in different hailstones 36
Figure 4.9: Data from hail characterization study 39

Figure 4.10: Terminal velocity per D_{max} and D_{eq} 40
Figure 4.11: Kinetic energy per D_{max} and D_{eq} 41
Figure 4.12: Analytical model and impact phases 43
Figure 4.13: Loading Phase 44
Figure 4.14: Unloading phase 44
Figure 4.15: Numerical vs experimental results 45
Figure 4.16: Influence of velocity and diameter 46
Figure 4.17: Influence of temperature 46
Figure 5.1: PASAN III B solar simulator 50
Figure 5.2: PASAN III B spectral match 50
Figure 5.3: I-V curve estimation 50
Figure 5.4: EL test station in the darkroom 51
Figure 5.5: High-resolution camera 52
Figure 5.6: Objectives 52
Figure 5.7: Mechanical load test 53
Figure 5.8: Tubes for air cannon 53
Figure 5.9: Hail resistance test 53
Figure 6.1: Example of target locations 60
Figure 6.2: KE in function of diameter and equivalent diameter per HAR run 61
Figure 6.3: P_{max} new modules 62
Figure 7.1: Measured maximum kinetic energy withstood by modules 63
Figure 7.2: Comparison between module with different incidence angle 64
Figure 7.3: Delta_P_{max} per module 65
Figure 7.4: Evolution of Delta_P_{max} during HAR cycle 66
Figure 7.5: Delta_P_{max} per module. Comparison for different angle of incidence 67
Figure 7.6: Evolution of Delta_P_{max} during HAR cycle. Comparison for different angle of incidence 67
Figure 7.7: Comparison between EL pre-characterization and last measurement before glass breakage. From the top: *90° New Module", 60° New Module", 45° New Module"* 68
Figure 7.8: Delta_P_{max} per module. Comparison for different aging condition 69

Figure 7.9: Evolution of Delta_P_{max} during HAR cycle. Comparison for different aging condition 70

Figure 7.10: Comparison between EL pre-characterization and last measurement before glass breakage. From the top: *90° New Module*", "*DAH Module 1* 70

Figure 7.11: Comparison between EL pre-characterization and last measurement before glass breakage. From the top: "*DAH Module 2*", "*MEL Module 1*", "*MEL Module 2*" 71

Figure 7.12: Evolution of Delta_V_{oc} during HAR cycle 72

Figure 7.13: Evolution of Delta_I_{sc} during HAR cycle 72

Figure 7.14: Delta_P_{max} per module after glass breakage 73

Figure 7.15: VI and EL of a module with broken front glass 73

Figure 7.16: Crack-forming, glass breaking shots and kinetic energy. Complete 74

Figure 7.17: Crack-forming, glass breaking shots and kinetic energy. Comparison between different angles of incidence 75

Figure 7.18: Crack-forming and glass breaking shots and kinetic energy. Comparison between different pre-aging conditions 75

Figure 7.19: Crack-forming, glass breaking shots and angle of incidence. 76

Figure 7.20: examples of types of defects on cells. Top row, from left to right: Dark zone, scratches, thermal puncture, chip on vertical edge. Bottom row, from left to right: chip on the corner, chips on horizontal edge, puncture, cracked cell due to MEL 78

Figure 7.21: number of initiated cracks divided per type of defect 79

Figure 7.22: number of initiated cracks divided per type of defect and HAR run 80

Figure 7.23: number of initiated cracks divided per type of defect and HAR run. Comparison of new modules between different angles of incidence. Top 90°, center 60°, Bottom 45° 81

List of Tables

Table 3.1: Comparison between IEC 61215 and VKF 25

Table 5.1: Classification criteria for PASAN III B 50

Table 5.2: Impact location according to VKF 54

Table 5.3: Requirements and tolerances for some iceball diameters according to IEC 61215 55

Table 5.4: Requirements and tolerances for some diameters according to VKF 55

Table 6.1: Summary of the modules and design of experiment 59

Table 6.2: Target location's choice criteria 60

Table 6.3: Impact velocity, kinetic energy and equivalent diameter per HAR run 60

Table 6.4: P_{max} and FF per module 62
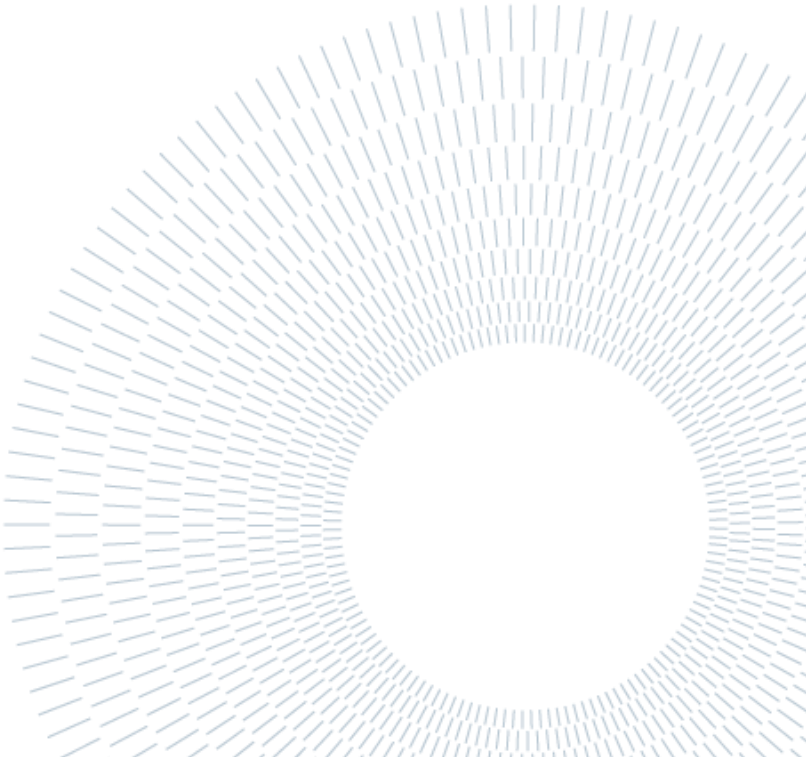
Table 7.1: Glass breakage kinetic energy and HAR run per module (measured) 64